COMPUTATIONAL THERMAL SCIENCES

AN INTERNATIONAL JOURNAL

COMPUTATIONAL THERMAL SCIENCES

AIMS AND SCOPE. Computational Thermal Sciences is a new international journal designed to provide a forum for the exposure and exchange of ideas, methods and results in computational thermodynamics, fluid dynamics, heat transfer and mass transfer in solids, liquids and gases, with applications in areas such as energy, materials processing, manufacturing and the environment. All modes of heat and mass transfer will be included: conduction, convection, diffusion, radiation and phase change. Topics to be covered will also include the laws of thermodynamics, the thermal properties of substances, engine and refrigeration cycles and combustion.

Papers on all aspects – both fundamental and applied – will be welcome: on the one hand the development of new mathematical methods and computational algorithms, and on the other the application of new or existing methods to the solution of problems in the thermal sciences. Reports of experimental studies undertaken in conjunction with computational work are encouraged. The assessment of the accuracy of computational solutions through verification (examining and limiting errors associated with discretization and with the computational solution methods adopted) and validation (quantification of errors in the physical models used) are essential parts of any computational study, and authors will be expected to examine these aspects.

Computational Thermal Sciences

TATIANA GAMBARYAN-ROISMAN
Faculty of Mechanical and Process Engineering
Technische Universität Darmstadt
Petersenstr. 30
64287 Darmstadt, Germany
gtatiana@ttd.tu-darmstadt.de

MOHAMED HAMED
Department of Mechanical Engineering
McMaster University
1280 Main Street West
Hamilton, ON, Canada L8S 4L7
hamedm@mcmaster.ca

KEMO HANJALIC
Faculty of Applied Sciences
Delft University of Technology
Lorentzweg 1
2628 CJ Delft, The Netherlands
hanjalic@ws.tn.tudelft.nl

MASARU ISHIZUKA
Toyama Prefectural University
5180 Kurokawa Imizu-shi
Toyama, Japan 939-0398
ishizuka@pu-toyama.ac.jp

JOON SIK LEE
Seoul National University
San 56-1. Sillim-dong
Gwanak-gu .Seoul 151-742 Korea
jslee123@snu.ac.kr

GORDON MALLINSON
Department of Mechanical Engineering
University of Auckland
Bldg. 401, Room 1.909, Private Bag 92019
Auckland 1142, New Zealand
g.mallinson@auckland.ac.nz

PATRICK H. OOSTHUIZEN
Department of Mechanical and Materials Engineering,
Room 301, McLaughlin Hall
Queen's University
Kingston, ON K7L 3N6, Canada
oosthuiz@me.queensu.ca

D. A. S. REES
Dept. of Mechanical Engineering
University of Bath
Claverton Down, Bath, BA2 7AY UK
D.A.S.Rees@bath.ac.uk

NEVIN SELCUK
Department of Chemical Engineering
Middle East Technical University
06531 Ankara Turkey
selcuk@metu.edu.tr

EVGUENI M. SMIRNOV
Department of Aerodynamics
St. Petersburg State Polytechnic University
29, Polytechnitcheskaya Str.
St. Petersburg, 195251, Russia
aero@phmf.spbstu.ru

PETER VADASZ
Department of Mechanical Engineering
Northern Arizona University
PO Box 15600
Flagstaff, AZ 86011-5600, USA
peter.vadasz@nau.edu

RICHARD K. K. YUEN
Department of Building and Construction
City University of Hong Kong
Tat Chee Avenue, Room B6506
Kowloon, Hong Kong
Richard.Yuen@cityu.edu.hk

COMPUTATIONAL THERMAL SCIENCES
AN INTERNATIONAL JOURNAL

CONTENTS

This journal contains information obtained from highly regarded sources. Reprinted material is quoted with permission, and sources are indicated. A wide variety of references are listed. Reasonable efforts have been made to publish reliable data and information, but the editor and the publisher assume no responsibility for any statements of fact or opinion expressed in the published papers or in the advertisements.

COMBINED HEAT AND MASS TRANSFER WITH PHASE CHANGE IN A VERTICAL CHANNEL

Mohamed Aboudou Kassim,[1] Brahim Benhamou,[1,] & Souad Harmand[2]*

[1]*Fluid Mechanics and Energetic Laboratory, CNRST Associate Unit URAC27, Cadi Ayyad University, P.O. Box 2390, Marrakech 40 001, Morocco*

[2]*Laboratoire de Mécanique et d'Energétique (LME), Université de Valenciennes et du Hainaut Cambrésis, Valenciennes, France*

*Address all correspondence to Brahim Benhamou E-mail: bbenhamou@ucam.ac.ma

The objective of this study is to investigate numerically the effects of mixed convection heat and mass transfer with phase change in a vertical parallel-plate channel. One of the plates is wetted by a thin liquid water film and maintained at a constant temperature, while the other is dry and thermally insulated. The mathematical model is solved numerically by the finite volume method. Buoyancy forces' effects on heat and mass transfer and hydrodynamic field are studied. The results show that these forces have an important effect on the flow field as well as on heat and mass transfer characteristics. Indeed, they act in the opposite direction of the upward flow and induce a flow reversal near the isothermal plate. Heat and mass transfers are diminished by buoyancy forces, which slow down the flow.

KEY WORDS: *numerical study, channel flow, heat and mass transfer, mixed convection, buoyancy forces, flow reversal, condensation*

1. INTRODUCTION

Combined heat and mass transfer problems are of importance in many processes and have therefore received a considerable amount of attention. Notable examples include cooling towers, waste heat disposal in industrial processes, protection of system components from high-temperature gas streams, cooling of electronic equipment, and desalination. Many analyses of combined heat and mass transfer convection in channels are available in the literature. Turbulent heat and mass transfer in an asymmetrically heated, vertical parallel-plate channel has been studied by Fedorov et al. (1997). One of the plates is isothermally heated and wetted by a thin liquid water film, and the other is dry and thermally insulated. The film thickness is assumed extremely thin. On the basis of their numerical results, the authors showed that heat transfer is dominated by the transport of latent heat associated with evaporation of the liquid film. Also, these results suggest that heat and mass transfer analogy begin to break down after the flow transition from laminar to turbulent.

A numerical study was performed by Feddaoui et al. (2003) for modeling laminar mixed convection heat and mass transfer with evaporation of a liquid film streaming along an insulated vertical parallel-plate channel. The authors showed that the cooling of the film is mainly caused by latent heat transport associated with evaporation. The effects of thermal and solutal buoyancy forces on both upward and downward airflow in a vertical parallel-plate channel have been investigated numerically by Azizi et al. (2007). The plates are wetted by a thin liquid water film and maintained at a constant temperature lower than that of the air entering the channel. Cases with evaporation and condensation have been investigated. Results show that buoyancy forces have an important effect on heat and mass transfer. It has been established that heat transfer associated with these phase changes may be more or less important compared to the sensible one. On the other hand, the authors showed that flow reversal may occur for an upward flow with a relatively high temperature difference between the incoming air and the walls. The authors seem to be pioneers in studying flow rever-

NOMENCLATURE

b	half-channel width (m)		x, y	axial and transverse coordinates (m)

b half-channel width (m)

C mass fraction (kg vapor/kg mixture)

C_p specific heat (J kg^{-1} K^{-1})

D diffusion coefficient (m^2/s)

D_h $= 4.b$, hydraulic diameter (m)

g gravitational acceleration (m/s^2)

h_{gf} latent heat of condensation (kJ/kg)

h heat transfer coefficient (W/m^{2}K)

k thermal conductivity [W/(m.K)]

L channel length (m)

$\dot{m}''$ condensed mass flux at liquid-air interface [kg/(s m^2)]

Nu_m $= \frac{1}{x}\int_0^x \mathrm{Nu}_x dx$, mean Nusselt number

P_m $= p + \rho_{in}gx$, modified pressure (Pa)

Sh_m $= \frac{1}{x}\int_0^x \mathrm{Sh}_x dx$, mean Sherwood number

T temperature (K)

u, v axial and transverse velocity components (m/s)

Ve transverse velocity of the vapor at air-liquid interface (m/s)

x, y axial and transverse coordinates (m)

Greek Symbols

β_M $= (M_a/M_v) - 1$, coefficient of mass expansion

β_T $= 1/T_{in}$, coefficient of thermal expansion (K^{-1})

μ dynamic viscosity (Pa s)

ν kinematic viscosity ($= \mu/\rho$) (m^2/s)

ρ density (kg/m^3)

φ humid air relative humidity (%)

Subscripts

a air

AD   adiabatic

in at the inlet

IS   isothermal

L relative to the latent heat

m mean value

S relative to the sensible heat

v vapor

w at the wall

sal in developing flow with heat and mass transfer since studies on this subject have dealt with fully developed flow (Salah El-Din, 1992; Boulama and Galanis, 2004). Two-phase modeling of laminar film condensation from mixtures of a vapor and a noncondensing gas in parallel-plate channels has been studied by Siow et al. (2007). The channel is inclined downward from the horizontal and has an isothermal cooled bottom plate and an insulated upper plate. Results for steam-air mixtures are presented and the effects of changes in the angle of inclination, inlet gas mass fraction, airflow Reynolds number, and inlet temperature are examined. It was found that an increase in the angle of declinations results in thinner and faster-moving liquid films. The authors show that increasing airflow Reynolds number always produces thinner films and higher Nusselt numbers. A numerical study of turbulent heat and mass transfer on mixed convection with film evaporation has been conducted by Jang and Yan (2006). These authors consider a turbulent hot downward airflow in a parallel-plate channel. Both plates are thermally insulated and wetted by a liquid water film. The inlet temperature of this film was set at 20°C. In this study, the effects of liquid flow rate, airflow Reynolds number, and inlet air

temperature are studied. Their results show that a higher value of the two latter parameters causes larger sensible and latent heat transfer and better mass transfer, while the effect of liquid flow rate on heat and mass transfer is insignificant.

A numerical and experimental analysis has been carried out by Tsay et al. (1990) to explore the detailed heat transfer characteristics for a falling liquid film along a vertical insulated flat plate. Free stream air temperature was set at 30°C and inlet liquid film temperature was taken to be equal to 30°C or 35°C. Variable thermophysical properties are considered. The results show that latent heat transfer connected with vaporization mainly causes cooling of the liquid film. The authors affirm that when inlet liquid temperature is equal to ambient temperature, latent heat transfer due to the film vaporization initiates heat transfer in the film and gas flow. Convective instability of heat and mass transfer for laminar forced convection in the thermal entrance region of a horizontal rectangular channel has been examined by Lin et al. (1992). The rectangular channel is thermally insulated, except for the bottom wall. The latter is maintained at a constant temperature and covered by a thin liquid water film. The thick-

ness of this film is neglected, and thus it is treated as a boundary condition for heat and mass transfer. Inlet air temperature was fixed at 20°C. The effects of changes of bottom wall temperature, relative humidity of air at the entrance, and the channel aspect ratio are examined. The results show that the convective instability is affected by changes in inlet air relative humidity and temperature and also the channel aspect ratio.

Volchkov et al. (2004) reported a numerical work on both laminar and turbulent forced convection of humid air over an infinite flat plate. A boundary-layer-type model was used and the authors aim to establish the validity of the heat-mass transfer analogy. The steam in the humid airflow may condensate on the plate whose temperature is lower than that of the airflow. The authors made a major simplification by neglecting the effect of the condensate film. They claim that this assumption is justified by the experimental data in the literature which indicate that measurements of the liquid film-air interface temperature in humid-air flows show that it is close to the saturation temperature corresponding to the vapor concentration at the plate.

It should be mentioned that the assumption of negligible liquid film thickness has been extensively used in heat and mass transfer problems (Lin et al., 1992; Fedorov et al., 1997; Ait Hammou et al., 2004; Volchkov et al., 2004; Azizi et al., 2007). The film was then treated as a boundary condition. The validity of this assumption has been investigated by Yan (1992, 1993). The author conducted a study of laminar mixed convection with evaporation of a liquid film dripping on the inner walls of a vertical channel. The walls are isothermally heated (Yan, 1993) or heated by a uniform heat flux (Yan, 1992). In each case, the author conducted two studies: one with the conservation equations solved both in liquid and gas phases and the other with thickness neglected. By comparing the results of these two studies, the author was able to demonstrate that the assumption of negligible film thickness is valid for low liquid film flow rates.

The objective of this study is to investigate the effect of inlet humidity of laminar airflow in an asymmetrically cooled parallel-plate channel. The adopted model includes an axial diffusion terms and thus allows for computing flow reversal situations.

2. MATHEMATICAL MODEL AND NUMERICAL METHOD

We consider a vertical parallel-plate channel. One of the plates is wetted by a thin liquid water film and main-

tained at a constant temperature T_w, while the other is dry and thermally insulated. A hot upward airflow enters the channel with uniform velocity u_{in}, temperature T_{in}, and relative humidity φ_{in} (Fig. 1). We consider that the liquid film, streaming along the isothermal plate, is extremely thin so that it can be treated as a boundary condition. As reported in the introduction, this assumption has been found to be relevant for low liquid film flow rates (Yan, 1992, 1993). The present study deals with such low liquid flow rates. Steady state conditions are considered, and the flow is supposed to be laminar. Viscous dissipation, radiation heat transfer, and Duffour and Soret effects are negligible (Gebhart and Pera, 1971). Thermodynamic equilibrium is assumed at the liquid film-air interface. The physical properties are taken to be constant, except for the density in the body forces, which is considered to be a linear function of temperature and mass fraction (Oberbeck-Boussinesq approximation):

$$\rho = \rho_{in} \left[1 - \beta_T \left(T - T_{in} \right) - \beta_M \left(C - C_{in} \right) \right] \quad (1)$$

With this formulation and the preceding assumptions, the governing equations of the problem can be written in the following form:

Continuity:

$$\frac{\partial u}{\partial x} + \frac{\partial v}{\partial y} = 0 \quad (2)$$

x-Momentum:

$$\rho \left(u \frac{\partial u}{\partial x} + v \frac{\partial u}{\partial y} \right) = -\frac{\partial P_m}{\partial x} + \mu \left(\frac{\partial^2 u}{\partial x^2} + \frac{\partial^2 u}{\partial y^2} \right)$$
$$+ \rho_{in} g \left(\beta_T \left(T - T_{in} \right) + \beta_M \left(C - C_{in} \right) \right) \quad (3)$$
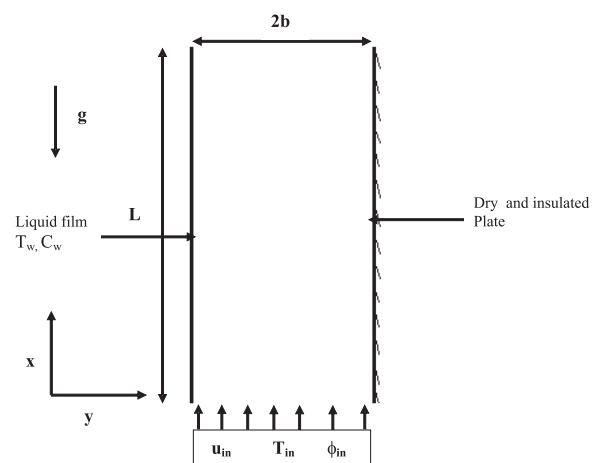
FIG. 1: Sketch of the physical system

y-Momentum:

$$\rho \left(u\frac{\partial v}{\partial x} + v\frac{\partial v}{\partial y} \right) = -\frac{\partial P_m}{\partial y} + \mu \left(\frac{\partial^2 v}{\partial x^2} + \frac{\partial^2 v}{\partial y^2} \right) \quad (4)$$

P_m is a modified pressure, which results from the linear development of the density [Eq. (1)]. It is given by $P_m = p + \rho_{in}gx$:

Energy Equation:

$$\rho C_P \left(u\frac{\partial T}{\partial x} + v\frac{\partial T}{\partial y} \right) = k \left(\frac{\partial^2 T}{\partial x^2} + \frac{\partial^2 T}{\partial y^2} \right) \quad (5)$$

Species Equation (Water Vapor):

$$u\frac{\partial C}{\partial x} + v\frac{\partial C}{\partial y} = D \left(\frac{\partial^2 C}{\partial x^2} + \frac{\partial^2 C}{\partial y^2} \right) \quad (6)$$

2.1 Boundary Conditions

At the channel inlet ($x = 0$), the humid airflow velocity is assumed uniform, and in the x-direction with constant temperature and mass fraction,

$$u = u_{in}, \quad v = 0, \quad T = T_{in}, \quad C = C_{in} \quad (7)$$

At the isothermal plate ($y = 0$), the airflow axial velocity is obviously null (no slip), and its transverse velocity is equal to that of the evaporated liquid film or condensed humid air vapor on the plate. The mass fraction is that of saturation conditions at the plate's temperature. Thus

$$u = 0, \quad v = Ve, \quad T = T_w, \quad C = C_w \quad (8)$$

where Ve is the transverse velocity component of the vapor at the liquid-gas interface. Assuming that the air-water interface is semipermeable, Ve is given by the following expression (Burmeister, 1993):

$$Ve = -\frac{D}{1 - C_W} \left. \frac{\partial C}{\partial y} \right|_{y=0} \quad (9)$$

Mass fraction at the wetted plate C_w corresponds to saturation conditions at T_w. It is calculated by assuming that the air-vapor mixture is an ideal gas mixture.

At the insulated plate ($y = 2b$),

$$u = v = 0 \quad \text{and} \quad \left[\frac{\partial C}{\partial y} \right]_{y=2b} = \left[\frac{\partial T}{\partial y} \right]_{y=2b} = 0 \quad (10)$$

At the channel exit ($x = L$), the flow is assumed fully developed. Hence

$$\frac{\partial u}{\partial x} = \frac{\partial v}{\partial x} = \frac{\partial T}{\partial x} = \frac{\partial C}{\partial x} = 0 \quad (11)$$

2.2 Flow, Heat, and Mass Transfer Parameters

The local Sherwood number at the isothermal plate is defined by

$$\text{Sh} = \frac{D_h}{C_m - C_W} \left. \frac{\partial C}{\partial y} \right|_{y=0} \quad (12)$$

where C_m is the mean mass fraction, defined as follows:

$$C_m = \frac{\int_0^{2b} \rho u C \, dy}{\int_0^{2b} \rho u \, dy} \quad (13)$$

The friction factor at the isothermal plate is given by

$$f_{IS} = -\frac{\mu \left. \frac{\partial u}{\partial y} \right|_{y=0}}{\frac{1}{2}\rho u_0^2} \quad (14)$$

The friction factor at the insulated plate is given by

$$f_{AD} = -\frac{\mu \left. \frac{\partial u}{\partial y} \right|_{y=2b}}{\frac{1}{2}\rho u_0^2} \quad (15)$$

Since both sensible and latent heat fluxes near the isothermal wetted plate are involved in this problem, the Nusselt number is the sum of a sensible and a latent one. The local sensible Nusselt number at the isothermal plate is given by

$$\text{Nu}_S = \frac{D_h \left. \frac{\partial T}{\partial y} \right|_{y=0}}{T_m - T_W} \quad (16)$$

The local latent Nusselt number at the isothermal plate is defined by Tsay and Yan (1990):

$$\text{Nu}_L = -\frac{D_h \rho D h_{fg}}{k(1 - C_W)(T_W - T_m)} \left. \frac{\partial C}{\partial y} \right|_{y=0} \quad (17)$$

where T_m is the mean airflow temperature calculated by the following expression:

$$T_m = \frac{\int_0^{2b} \rho u T \, dy}{\int_0^{2b} \rho u \, dy} \quad (18)$$

The two last terms in Eq. (3) correspond to buoyancy forces. The magnitude of these forces relative to the inertia force is given by the Grashof number. Since thermal and mass buoyancy forces appear in Eq. (3), two Grashof numbers are defined, as follows:

Solutal Grashof Number:

$$\text{Gr}_M = \frac{g\beta_M D_h^3 (C_W - C_{in})}{\nu^2} \quad (19)$$

Thermal Grashof Number:

$$\mathrm{Gr}_T = \frac{g\beta_T D_h^3 (T_W - T_{in})}{\nu^2} \qquad (20)$$

The airflow Reynolds number is

$$\mathrm{Re} = \frac{u_{in} D_h}{\nu} \qquad (21)$$

The liquid water film may evaporate in the airflow, and water vapor contained in that airflow may condense at the isothermally cooled plate. The rate of evaporation/ condensation is calculated by the evaporated/condensed mass flux of water vapor at the liquid-air interface:

$$\dot{m}'' = \frac{\rho D}{1 - C_W} \left. \frac{\partial C}{\partial y} \right|_{y=0} \qquad (22)$$

2.3 Numerical Method

A finite volume method is used for the discretization of the governing equations [Eqs. (2)–(6)]. A power-law scheme for the combined convection-diffusion term is used, and a block-correction method coupled with a line-by-line procedure is used to solve the resulting algebraic equations (Patankar, 1981). The velocity-pressure coupling is treated by the well-known SIMPLER algorithm (Patankar, 1980, 1981). Convergence of this iterative procedure is declared when the relative variation of any dependent variable is less than 10^{-4} and the mass residual falls below 10^{-6} at all the grid points. The grid is nonuniform in both the streamwise and transverse directions, with greater node density near the inlet and the walls, where the gradients are expected to be more significant. Furthermore, different grid sizes were considered to ensure that the solution was grid independent. Results of the grid sensibility study are presented in Table 1. This table presents the values of the local sensible Nusselt number Nu_s and friction factor at the isothermal plate f. Re_{IS} obtained for three grids 100×35, 200×70, and 400×140. It is clear from this table that changes in Nu_s and $f.\mathrm{Re}_{IS}$ with respect to the grid (as well as the other parameters

not presented here) are less than 5%. Hence we choose the 100×35 grid.

Validation of the computer code and the mathematical model has been carried out first for hydrodynamically and thermally developing forced thermal convection. The results are compared to those obtained by Mercer in the case of a parallel-plate channel with one of the plates isothermal and the other insulated (Shah and London, 1978). This comparison, presented in Fig. 2, concerns the mean Nusselt number Nu_m. Under the premise of heat and mass transfer analogy, results for mass transfer were obtained by setting $\mathrm{Sc} = \mathrm{Pr}$. The calculated mean Sherwood number is compared to the Nusselt number from Mercer (Fig. 2). Our results are very close to those of Mercer reported in Shah and London (1978). Other validations in the case of mixed convection with heat and mass transfer were performed. The details of these validations are given by Ait Hammou et al. (2004). In view of these successful validations, the computer code as well as the mathematical model are considered reliable.

3. DISCUSSION OF RESULTS

The thermophysical properties are taken to be constant and evaluated at a reference temperature T_{ref} and mass fraction w_{ref} obtained by these expressions: $T_{ref} = (2.T_w + T_{in})/3$ and $w_{ref} = (2.w_w + w_{in})/3$, where T_w, T_{in}, w_w, and w_{in} are, respectively, the channel's wall and inlet air temperatures and mass fractions. This special way of evaluating thermophysical properties, known as the one-third rule, has been found to be appropriate for the analysis of heat and mass transfer problems (Chow and Chung, 1983). The properties of air, water, and their mixture are evaluated by formulas given by Fuji et al. (1977). All results presented here have been calculated with an aspect ratio $L/2b = 130$ and a channel length $L = 2m$. Ambient air conditions (channel entrance) have been fixed at $T_{in} = 70°C$, $u_{in} = 0.169$ m/s (leading to Re = 300), and different airflow inlet relative humidity values $\phi_{in} = 10\%$, 30%, and 70%. The wetted plate is maintained at a constant temperature lower than that of airflow,

TABLE 1: Local sensible Nusselt number and friction factor for different grids[a]

Grid (X, Y)	$x/L = 0.025$		$x/L = 0.1$		$x/L = 0.5$		$x/L = 0.95$	
	Nu_s	$f\cdot\mathrm{Re}_{IS}$	Nu_s	$f\cdot\mathrm{Re}_{IS}$	Nu_s	$f\cdot\mathrm{Re}_{IS}$	Nu_s	$f\cdot\mathrm{Re}_{IS}$
100×35	2.07	–22.78	3.75	–38.23	4.14	6.86	4.66	18.36
200×70	2.09	–21.66	3.86	–37.66	4.26	7.02	4.69	19.2
400×140	2.18	–21.60	3.94	–37.01	4.28	7.36	4.71	19.4

[a]In the table, $\varphi_{in} = 70\%$, $T_{in} = 70°C$, and Re = 300.
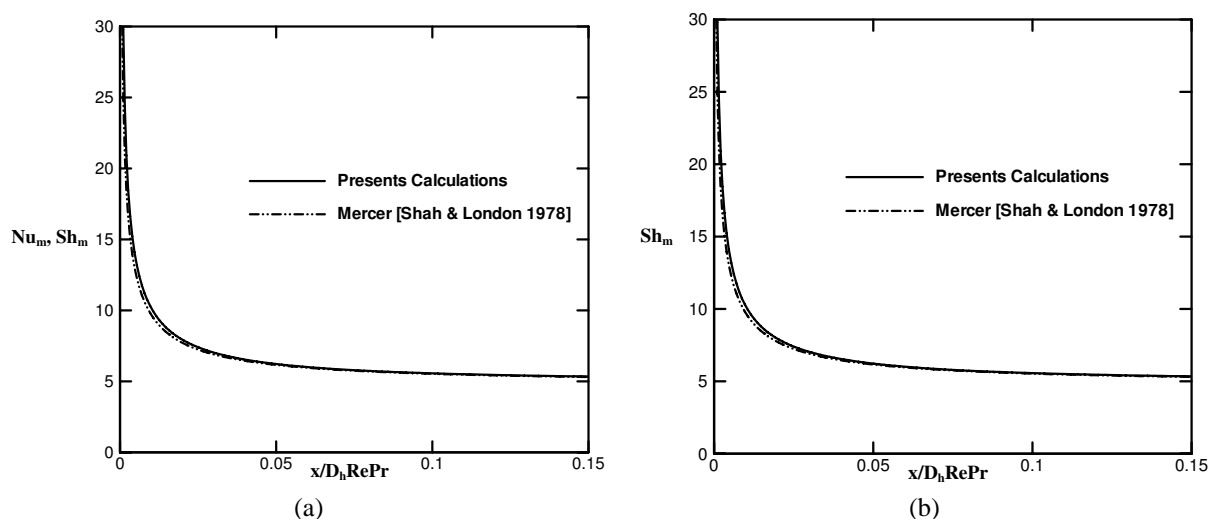
FIG. 2: (a) Mean Nusselt and Sherwood numbers; **(b)** mean Sherwood number (Sc = Pr)

$T_w = 20°C$ (hence $C_w = 14.65$ g/kg). The values of solutal and thermal Grashof number are given in Table 2. We notice that both solutal and thermal Grashof numbers are negative. Thus the last two terms in the right-hand side of Eq. (3) are negative. These terms represent the thermal and solutal buoyancy forces. It can be deduced that these forces act in the opposite direction of the upward airflow.

Figure 3 presents axial evolution of the friction factor $(f.Re_{IS})$ at the isothermal plate. We observe that $f.Re_{IS}$ diminishes rapidly near the channel inlet because of the boundary layer development. The friction factor evolution is not monotonic. Indeed, it passes by minima and then increases to asymptotic values of 19.5, 19.2, and 18.5, respectively, for $\varphi_{in} = 10\%$, 30%, and 70% at the outlet of the channel. These values are slightly different from that corresponding to a fully developed forced convection flow $f.Re = 24$ (Shah and London, 1978). This indicates that the flow field is still developing. We also note that for all the considered values of φ_{in}, $f_{IS}.Re$ becomes negatives starting from $x/L = 0.008$. These negative values of $f_{IS}.Re$ correspond to axial velocity in the opposite direction of the entering airflow (negative u). This is a flow reversal situation, which is induced by buoyancy forces.

The magnitude of these forces depends strongly on the value of φ_{in} (Table 2) and, in the same manner, the location where $f_{IS}.Re$ is negative. Negative values of $f_{IS}.Re$ occur for $0.008 < x/L < 0.335$, $0.008 < x/L < 0.390$, and $0.021 < x/L < 0.475$, respectively, for $\varphi_{in} = 10\%$, 30%, and 70%. It is important to note that the minima of $f_{IS}.Re$ occur at $x/L = 0.079$, 0.082, and 0.088, respectively, for $\varphi_{in} = 10\%$, 30%, and 70%. These minima correspond to the maximum of the buoyancy force magnitude.

Figure 4 presents the axial velocity profile at $x/L = 0.088$ which corresponds to the minimum of $f_{IS}.Re$ for $\varphi_{in} = 70\%$. This figure reveals an important effect of the inlet air humidity φ_{in}. Indeed, increasing φ_{in} gives rise to more important buoyancy forces, which affect the velocity profile. Near the left plate (the isothermal one), the flow is decelerated by these buoyancy forces, which are so important that they overcome inertia forces, and this results in an axial velocity in the opposite direction of the main upward flow (negative u). The zone where negative axial velocities prevail constitutes a recirculation cell (i.e., flow reversal zone). The dimension of this cell can be appreciated from the streamline patterns (Fig. 6). On the

TABLE 2: Grashof numbers for different values of airflow inlet relative humidity φ_{in}

φ_{in}(%)	10	30	70
C_{in} (kg/kg)	0.0196	0.0603	0.148
Gr_M	−3045	−28,262	−83,849
Gr_T	−147,611	−148,723	−151,105
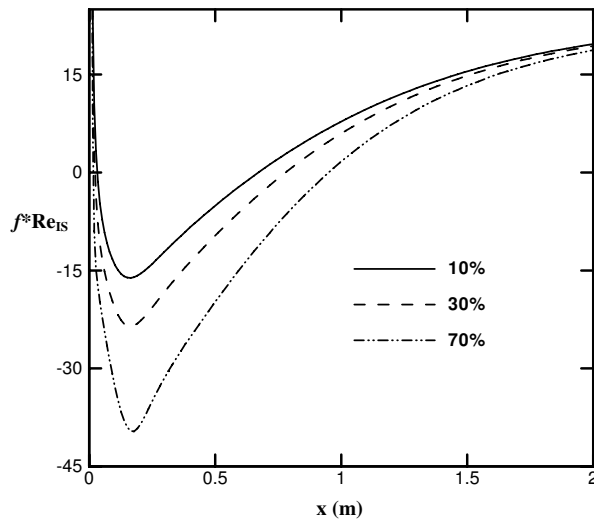
FIG. 3: Friction factor at the isothermal plate for different inlet air humidities
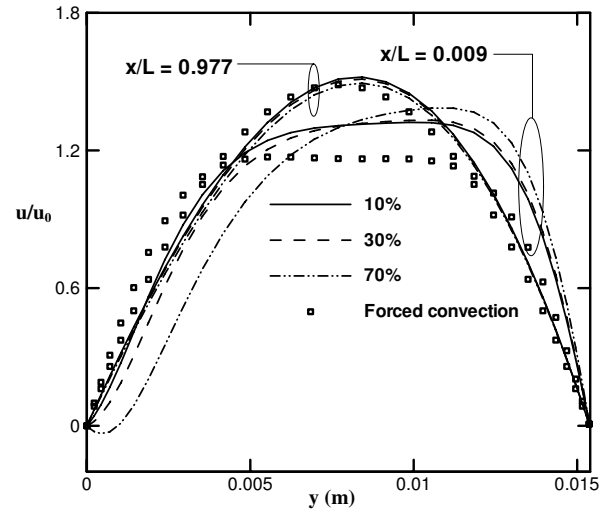
FIG. 5: Axial velocity profiles close to the channel inlet and outlet for different inlet humidities
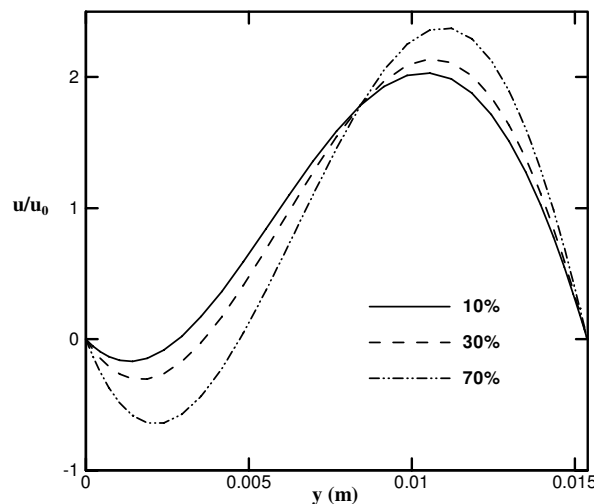
FIG. 4: Axial velocity profiles at $x/L = 0.088$ for different inlet air humidities

other hand, Fig. 4 reveals that the flow is accelerated near the right plate (the adiabatic one). This acceleration counterbalances the deceleration of airflow near the isothermal plate to satisfy the mass conservation equation.

Figure 5 shows the axial velocity profiles near the channel inlet and outlet. The case of forced convection is also reported. It is clear that inlet air humidity has an important effect on the flow. Indeed, axial velocity profiles are strongly distorted. This distortion is due to

buoyancy forces that are as strong as φ_{in} is greater. This distortion is more pronounced near the channel entrance where thermal and mass gradients are greater. Indeed, the maximum of the axial velocity is shifted to the adiabatic plate. There airflow is accelerated due its deceleration in the vicinity of the isothermal plate. Near the channel exit ($x/L = 0.977$), thermal and mass gradients diminish as air is cooled and its humidity decreases (as can be seen in Figs. 9–10). Thus the magnitude of buoyancy forces decreases and axial velocity profiles tend to the forced convection one. As it was mentioned earlier, the flow is still developing, so the fully developed profile is not yet reached.

The streamlines for $\varphi_{in} = 70\%$ are presented in Fig. 6. This figure shows the recirculation cell that is induced by buoyancy forces. The dimensions of this recirculation cell are more important as φ_{in} is increased. The eye of this recirculation cell is located at $x/L = 0.075$ and $y/L = 0.002$. This location is close to the minimum of $f_{IS}.$Re and u for $\varphi_{in} = 70\%$, as can be seen in Figs. 3 and 4.

Axial evolution of the friction factor at the adiabatic plate $f_{AD}.$Re is shown in Fig. 7. Very close to the channel entrance ($x/L < 0.006$), this friction factor diminishes abruptly and takes the same value for any air inlet humidity, as can be seen in Fig. 7 (inset). This evolution is due to the boundary layer development. In this region, the effect of inlet air humidity (and hence buoyancy forces) is weak. Beyond this region, $f_{AD}.$Re increases with the axial position until reaching a maximum at $x/L = 0.051$,
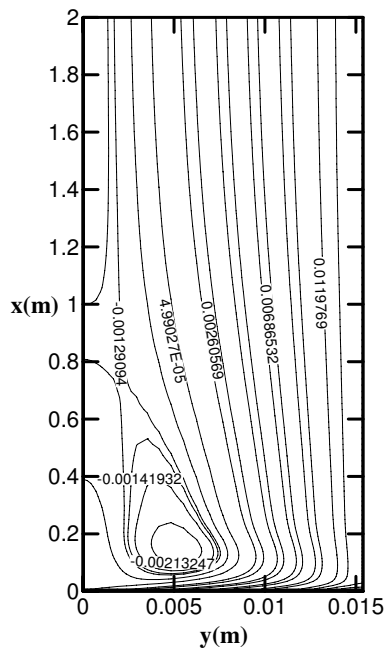
FIG. 6: Streamlines for $\varphi_{in} = 70\%$
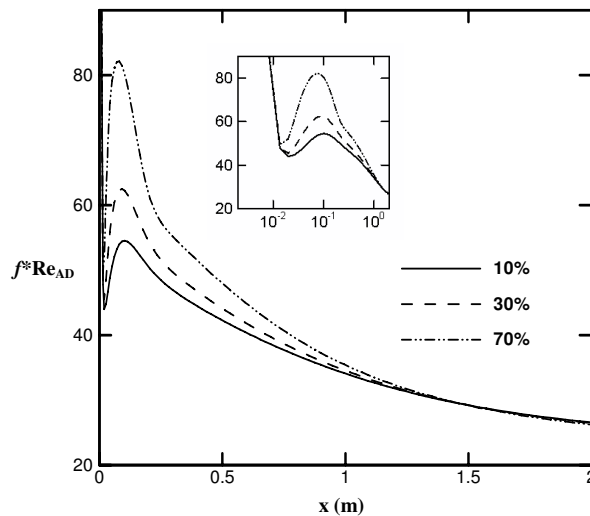
FIG. 7: Axial evolution of the friction factor at the adiabatic plate for different inlet air humidities

0.045, and 0.038, respectively, for $\varphi_{in} = 10\%$, 30%, and 70%. This increase is due to the acceleration of the flow near the adiabatic plate further to its deceleration near the isothermal one. This is a result of a momentum transfer from the isothermal plate, where the flow is decelerated,

to the adiabatic one, where it is accelerated (see axial velocity profiles in Figs. 4 and 5). The maxima of f_{AD}.Re are 54.51, 62.48, and 82.11, respectively, for $\varphi_{in} = 10\%$, 30%, and 70%. Beyond $x/L = 0.038$ and as the flow goes downstream, f_{AD}.Re decreases. Indeed, in this region, the magnitude of buoyancy forces diminishes, thus the axial velocity near the adiabatic plate is reduced (see Fig. 5). At the channel exit, f_{AD}.Re takes the values 26.61, 26.5, and 26.28, respectively, for $\varphi_{in} = 10\%$, 30%, and 70%. Again, these values are slightly different from that corresponding to fully developed forced convection, f.Re = 24 (Shah and London, 1978).

Axial evolution of mass fraction C_{AD} at the insulated plate is presented in Fig. 8. We notice that C_{AD} is essentially constant for $\varphi_{in} = 10\%$ and goes down in the other cases. Indeed, as the insulated plate is dry, its mass fraction is that of air near it. As inlet air mass fraction C_{in} is always greater than C_w (see Table 2), water vapor contained in airflow is condensed on the isothermal plate. This condensation is as intense as C_{in} (i.e., φ_{in}) is greater.

The mass flux of condensed vapor at the liquid-air interface is shown in Fig. 9. As indicated before, water vapor contained in airflow is condensed at the isothermal wetted plate in all cases. For $\varphi_{in} = 10\%$, condensed mass flux decreases rapidly and stretches to zero. This indicates that the phase change and mass transfer at the liquid-air interface are weak. Indeed, mass fractions of air at the channel entrance and at the wetted wall take very close
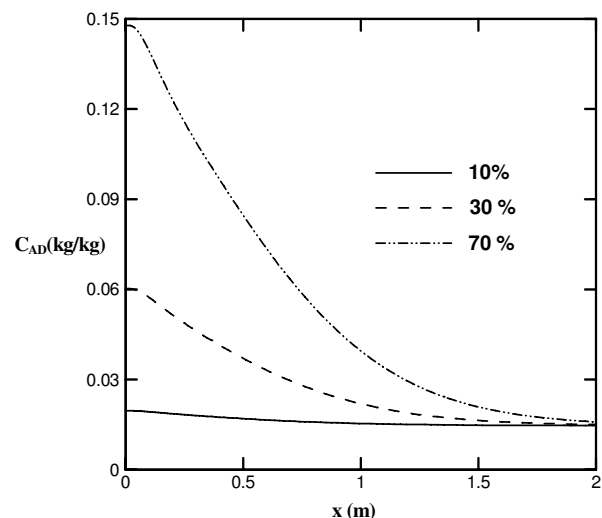
FIG. 8: Evolution of the mass fraction near the insulated plate for different inlet air humidities
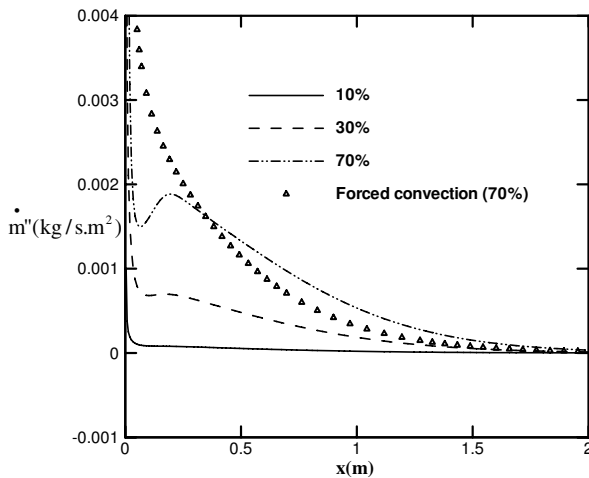
FIG. 9: Condensed mass flux at the liquid-air interface for different inlet air humidities
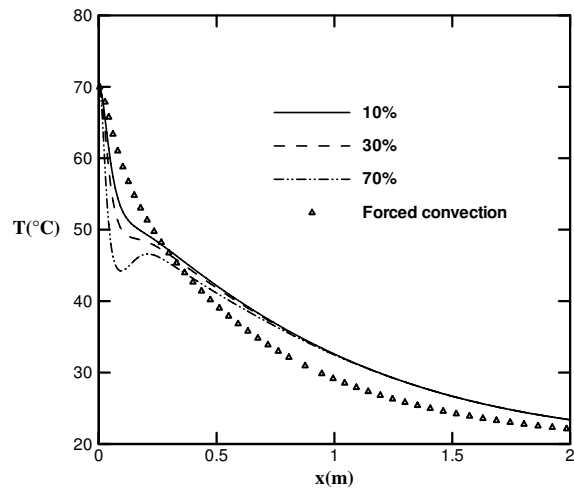
FIG. 10: Air temperature at the channel midplane $(y/L = 0.0037)$

values ($C_{in} = 19.6$ g/kg and $C_w = 14.6$ g/kg). Considering the other cases ($\varphi_{in} = 30\%$ or 70%), it is clear that the condensation phenomenon depends strongly on the air inlet humidity. In addition to its decrease (due to the boundary layer development; refer to the forced convection case), the condensed mass flux at the isothermal plate exhibits local extrema. These extrema are more pronounced as φ_{in} is increased. The local minimum of the vapor condensed mass flux occurs at $x/L = 0.038$. For $\varphi_{in} = 70\%$, this location is that of the recirculation cell eye (see Fig. 6). Thus it can be deduced that the increasing of the condensed mass flux toward its local maximum is attributed to the recirculation cell. The latter induces a fluid mixing near the isothermal plate and thus increases the condensed mass flux. This one reaches its local maximum at $x/L = 0.088$ for $\varphi_{in} = 70\%$. This location is exactly that where the friction factor at the isothermal plate exhibits its minimum. As explained before, the magnitude of buoyancy forces takes its greater value there (see Fig. 3). As the buoyancy force's magnitude decreases (beyond $x/L = 0.088$ for $\varphi_{in} = 70\%$), the recirculation cell and, as a result, the fluid mixing switch off. Thus condensed mass flux decreases due to the boundary layer development. Moreover, at the channel exit, condensed mass flux tends toward zero as the mass fraction gradient becomes blurred.

Figure 10 presents the axial development of airflow temperature at the channel midplane ($y/L = 0.0034$). The case of forced convection is reported for comparison. It is noticed that air is being cooled in all cases as

it goes downstream. This is due to a sensible heat transfer from air toward the isothermal plate. This plate has to be cooled to maintain its temperature at 20°C. As reported by Ait Hammou et al. (2004), this situation is present either in condensation or evaporation cases. The airflow temperature at the channel midplane exhibits two local extrema near the channel entrance. These extrema are more pronounced for $\varphi_{in} = 70\%$. In this case, the local minimum of air temperature is 44.24°C, which occurs at $x/L = 0.046$, and the local maximum is 46.59°C, which occurs at $x/L = 0.104$. These axial locations are nearly close to that corresponding to the local minimum and maximum of the condensed mass flux (Fig. 9). Once again, it is clear that the existence of local extrema of air temperature at the channel midplane is related to the fluid mixing induced by flow reversal near the isothermal plate. This fluid mixing increases the condensed mass flux, and thus the airflow temperature increases. Indeed, vapor condensation releases latent heat, which is partly absorbed by airflow. Moreover, near the channel inlet ($x/L < 0.046$), airflow at the channel midplane is cooler as φ_{in} is increased. In this region, the magnitude of buoyancy forces augments, and its value is greater for large values of φ_{in} (see Table 2). As these forces decelerate the upward airflow and induce flow reversal, they increase the air cooling through sensible heat transfer toward the isothermal plate. Indeed, airflow is cooler when natural convection is taken into account and if φ_{in} is increased. It should be borne in mind that flow reversal is stronger as φ_{in} is increased (see Fig. 3). Finally, at the channel exit, airflow

temperature at the channel midplane tends asymptotically to 20°C, which is the isothermal plate temperature.

Axial evolution of the insulated plate temperature T_{AD} is presented in Fig. 11. Remember that this temperature is that of airflow at its vicinity. It is clear from Fig. 11 that T_{AD} decreases as the flow goes downstream. This decrease is due to the sensible heat removed from air and transferred to the isothermal plate. A meticulous examination of Fig. 11 shows that as airflow is as cool as the air humidity at the channel inlet, φ_{in} increased. This a result of the heat transfer from the cooler isothermal plate to the insulated one induced by the fluid mixing resulting from flow reversal (Fig. 6). Close to the channel outlet, T_{AD} takes the values 24.78°C, 24.77°C, and 24.76°C, respectively, for $\varphi_{in} = 10\%$, 30%, and 70%.

Axial evolution of latent Nusselt number (Nu_L) at the isothermal plate is represented in Fig. 12. Near the channel inlet, Nu_L decreases due to the boundary layer development. Considering the case $\varphi_{in} = 10\%$, Nu_L diminishes and stretches to zero at the channel exit. As explained earlier, in this case, phase change and mass transfer at the liquid-air interface is weak (Fig. 9). The axial evolution of Nu_L for $\varphi_{in} = 10\%$ is monotonous. This is not the case for the other values of φ_{in}. Indeed, for $\varphi_{in} = 30\%$ and 70%, Nu_L exhibits a local minimum and maximum. The positions of these extrema depend on φ_{in} and are more pronounced for $\varphi_{in} = 70\%$. Equation (18) shows that Nu_L depends essentially on the mass fraction gradient, which is related to the condensed mass flux [Eq. (22)]. Thus the extrema locations of these two pa-

FIG. 12: Axial evolution of the local latent Nusselt number for different inlet air humidities

rameters are exactly the same (cf. Fig. 9). Furthermore, the development of the two parameters (Nu_L and condensed mass flux) is analogous. Thus the occurrence of the local extrema of Nu_L is due to the interaction between the condensation phenomenon and flow reversal, as explained earlier. Moreover, we notice that Nu_L (i.e., latent heat flux) increases with φ_{in}. Indeed, as φ_{in} rises, mass fraction at the channel inlet (C_{in}) and then latent heat flux related to vapor condensation increase.

Figure 13 presents the axial evolution of sensible Nusselt number (Nu_s) at the isothermal plate. This plate is wetted by a thin liquid water film and maintained at a temperature $T_w = 20°C$, which is lower than that of the airflow at the channel entrance ($T_{in} = 70°C$). So airflow is cooled. A comparison of Fig. 13 and Fig. 12 reveals that the effect of inlet air humidity φ_{in} on Nu_s is less important than its effect on Nu_L. This is explained by Eq. (16), which shows that Nu_s is not directly affected by the mass fraction contrary to Nu_L. On the other hand, the evolution of Nu_s presents a minimum whose location depends slightly on φ_{in}. This minimum is due to the buoyancy force effects, which decelerate the airflow near the isothermal plate (as shown in Fig. 3) and thus diminish the sensible heat transfer. It is important to note that the minimum of Nu_s is observed at $x/L = 0.054$, 0.043, and 0.027, respectively, for $\varphi_{in} = 10\%$, 30%, and 70%. Finally, at the channel exit, Nu_s takes the values 4.69, 4.69, and 4.67 for $\varphi_{in} = 10\%$, 30%, and 70%, respectively.

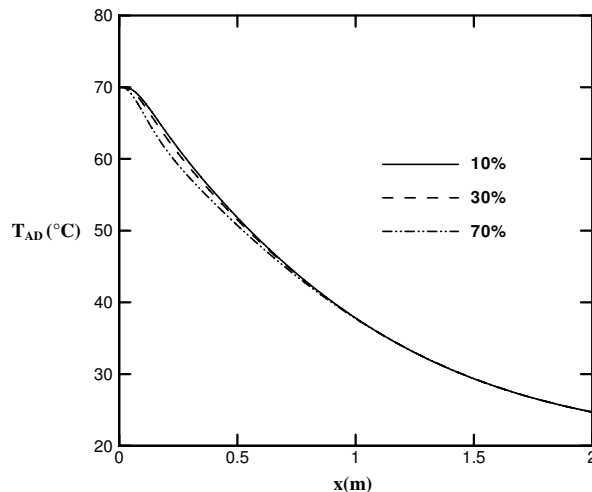**FIG. 11:** Axial evolution of the insulated plate's temperature for different inlet air humidities
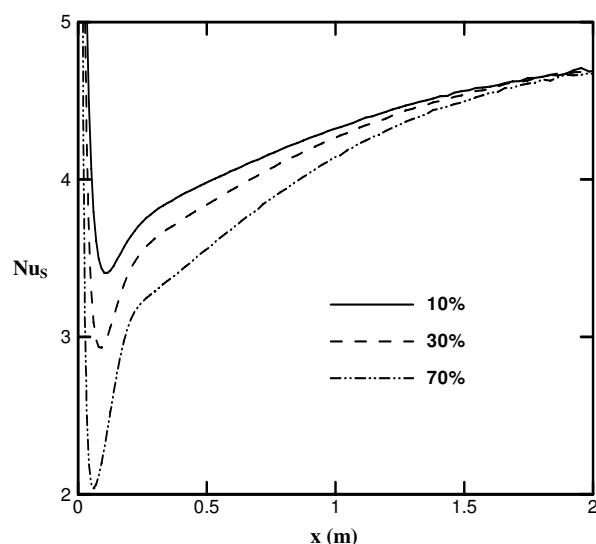
FIG. 13: Axial evolution of the local sensible Nusselt number for different inlet air humidities

These values are close to 4.86, which corresponds to a fully developed forced convection flow (Shah and London, 1978).

Sherwood number Sh characterizes mass transfer between liquid film streaming on the isothermal plate and the airflow. The axial evolution of Sh near the isothermal plate is shown in Fig. 14. An analysis of this figure shows that Sh evolution is not monotonous. Indeed, at the inlet
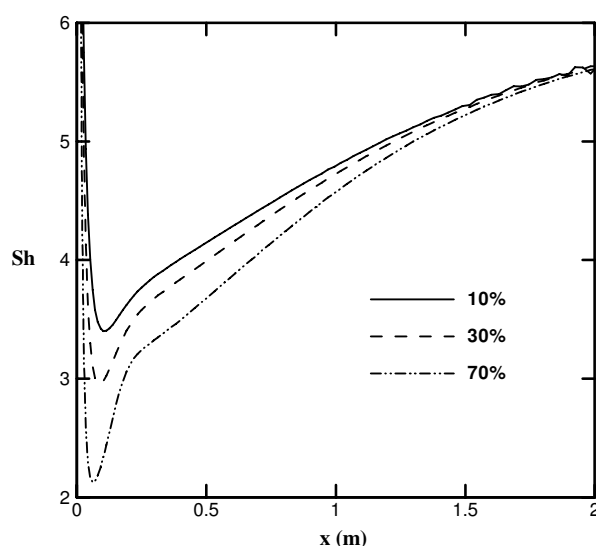
FIG. 14: Axial evolution of the local Sherwood number for different inlet air humidities

of the channel, Sh takes important values because of the important gradient of mass fraction. It is important to note that the minimum of Sh is noted at $x/L = 0.054$, 0.043, and 0.027, respectively, for $\varphi_{in} = 10\%$, 30%, and 70%. It is clear that Sh presents the same evolution as Nu_s; indeed, Prandtl and Schmidt numbers take very close values in the present study (Pr = 0.707 and Sc = 0.603). Furthermore, at the channel exit, Sh takes the values 5.62, 5.60, and 5.58 for $\varphi_{in} = 10\%$, 30%, and 70%, respectively. Again it should be pointed out that these values are close to the fully developed forced convection value (Shah and London, 1978).

4. CONCLUSIONS

Combined heat and mass transfer with phase change in a vertical parallel-plate channel has been studied numerically. One of the plates is wetted by a thin liquid water film and maintained at a constant temperature while the other is dry and thermally insulated. Based on our results, the following conclusions can be drawn.

1. Buoyancy forces, which act in the opposite direction of the upward airflow, slow down the flow and give rise to a flow reversal near the isothermal plate. A recirculation cell appears near this plate. The dimensions of this cell depend strongly on the conditions at the channel inlet. Indeed, as the inlet air humidity increases, the recirculation cell resulting occupies a large part of the channel length.

2. Water vapor is removed from airflow and condensed on the isothermal plate. The recirculation cell introduces a fluid mixing between the fluid at the channel axis and that near the isothermal plate. This fluid mixing intensifies water vapor condensation. Owing to the flow deceleration near the isothermal plate, the condensed mass flux is diminished.

3. Increasing the inlet air humidity decreases slightly the sensible heat transfer while it augments considerably the latent heat transfer. As the inlet air humidity increases, latent Nusselt number increases due to the intensification of water vapor condensation.

It should be noted that in all studied cases, water vapor is condensed on the isothermal plate, so the film thickness would increase. Thus the assumption of zero film thickness may be inappropriate; this point will be considered in the near future by handling the liquid film thickness in our mathematical model.

ACKNOWLEDGMENTS

REFERENCES

Ait Hammou, Z., Benhamou, B., Galanis, N., and Orfi, J., Laminar mixed convection of humid air in a vertical channel with evaporation or condensation at the wall, *Int. J. Thermal Sci.,* vol. **43**, pp. 531–539, 2004.

Azizi, Y., Benhamou, B., Galanis, N., and El-Ganaoui, M., Buoyancy effects on upward and downward laminar mixed convection heat and mass transfer in a vertical channel, *Int. J. Numer. Method Heat Fluid Flow*, vol. **17**, pp. 333–353, 2007.

Boulama, K. and Galanis, N., Analytical solution for fully developed mixed convection between parallel vertical plates with heat and mass transfer, *J. Heat Transfer*, vol. **126**, pp. 381–388, 2004.

Burmeister, L. C., *Convective Heat Transfer*, 2nd ed., McGraw-Hill, New York, 1993.

Chow, L. C. and Chung, J. N., Evaporation of water into laminar stream of air and superheated steam, *Int. J. Heat Mass Transfer*, vol. **26**, pp. 373–380, 1983.

Feddaoui, M., Mir, A., and Belahmidi, E., Numerical simulation of mixed convection heat and mass transfer with liquid film cooling along an insulated vertical channel, *Int. J. Heat Mass Transfer*, vol. **39**, pp. 445–453, 2003.

Fedorov, A. G., Viskanta, R., and Mohamad, A. A., Turbulent heat and mass transfer in an asymmetrically heated, vertical parallel-plate channel, *Int. J. Heat Fluid Flow*, vol. **18**, pp. 307–315, 1997.

Fuji, T., Kato, Y., and Bihara, K., Expressions of transport and thermodynamic properties of air, steam and water, Sei San Ka Gaku Ken Kuu Jo report 66, Kyu Shu University, Kyu Shu, Japan, 1997.

Gebhart, B. and Pera, L., The nature of vertical natural convection flows resulting from the combined buoyancy effects of thermal and mass diffusion, *Int. J. Heat Mass Transfer*, vol. **14**, pp. 2025–2050, 1971.

Jang, J.-H. and Yan, W-M., Thermal protection with liquid film in turbulent mixed convection channel flows, *Int. J. Heat Mass Transfer*, vol. **49**, pp. 3645–3654, 2006.

Lin, J. N., Tzeng, P. Y., Chou, F. C., and Yan, W. M., Convective instability of heat and mass transfer for laminar forced convection in the thermal entrance region of horizontal rectangular channels, *Int. J. Heat Fluid Flow*, vol. **13**, pp. 250–258, 1992.

Patankar, S. V., *Numerical Heat Transfer and Fluid Flow*, Hemisphere/McGraw-Hill, New York, 1980.

Patankar, S. V., A calculation procedure for two-dimensional elliptic situations, *Numer. Heat Transfer*, vol. **4**, pp. 409–425, 1981.

Salah El-Din, M. M., Fully developed forced convection in a vertical channel with combined buoyancy forces, *Int. Commun. Heat Mass Transfer*, vol. **19**, pp. 239–248, 1992.

Shah, R. K. and London, A. L., *Laminar Flow Forced Convection in Ducts*, Academic, New York, 1978.

Siow, E. C., Ormiston, S. J., and Soliman, H. M., Two-phase modelling of laminar film condensation from vapour-gas mixtures in declining parallel-plate channels, *Int. J. Thermal Sci.*, vol. **46**, pp. 458–466, 2007.

Tsay, H. C. and Yan, W. M., Binary diffusion and heat transfer in laminar mixed convection channel flows with uniform wall heat flux: Extremely thin film thickness, *Warme-Stoffubertragung*, vol. **26**, pp. 23–31, 1990.

Tsay, Y. L., Lin, T. F., and Yan, W. M., Cooling of a falling liquid film through interfacial heat and mass transfer, *Int. J. Multiphase Flow*, vol. **16**, pp. 853–865, 1990.

Yan, W. M., Effects of film evaporation on laminar mixed convection heat and mass transfer in a vertical channel, *Int. J. Heat Mass Transfer*, vol. **35**, pp. 3419–3429, 1992.

Yan, W. M., Mixed convection heat transfer in a vertical channel with film evaporation, *Can. J. Chem. Eng.*, vol. **71**, pp. 54–62, 1993.

Volchkov, E. P., Terekhov, V. V., and Terekhov, V. I., A numerical study of boundary layer heat and mass transfer in a forced convection of humid air with surface steam condensation, *Int. J. Heat Mass Transfer*, vol. **47**, pp. 1473–1481, 2004.

RANS SIMULATION OF EFFECT OF EVAPORATING DROPLETS ON A TURBULENT HEAT TRANSFER IN A MIST FLOW IN A SUDDEN PIPE EXPANSION

M. A. Pakhomov & V. I. Terekhov*

Kutateladze Institute of Thermophysics, Laboratory of Thermal and Gas Dynamics, Russian Academy of Sciences, Siberian Branch, 630090, 1, Acad. Lavrent'ev Avenue, Novosibirsk, Russia

*Address all correspondence to V. I. Terekhov E-mail: terekhov@itp.nsc.ru

A mathematical model of the two-phase mist flow past a sudden pipe expansion using the Eulerian/Eulerian approach was developed in the case of water and ethanol droplets. The effect of mass concentration of droplets and their size on the structure of the separation flow region and on the heat transfer were analyzed in detail. The results obtained are compared with previously experimental and numerical data for two-phase flows developing downstream of sudden pipe expansion.

KEY WORDS: *gas droplet flow, heat and mass transfer, droplet evaporation*

1. INTRODUCTION

Sudden expansion pipe with detached flows is encountered frequently in technical applications. The detachment affects momentum, heat, and mass transfer processes and to a large extent determines the turbulent flow structure. Knowledge of the turbulent flow field and heat transfer in sudden expansion flows is important from both theoretical and practical points of view. Sudden pipe expansions are normally used to stabilize flame in combustion chambers. Other numerous applications of sudden pipe expansions imply their use as step diffusers or as heat transfer intensifiers in ducted flows. Thus such flows have become a subject of many extensive studies. Studies of one-phase separated flows past a backward-facing step were reported in many publications, which are reviewed by Eaton and Johnston (1981), Alemasov et al. (1989), Simpson (1996), and Ota (2000).

Two-phase separated flows have been found in many technical applications. The effect of solid or liquid particles becomes more pronounced with increasing size and concentration of the particles. Detailed information concerning the turbulent flow structure, the velocities, and temperatures of the phases and the distribution of par-

ticles over the pipe cross section are important matters for optimization of evaporation/combustion processes. Two-phase separated flows with solid particles behind a backward-facing step or a sudden pipe expansion were investigated by Ruck and Makiola (1988), Hardalupas et al. (1992), Volkov et al. (1994), Zaichik et al. (1994, 1997), Founti and Klipfel (1998), Fessler and Eaton (1999), Zhang et al. (2001), Yua et al. (2004), and Terekhov and Pakhomov (2008, 2009). These authors showed that light particles are entrained in the circulating flow, whereas heavy particles escape trapping in the separation zone and present only in the shear flow region. In the wall zone, dispersed impurities are accumulated.

Zaichik et al. (1994, 1997) were among the first workers who used the Eulerian/Eulerian approach in computation of gas-particle separated flows. The results obtained by these authors fairly well agree with experimental data obtained for two-phase flows past a backward-facing step and sudden pipe expansion. It should be noted that in latter studies, gas flow laden with solid particles was examined.

The only one study on the flow with evaporating liquid droplets past a backward-facing step was the experimental work by Hishida et al. (1995). In this paper,

NOMENCLATURE

		Greek Symbols	
C_D	drag coefficient of evaporating droplets	Φ	volume concentration of particles
D_{Lij}	tensor turbulent diffusion of particles (m²/s)	ε	dissipation of the turbulent kinetic energy (m²/s³)
d	droplet diameter (m)		
ER	$= (R_2/R_1)^2$ expansion ratio	τ	$= \rho_L d^2/(18\mu W)$, $\tau_\Theta = C_{pL}\rho_L d^2/(12\lambda Y)$
H	step height (m)		particle dynamics and thermal relaxation time (s)
J	mass flux of vapor from the surface of evaporating drop [kg/(m²s)]		

C_D drag coefficient of evaporating droplets
D_{Lij} tensor turbulent diffusion of particles (m²/s)
d droplet diameter (m)
ER $= (R_2/R_1)^2$ expansion ratio
H step height (m)
J mass flux of vapor from the surface of evaporating drop [kg/(m²s)]
$K_A,$ mass concentration of air and vapor,
K_V respectively, in binary vapor-air mixture
K_{VS} mass concentration of vapor at the drop surface and evaporating corresponding to saturation parameters at the drop temperature T_L
M_L mass concentration of droplets
$\bar{R}$ absolute gas constant [J/(mol K)]
$\langle uv \rangle$ $= -\nu_T(\partial U/\partial r)$, $\langle u_L v_L \rangle$ turbulent stresses in gas and dispersed phases (m²/s²)
W $= \left(1 + \text{Re}_L^{2/3}/6\right)$
x_R reattachment length (m)
Y $= \left(1 + 0.3\text{Re}_L^{1/2}\,\text{Pr}^{1/3}\right)$

Greek Symbols
Φ volume concentration of particles
ε dissipation of the turbulent kinetic energy (m²/s³)
τ $= \rho_L d^2/(18\mu W)$, $\tau_\Theta = C_{pL}\rho_L d^2/(12\lambda Y)$ particle dynamics and thermal relaxation time (s)

Subscripts
0 parameter at the axis of the pipe
1 parameter under inlet conditions
A air
fd full developed
i current calculation cross section along the axial direction
$i-1$ previous calculation cross section along the axial direction
L dispersed phase
P particle
T turbulent parameter
V vapor

measurements were performed using the phase Doppler anemometer (PDA) method. Measured were the velocities and turbulent kinetic energies of the two phases, the mass flow rate of the droplet flow, and the heat transfer coefficient from the heated wall to the two-phase flow. The purpose of this study is the development of the mathematical model and the numerical examination of the influence of key parameters of the two-phase flow, namely, the mass concentration of liquid droplets and the droplet size, on heat transfer.

2. PROBLEM STATEMENT

In this paper, evolution of a downward gas-droplet turbulent flow in the downstream region of a sudden pipe expansion was examined. A schematic of the sudden expansion gas-droplet flow is shown in Fig. 1. The volumetric dispersed phase fraction was small ($\Phi_1 < 10^{-4}$) and the droplets ($d_1 < 100\mu$m) so that, according to Volkov et al. (1994), the effects due to interparticle collisions
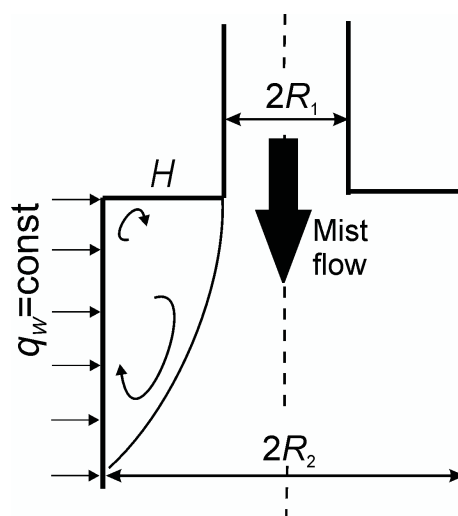

FIG. 1: Schematic of the sudden expansion gas droplet flow

could be neglected. All computations were performed for monodispersed gas-droplet flow and a uniform wall heat flux ($q_W = 1$ kW/m^2). The pipe surface was dry so that no liquid film from deposited droplets formed on the wall. This assumption for heated channels was allowable (see Mastanaiah and Ganic, 1981). This condition is valid if the wall temperature is $40°$C superheated. The droplet temperature is assumed to be uniform over the droplet radius.

3. MATHEMATICAL MODEL

The momentum, heat, and mass transfer processes in the gas and dispersed phases were treated using the Eulerian/Eulerian approach. This approach is based on using the kinetic equation of probability density function for the coordinates, velocities, and temperatures of droplets in the turbulent flow (Derevich and Zaichik, 1988).

3.1 Governing Equations for Heat and Mass Transfer in the Gas Phase

The system of Reynolds-averaged Navier-Stokes equations for a two-phase steady state axisymmetric flow with ignored mass forces has the form (Terekhov and Pakhomov, 2009)

$$\rho \frac{\partial U_j}{\partial x_j} = \frac{6J\Phi}{d}$$

$$\rho \frac{\partial (U_j U_i)}{\partial x_j} = -\frac{\partial (P + 2k/3)}{\partial x_i} + \frac{\partial}{\partial x_j}$$
$$\times \left[(\mu + \mu_T) \left(\frac{\partial U_i}{\partial x_j} + \frac{\partial U_j}{\partial x_i} \right) \right]$$
$$- (U_i - U_{Li}) \frac{\Phi}{d} \left[\frac{1}{8} C_D \rho \, |\mathbf{U} - \mathbf{U}_L| + J \right]$$
$$+ \rho_L g_u < u_i u_j > \frac{\partial \Phi}{\partial x_j}$$

$$\rho \frac{\partial (U_j T)}{\partial x_j} = \frac{\partial}{\partial x_j} \left(\frac{\mu}{\mathrm{Pr}} + \frac{\mu_T}{\mathrm{Pr}_T} \right) \frac{\partial T}{\partial x_j}$$
$$- \frac{6\Phi}{C_P d} \left[\alpha \left(T - T_L \right) + JL \right]$$
$$+ \frac{\rho D_T}{C_P} (C_{PV} - C_{PA}) \left(\frac{\partial K_V}{\partial x_i} \frac{\partial T}{\partial x_i} \right)$$
$$+ \frac{C_{PL} \rho_L \tau g_{ut}}{C_P} < u_j t > \frac{\partial \Phi}{\partial x_j}$$

$$\frac{\partial (U_j K_V)}{\partial x_j} = \frac{\partial}{\partial x_j} \left[\left(\frac{\nu}{Sc} + \frac{\nu_T}{Sc_T} \right) \frac{\partial K_V}{\partial x_j} \right] + \frac{6J\Phi}{\rho d}$$

$$\rho = P / \left(\bar{R} T \right) \qquad (1)$$

Here C_D is the evaporating droplet drag coefficient by Mastanaiah and Ganic (1981):

$$C_D = \frac{C_{DP}}{1 + C_p(T - T_L)/L}$$

where C_{DP} is the coefficient of resistance of nonevaporating particles, which can be calculated from the relations presented by Clift et al. (1978):

$$C_{DP} = \begin{cases} 24/\mathrm{Re}_L, & \mathrm{Re}_L \leq 1 \\ 24/\mathrm{Re}_L \left(1 + 0.15\mathrm{Re}_L^{0.687} \right), & \mathrm{Re}_L > 1 \end{cases}$$

$\mathrm{Re}_L = (\mathbf{U} - \mathbf{U}_L) \, d/\nu$ the particle Reynolds number; J is the mass flux of vapor from the surface of an evaporating droplet; K_V is the mass vapor concentration in the binary vapor-gas mixture; and $\bar{R}$ is the gas constant. The turbulent Prandtl and Schmidt numbers were assumed constant, equal to $\mathrm{Pr}_T = \mathrm{Sc}_T = 0.85$.

The equation for mass flux of vapor from the surface of evaporating droplet can be written as

$$J = JK_{VS} - \rho D \frac{\partial K_{VS}}{\partial r}$$

The first term on the right-hand side describes convective vapor flux, and the second is the diffusivity vapor flux.

Turbulent Reynolds stresses and turbulent heat and mass fluxes in the gas phase were determined according to the Boussinesq hypothesis; they have the form

$$- <u_i u_j> = \nu_T \left(\frac{\partial U_i}{\partial x_j} + \frac{\partial U_j}{\partial x_i} \right) - \frac{2}{3} k \delta_{ij}$$

$$<u_j t> = -\frac{\nu_T}{\mathrm{Pr}_T} \frac{\partial T}{\partial x_j}, \quad <u_j k_V> = -\frac{\nu_T}{\mathrm{Sc}_T} \frac{\partial K_V}{\partial x_j}$$

Here δ_{ij} is the Kronecker delta and μ_T is the turbulent dynamic viscosity.

3.2 Two-Equations Turbulence Model

The equations for the turbulent kinetic energy k and for the dissipation rate $\tilde{\varepsilon}$ modified to the case of a two-phase particle laden flow can be written as

$$\frac{\partial (U_j k)}{\partial x_j} = \frac{\partial}{\partial x_j} \times \left[\left(\nu + \frac{\nu_T}{\sigma_k} \right) \frac{\partial k}{\partial x_j} \right] - \frac{1}{2} \frac{\partial}{\partial x_j}$$
$$\times \left[\nu \frac{k}{\varepsilon} \frac{\partial \hat{\varepsilon}}{\partial x_j} \right] + \Pi - \varepsilon + S_k/\rho$$

$$\frac{\partial (U_j \tilde{\varepsilon})}{\partial x_j} = \frac{\partial}{\partial x_j} \left[\left(\nu + \frac{\nu_T}{\sigma_\varepsilon} \right) \frac{\partial \tilde{\varepsilon}}{\partial x_j} \right] + \frac{\partial}{\partial x_j} \left(\nu \frac{\tilde{\varepsilon}}{k} \frac{\partial k}{\partial r} \right)$$

$$+ \frac{\tilde{\varepsilon}}{k} \left(C_{\varepsilon 1} f_1 \Pi - C_{\varepsilon 2} \tilde{\varepsilon} f_2 \right) + S_\varepsilon / \rho \qquad (2)$$

$$\nu_T = \frac{C_\mu f_\mu}{1 + \left(\Pi/\tilde{\varepsilon} - 1 - A_k/\tilde{\varepsilon} \right)/E} \cdot \frac{k^2}{\tilde{\varepsilon}} \qquad (3)$$

The constants and the damping functions were adopted by Hwang and Lin (1998): $C_\mu = 0.09$, $\sigma_k = 1.4 - 1.1 \exp\left[-(0.1 y_\lambda)\right]$, $\sigma_\varepsilon = 1.3 - \exp\left[-(0.1 y_\lambda)\right]$, $C_{\varepsilon 1} = 1.44$, $C_{\varepsilon 2} = 1.92$, $f_1 = f_2 = 1$, and $f_\mu = 1 - \exp\left(-0.01 y_\lambda - 0.008 y_\lambda^3\right)$; here $y_\lambda = y/\sqrt{\nu k/\tilde{\varepsilon}}$ is the Taylor microscale, $\Pi = - < u_i' u_j' > \partial U_i/\partial x_j$ is the rate of turbulent kinetic energy production from the average motion of the gaseous phase, $\varepsilon = \tilde{\varepsilon} + \hat{\varepsilon}$, and $\hat{\varepsilon} = 2\nu \left(\partial \sqrt{k}/\partial r \right)^2$ is the rate of dissipation of the turbulence kinetic energy in the wall zone.

The adoption of the Taylor microscale y_λ in the damping functions and the inclusion of pressure diffusion terms in both the k and $\tilde{\varepsilon}$ equations were key features of the Hwang and Lin (1998) model. The designed model not only conforms with the near-wall characteristics obtained from direct numerical simulation (DNS) data but also possesses correct asymptotic behaviors in the vicinity of the solid wall. The performance of the model of Hwang and Lin (1998) is assessed by comparison with the experiments of the backward-facing step flow with the heat transfer of Vogel and Eaton (1985). The present model predicted correctly the skin friction and heat transfer between the wall and the airflow.

In Eq. (3), $E = 2$ is the constant in the Rotta approximation for the correlations of pressure pulsations with deformation rate (see Lumley, 1980). With $\Pi/\tilde{\varepsilon} = 1$ and $_k = 0$, expression (4) yields the classical expression $\nu_T = C_\mu f_\mu k^2/\tilde{\varepsilon}$ in the turbulence model. The minimum admissible value of E is unity (see Gatski and Speziale, 1993). With $E = 1$, Eq. (3) reduces to $\nu_T = C_\mu f_\mu k^2/\Pi$ (see Lumley, 1980). In the present study, with due consideration given to data reported by Volkov et al. (1994), the value $E = 2$ was adopted. Relation (3) results when one expands the system of implicit algebraic equations for Reynolds stresses in terms of the mean velocity gradient (see Lumley, 1980; Gatski and Speziale, 1993; Volkov et al., 1994). This modification of Eq. (3) keeps the turbulence equations unchanged. Here the coefficient $_k$ stands to allow for the influence of droplets on the shear stresses (see Volkov et al., 1994). The terms S_k and S_ε characterize the additional dissipation of the gas-phase turbulence due to fine evaporating particles present in the flow and due to the nonuniform particle concentration profile; for

these terms, expressions previously used by Terekhov and Pakhomov (2005) were adopted.

3.3 Dispersed Phase

The system of mean equations governing transport processes in the dispersed phase has the form (Terekhov and Pakhomov, 2009)

$$\frac{\partial U_{Lj}}{\partial x_j} = -\frac{6 J \Phi}{d}$$

$$\rho_L \frac{\partial (\Phi U_{Lj} U_{Li})}{\partial x_j} + \rho_L \frac{\partial (\Phi < u_{Li} u_{Lj} >)}{\partial x_j}$$

$$= \Phi (U_i - U_{Li}) \frac{\rho_L}{\tau} + \Phi \rho_L g - \frac{\rho_L}{\tau} \frac{\partial (D_{Lij} \Phi)}{\partial x_j}$$

$$\rho_L \frac{\partial (\Phi U_j T_{Li})}{\partial x_j} + \rho_L \frac{\partial}{\partial x_j} \left(\Phi < \theta u_{Lj} > \right)$$

$$= \Phi (T_i - T_{Li}) \frac{\rho_L}{\tau_\Theta} - \frac{\rho_L}{\tau_\Theta} \frac{\partial \left(D^\Theta_{Lij} \Phi \right)}{\partial x_j} \qquad (4)$$

3.4 Reynolds Stress Mode, Equations for the Temperature Fluctuations, and Turbulent Heat Flux in the Dispersed Phase

The Reynolds stresses, velocity, temperature fluctuations, and the correlations between velocity and temperature fluctuations were calculated using the equations by Simonin (1991). The velocity and temperature fluctuations, and also the correlations between these fluctuations, were calculated using the equations by Volkov et al. (1994) and Derevich (2002):

$$\underbrace{U_{Lk} \frac{\partial \langle u_{Li} u_{Lj} \rangle}{\partial x_k}}_{\text{I}} + \underbrace{\frac{1}{\Phi} \left\{ \frac{\partial}{\partial x_k} \left(\Phi \langle u_{Li} u_{Lj} u_{Lk} \rangle \right) \right\}}_{\text{II}}$$

$$+ \underbrace{\langle u_{Li} u_{Lk} \rangle \frac{\partial U_{Lj}}{\partial x_k} + \langle u_{Lj} u_{Lk} \rangle \frac{\partial U_{Li}}{\partial x_k}}_{\text{III}}$$

$$= \underbrace{\frac{2}{\tau} \left(f_u \langle u_i u_j \rangle - \langle u_{Li} u_{Lj} \rangle \right)}_{\text{IV}}$$

$$\underbrace{U_{Lk}\frac{\partial \langle \theta_L^2 \rangle}{\partial x_k}}_{\text{I}} + \underbrace{\frac{1}{\Phi}\left\{\frac{\partial}{\partial x_k}\left(\Phi \langle u_{Lk}\theta_L^2 \rangle\right)\right\}}_{\text{II}}$$

$$+ \underbrace{2\langle u_{Lk}\theta_L \rangle\frac{\partial T_L}{\partial x_k}}_{\text{III}} = \underbrace{\frac{2}{\tau_\Theta}\left(f_{ut}\langle t^2 \rangle - \langle \theta_L^2 \rangle\right)}_{\text{IV}}$$

$$\underbrace{U_{Lk}\frac{\partial \langle \theta_L u_{Lj} \rangle}{\partial x_k}}_{\text{I}} + \underbrace{\frac{1}{\Phi}\left\{\frac{\partial}{\partial x_k}\left(\Phi \langle u_{Li}u_{Lk}\theta_L \rangle\right)\right\}}_{\text{II}}$$

$$+ \underbrace{\langle u_{Li}u_{Lk} \rangle\frac{\partial T_L}{\partial x_k} + \langle u_{Lk}\theta_L \rangle\frac{\partial U_{Li}}{\partial x_k}}_{\text{III}} \qquad (5)$$

$$= \underbrace{\left(\frac{f_{\Theta u}}{\tau} + \frac{f_{u\Theta}}{\tau_\Theta}\right)\langle u_i t \rangle - \left(\frac{1}{\tau} + \frac{1}{\tau_\Theta}\right)\langle \theta_L u_{Lj} \rangle}_{\text{IV}}$$

Here $D_{Lij} = \tau\left(<u_{Li}u_{Lj}> + g_u <u_i u_j>\right)$, $D^{\Theta}_{Lij} = \tau_\Theta <t_L u_{Lj}> + \tau g^{<}_{u\theta} tu_j>$ are tensors of turbulent diffusion and turbulent heat flux of particles, respectively (Zaichik et al., 1997). Also $f_u = 1 - \exp(-\Omega^{\varepsilon L}/\tau)$, $f_{ut} = f_{\Theta u} = 1 - \exp(-\Omega^{tL}/\tau_\Theta)$, $g_{u\Theta} = \Omega^{tL}/\tau - f_{u\theta}$, and $f_{u\Theta} = 1 - \exp(-\Omega^{tL}/\tau)$ are coefficients of droplet entrainment into a large-eddy fluctuational motion of the gas phase, $g_u = \Omega^{\varepsilon L}/\tau - f_u$, where $\Omega^{\varepsilon L}$ is the interaction time between the droplet and eddy (Derevich, 2002):

$$\Omega^{\varepsilon L} = \begin{cases} \Omega^E, & |\mathbf{U} - \mathbf{U}_L|\,\Omega^E \leq \Gamma^E \\ \Gamma^E/|\mathbf{U} - \mathbf{U}_L|, & |\mathbf{U} - \mathbf{U}_L|\,\Omega^E > \Gamma^E \end{cases}$$

where $\Gamma^E = 2\left(<u^2>\right)^{1/2}\cdot\Omega^{Lag}$ is integral length scale of the turbulent eddy (Derevich, 2002); $\Omega^{Lag} = 0.608\Omega^E$ and $\Omega^E = 0.22\,k/\tilde{\varepsilon}$ are Lagrangian and Eulerian integral time scales (Simonin, 1991); and Ω^{tL} is the interaction time between the droplet and thermal eddy. We assumed that $\Omega^{tL} \approx \Omega^{\varepsilon L}$ (see Terekhov and Pakhomov, 2005).

In system (5), convective transport of fluctuations and temperature (I), diffusion (II), production of fluctuations from gradients of dispersed phase average motion and temperature (III), and the interaction between the phases (IV) are taken into account. To determine the diffusion member in Eq. (5), we use the algebraic equation for the third moments:

$$\langle u_{Li}u_{Lj}u_{Lk} \rangle = -\frac{1}{3}\left(D_{Lkn}\frac{\partial \langle u_{Li}u_{Lj} \rangle}{\partial x_n}\right.$$

$$\left. + D_{Ljn}\frac{\partial \langle u_{Li}u_{Lk} \rangle}{\partial x_n} + D_{Lin}\frac{\partial \langle u_{Lj}u_{Lk} \rangle}{\partial x_n}\right).$$

$$\langle \theta_L^2 u_{Lk} \rangle = -\frac{1}{\tau + 2\tau_\Theta}\left(\tau_\Theta D_{Lik}\frac{\partial \langle \theta_L u_{Lj} \rangle}{\partial x_k}\right.$$

$$\left. + \tau_\Theta D_{Ljk}\frac{\partial \langle \theta_L u_{Li} \rangle}{\partial x_k} + \tau D_{Lk}\frac{\partial \langle u_{Li}u_{Lj} \rangle}{\partial x_k}\right)$$

$$\langle \theta_L u_{Li}u_{Lk} \rangle = -\frac{1}{2\tau + \tau_\Theta}\left(\tau_\Theta D_{Lik}\frac{\partial \langle u_{Li}u_{Lj} \rangle}{\partial x_k}\right.$$

$$\left. + 2\tau_\Theta D_{Lk}\frac{\partial \langle \theta_L u_{Li} \rangle}{\partial x_k}\right) \qquad (6)$$

Correlation (6) was obtained at the neglect of small members, determinant for convective transfer, and production of the third moments of velocity pulsations for the account of the averaged velocity gradients of the disperse phase. The heat and mass transfer model for a single droplet was described in detail (e.g., see Terekhov and Pakhomov, 2005).

4. NUMERICAL REALIZATION, BOUNDARY CONDITIONS, AND TESTING OF THE MODEL

The numerical solution was obtained using the finite volume method of Patankar (1980). To convective terms in differential equations, the QUICK procedure was applied (Leonard, 1979). The diffusion fluxes were written using central differences. The pressure field was corrected by the finite-volume SIMPLEC procedure (Van Doormaal and Raithby, 1984). A computational grid was nonuniform both in the axial and radial directions. Refining the grid was applied in the recirculation zone, in the flow detachment region, and in the reattachment zone. All computations were performed on the grid with 350×120 control volumes (CVs). Additionally, a series of test computations for a gas-droplet flow with wall droplet evaporation occupying a total of 500×240 CVs was performed. Nusselt numbers obtained in different computation runs differed within 1% for the single-phase flow and within 2% for the gas-droplet flow with evaporating droplets. The Nusselt number being rather sensitive to variation of mean-flow quantities and to the temperature of the two-phase flow, in the majority of computations, a grid comprising 350×120 CVs was used.

Initial conditions at the pipe inlet were used in the form of uniform profiles of phase parameters. At the pipe outlet, boundary conditions consisted in setting zero derivatives of variable quantities in the longitudinal direction. At the pipe axis, for both phases, conditions of symmetry were adopted. At the wall were the wall impermeability condition and the no-slip conditions. For the dispersed phase were adopted the conditions of Derevich (2002).

After precipitation at the channel wall, droplets were assumed to stick to the surface and never return to the flow.

At the first stage, a comparison with experimental data for single-phase turbulent sudden expansion flows was performed. These results were presented in Terekhov and Pakhomov (2008). Comparison results for two-phase gas-dispersed and mist flows behind a backward-facing step and downstream of a pipe sudden expansion were published in Terekhov and Pakhomov (2009a, b).

5. NUMERICAL PREDICTIONS, ITS DISCUSSION, AND COMPARISON WITH EXPERIMENTAL RESULTS

All calculations were carried out for a monodispersed gas-droplet mixture. The tube diameter before expansion $2R_1 = 20$ mm, behind expansion it was $2R_2 = 60$ mm, the degree of channel expansion was ER $= (R_2/R_1)^2 = 9$, and the step height was $H = 20$ mm. The gas flow velocity before detachment was $U_1 = 10 - 60$ m/s, and Reynolds number for the gas phase was $\mathrm{Re}_H = HU_1/\nu = 1.3 \times 10^4 - 8 \times 10^4$. The initial velocity of the dispersed phase was $U_{L1} = 0.8U_1$. The initial droplet sized varied within $d_1 = 0 - 100$ μm, and their mass concentration changed within $M_{L1} = 0 - 0.1$. In the initial section, drops were monodisperse, and further down, the flow their size changed in both directions. Calculations were made for water and ethanol droplets. The length of calculation region after the tube expansion was $30H$. The density of heat flux fed to the tube surface was $q_W = 1$ kW/m^2.

Profiles of the axial velocity of the particles, their concentrations, and gas temperatures for two cases of the particles diameter are shown in Fig. 2. Small particles (solid curves) fall into the separation area and are present over the whole pipe section, and large drops practically do not permeate in the separation area and move only in the shear layer [see Fig. 2(a)]. Increased particle size acts to suppress the entrainment of particles with the recirculation flow because of increased Stokes number. For 100 μm diameter droplets (dashed curves), the Stokes number is Stk $= 2.5$, the entrainment of the dispersed phase with the detached flow being therefore less pronounced. The Stokes number of the dispersed phase in the mean motion Stk is one of the main criterion for determination of dispersed phase involvement into circulation of airflow. At Stk $\ll 1$, the particles are involved well into the detachment motion of the gas phase, and at Stk $\gg 1$, the dispersed phase does not participate in the recirculation motion. It is de-

termined as Stk $= \tau/\tau_f$, where τ_f is the time scale of turbulence for the flat detachment flow (Fessler and Eaton, 1999):

$$\tau_f = 5H/U_1 \tag{7}$$

It is necessary to note that relationship (6) was obtained by Fessler and Eaton (1999) for the flow behind a backward-facing step, and for the axial-symmetrical flows, its applicability requires separate investigation.

The radial profiles of the dispersed phase mass loading ratio downstream of the pipe abrupt expansion are shown in Fig. 2(b) for various initial particle diameters, $d_1 = 10$ μm, Stk $= 0.03$, and $d_1 = 100$ μm, Stk $= 2.7$. It should be noted that it entrains finely dispersed droplets into the separated flow readily, which are present in the stream throughout the whole pipe cross section, whereas large particles, due to their inertia, almost never enter the recirculation region. Behind the detachment point, the mass fraction of fine droplets decreases sharply because of intense evaporation of particles and due to the sudden expansion of the flow field. In the wall zone, owing to evaporation, the mass concentration of droplets is much lower than in the axial zone of the pipe.

The temperature profiles of the gas phase $\Theta = (T - T_W) / (T_1 - T_W)$ are shown in Fig. 2(c), where T_1 and T_W are the initial temperature of the flow in the detachment cross section and the wall temperature for two cases of water droplet initial diameter. While moving downward, the flow the profile of gas temperature substantially changes. In the axial region, gas temperature $\Theta > 1$ is explained by local gas cooling because of adiabatic evaporation of droplets. In the case of smaller droplets, the parameter Θ has larger value. Analogous results have been obtained in measurements and predictions (Terekhov and Pakhomov, 2005; Terekhov et al., 2005) in the studies of wall mist screens. Gas temperature, especially near the wall in case of the large drops, is higher (respectively, the value Θ is lower). The temperature profiles directly after flow detachment ($x/H = 2$) testify to an increase in thickness of the thermal mixing layer behind a backward-facing step. Intensive turbulent mixing in the detachment area leads to the fact that the most part of the temperature difference is within a thin wall layer (whose thickness is about 3%–5% of tube radius). Correspondingly, the value of heat transfer of the two-phase flow with the tube surface is determined by the intensity of turbulent mixing of the gaseous phase in the thin near-wall layer.

Figure 3 shows the distributions of Nusselt numbers over the pipe length for water and ethanol droplets, cor-

(a)

(b)

(c)
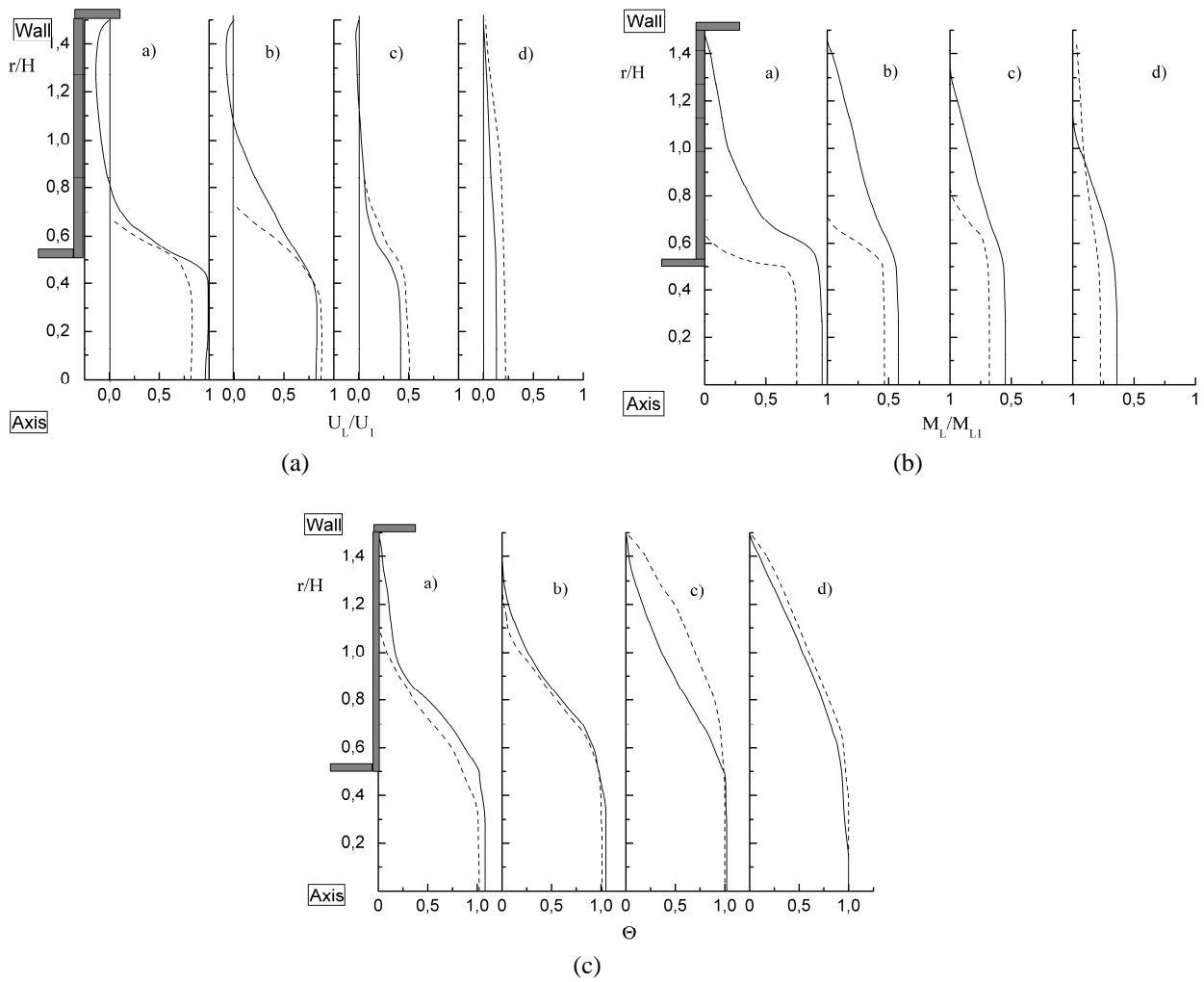
FIG. 2: (a) Distribution of water droplet axial velocity, **(b)** their mass fraction, and **(c)** gas temperature for particles of minimal initial size ($d_1 = 10$ μm, solid curves) and for maximal diameter ($d_1 = 100$ μm, dashed curves). $H = 20$ mm, Re = 13,300, $U_{L1} = 0.8\,U_1$, $T_1 = T_{L1} = 293$ K, $q_W = 1\,\text{kW/m}^2$, $M_{L1} = 0.05$; **(a)** $x/H = 2$, **(b)** $x/H = 6$, **(c)** $x/H = 10$, **(d)** $x/H = 15$

respondingly. The local Nusselt numbers were calculated by the formula

$$\text{Nu} = \frac{q_W R_2}{\lambda\,(T_W - T_m)}$$

where $T_m = 2/U_1 R_2^2 \int_0^{R_2} TU r\,dr$ is the mean gas flow temperature. Droplet addition to the airflow results in a substantial (more than twofold) heat transfer augmentation in comparison with the single-phase airflow (curve 1), all other conditions being identical. Enhanced heat transfer is observed both in the recirculation zone and in the relaxation region. The latter is confirmed by data in Fig. 2 showing that small droplets readily become entrained with the separated flow. Increasing the liquid droplet diameter exerts different effects on heat transfer in the separation flow. Fine droplets evaporate faster (over a shorter pipe length; see curve 2 in Fig. 3) due to a larger interphase surface. As more and more evaporating droplets disappear from the flow, the heat transfer intensity tends to the value observed in the single-phase flow. As a result, in the detachment zone, the rate of heat transfer is roughly the same as in the one-phase flow; behind

(a)   (b)
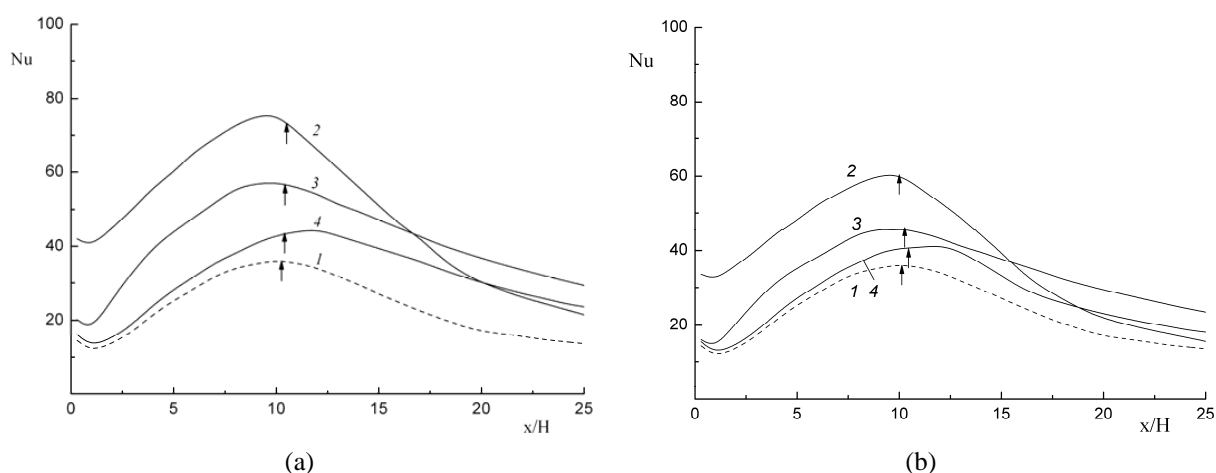
FIG. 3: Predicted local Nusselt number distribution along the pipe length **(a)** for the water and **(b)** for the ethanol droplets. The arrows mean the locus of reattachment point. $M_{L1} = 0.05$. Curve 1, $d_1 = 0$ μm (one-phase flow); curve 2, 10; curve 3, 50; curve 4, 100

the reattachment point, the heat transfer enhancement increases due to droplet evaporation. It should be noted that under conditions with evaporation, the Nusselt number in the flow laden with large droplets ($d_1 = 100$ μm) is smaller than the same number for finer droplets ($d_1 = 50$ μm) over the entire calculated flow domain.

Note that data on Nusselt number distribution fail to provide quantitative information on particles' involvement in recirculation gas motion. Data on Nusselt number

distribution provide only the qualitative evaluation of the degree of drop involvement in the detached gas flow.

Distribution of the maximal Nusselt number depending on the Reynolds number, plotted by the step height and initial velocity of the gas phase, is shown in Fig. 4. The empirical correlation (Baughn et al., 1989) (solid lines in Fig. 4) was used for comparison at the single-phase airflow. This correlation describes well the results obtained for the flow with pipe sudden expansion un-

(a)   (b)
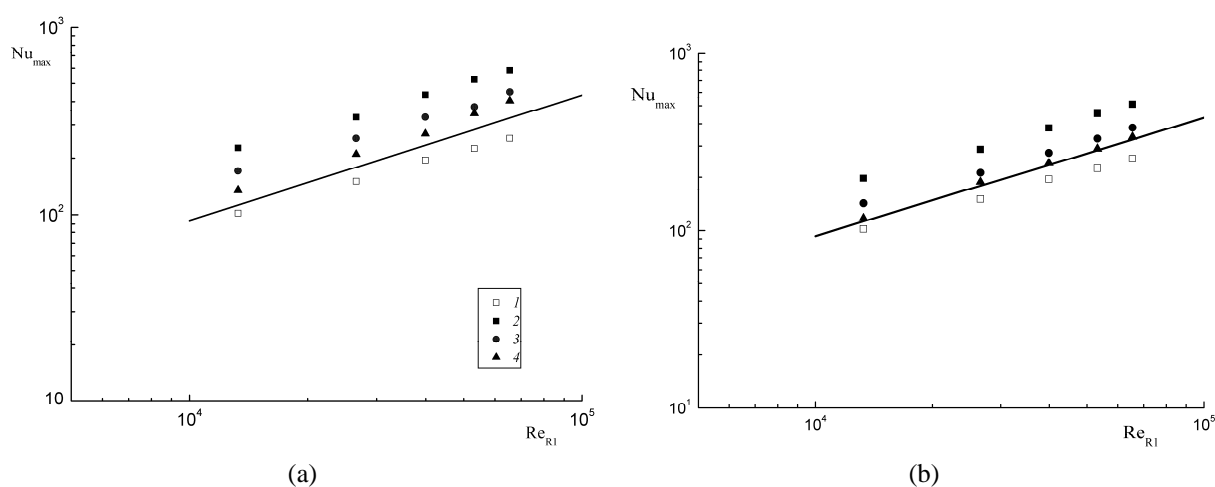
FIG. 4: Maximum Nusselt number downstream of the pipe sudden expansion for the **(a)** water and **(b)** ethanol particles as a function of Reynolds number. Solid line is the correlation from Baughn et al. (1989). The point designations and conditions of predictions are the same as in Fig. 3.

der the boundary conditions T_W = const and q_W = const:

$$\text{Nu}_{\max} = 0.2\text{Re}_{R1}^{2/3}, \qquad (8)$$

where $\text{Nu}_{\max} = \alpha_{\max} 2R_2/\lambda$ is the maximal Nusselt number, plotted by the tube diameter after the flow expansion. For the single-phase flow after the abrupt expansion, the results of calculations by this model (Fig. 4, line 1) correlate satisfactorily with correlation (7). With a rise of Re number, the local maximal Nusselt number increases, what is typical both for the single-phase flow and the gas-droplet medium. For the gas-droplet flow, the values of heat transfer coefficients are higher than the corresponding values obtained for the single-phase flow (Fig. 4, curves 2–4) because of evaporation of the dispersed phase. The increase in the number of droplets and their initial diameter influences differently heat transfer augmentation. A rise of mass concentration of droplets enhances the heat transfer rate. An increase in the particle size decreases heat transfer because of a significant reduction of the contact interface area, what is obviously in the range of low Re numbers. The employment of liquid with lesser phase transition heat (ethanol) as a coolant results in a value of heat transfer coefficient lesser than for the water droplets both in the area of flow recirculation and behind the section of flow attachment.

Distribution of heat transfer intensification parameter Nu/Nu_0, where Nu_0 is the Nusselt number for single-phase detached flow at other identical parameters, is given in Fig. 5 for the case of the used water (solid lines) and ethyl alcohol (dashed lines). For the case of small wa-

ter and ethanol particles ($d_1 = 10$ μm), heat transfer growth is observed in the whole calculation area. Large inertial droplets ($d_1 = 100$ μm), practically not dispersed in the recirculation area, cause an insignificant increase of the parameter Nu/Nu_0 in the zone of the detached flow, whereas the noticeable increase of heat transfer is specific for the area behind the attachment point, which accords with our data (Hishida et al., 1995; Terekhov and Pakhomov, 2009, 2010). Use of ethanol as a coolant results in a lesser increase of heat transfer in the detached two-phase flow compared with the water drops. All points mentioned accord with the data in Figs. 2–4.

The effect of step heights on the heat transfer rate is illustrated by Fig. 6 for two steps of 10 mm and 20 mm. Here $\text{St}_{0,\max}$ is the maximal Stanton number for the one-phase airflow, and x_R is the flow reattachment length. The Stanton number was calculated by the formula $\text{St} = \alpha/(\rho\,C_P\,U_1)$; here α is the heat transfer coefficient and U_1 is the flow velocity. An analysis of the data in Fig. 6 shows that the heat transfer in the case of gas-droplet flow increases appreciably (more than 50%) for both step heights. Predicted heat transfer for the step $H = 20$ mm (Stk = 1.1) is larger than that for $H = 10$ mm (Stk = 2.2) in the reattachment point. For the case $H = 10$ mm, the value $\text{St}/\text{St}_{0,\max}$ is higher in the area of reattached flow than in the case of the step 20 mm high. In the recirculation region, the heat transfer for $H = 20$ mm is higher than that for $H = 10$ mm because at lesser Stokes num-

FIG. 5: Heat transfer intensification ratio along the pipe length for water (solid lines) and ethanol (dashed lines) droplets. $M_{L1} = 0.05$. Curve 1, $d_1 = 10$ μm; 2, 100.
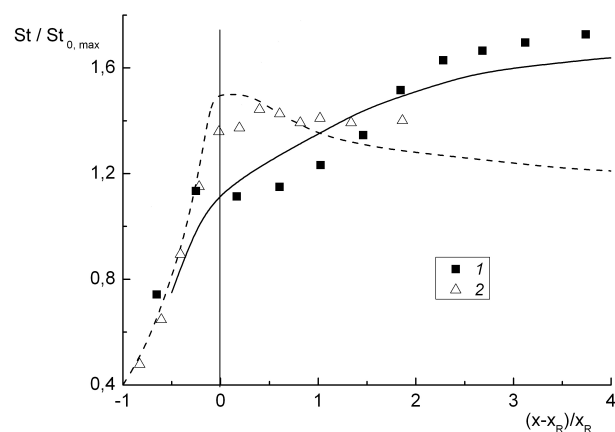

FIG. 6: Stanton number profiles in mist turbulent flow behind the backward-facing step for $H = 10$ mm (solid line) and 20 mm (dashed line). Symbols are experimental data of Hishida et al. (1995). $T_W = 323$ K. Curve 1, $H = 10$ mm, Stk = 2.2; 2, 20, Stk = 1.1.

ber, droplets are better entrained and dispersed through the recirculation flow. The maximum locus of heat transfer is far behind the reattachment point ($(x - x_R)/x_R \approx 2 - 4$) for $H = 10$ mm, which can be explained by lower entrainment of the particles into the detached flow at large Stokes numbers. Maximum heat transfer for $H = 20$ mm approximately coincides with the reattachment point.

6. CONCLUSIONS

Fine droplets (with a small Stokes number) get readily entrained with the detached flow, becoming scattered throughout the pipe cross section. On the contrary, large particles, due to their inertia, did not get into the recirculation zone, being therefore present only in the shear layer region. In the wall zone, due to droplet evaporation, the concentration of liquid droplets is much lower than in the axial region of the cylindrical channel.

Addition of droplets to the flow results in a pronounced heat transfer enhancement (twofold) in comparison with the single-phase airflow, all other conditions being identical. Here augmentation of heat transfer both in the recirculation zone and in the flow development region in the case of fine particles (Stokes number Stk < 0.3) is noteworthy. The latter observation confirms the conclusion that finely dispersed droplets get entrained with the detached flow. Relatively large particles (Stk > 1) added to the flow almost never enter the recirculation zone, the heat transfer intensity in this zone remains roughly unchanged, and enhanced heat transfer is only observed in the reattachment zone.

An increase in the initial droplet diameter decreases the Nusselt number due to interphase contact area reduction at fixed mass concentration of droplets. The results of a comparative analysis with previously experimental and numerical data for pipe sudden expansion two-phase flows and for flows past a backward-facing step are presented.

REFERENCES

Alemasov, V. E., Glebov, G. A., and Kozlov, A. P., *Methods of Thermoanemometer Study of Separation Flow* (in Russian), Kazan Branch of Academy of Sciences of USSR, Kazan, 1989.

Baughn, J. W., Hoffman, M. A., Lounder, B. E., Lee, D., and Yap, C., Heat transfer, temperature, and velocity measurements downstream of an abrupt expansion in a circular tube at uniform wall temperature, *Trans. ASME J. Heat Transfer*, vol. **111**, pp. 870–877, 1989.

Clift, R., Grace, J. R., and Weber, M. E., *Bubbles, Drops, and Particles*, Academic, New York, 1978.

Derevich, I. V., The hydrodynamics and heat transfer and mass transfer of particles under conditions of turbulent flow of gas suspension in a pipe and in an axisymmetric jet, *High Temp.*, vol. **40**, pp. 78–91, 2002.

Derevich, I. V. and Zaichik, L. I., Particle deposition from a turbulent flow, *Fluid Dyn.*, vol. **23**, pp. 722–729, 1988.

Eaton, J. K. and Johnston, J. P., Review of research on subsonic turbulent flow reattachment, *AIAA J.*, vol. **19**, pp. 1093–1100, 1981.

Fessler, J. R. and Eaton, J. K., Turbulence modification by particles in a backward-facing step flow, *J. Fluid Mech.*, vol. **314**, pp. 97–117, 1999.

Founti, M. and Klipfel, A., Experimental and computational investigations of nearly dense two-phase sudden expansion flows, *Int. J. Exp. Thermal Fluid Sci.*, vol. **17**, pp. 27–36, 1998.

Gatski, T. B. and Speziale, C. G., On explicit algebraic stress models for complex turbulent flows, *J. Fluid Mech.*, vol. **254**, pp. 59–78, 1993.

Hardalupas, Y., Taylor, A. M. K. P., and Whitelaw, J. H., Particle dispersion in a vertical round sudden-expansion flow, *Philos. Trans. R. Soc. London, Part A*, vol. **341**, pp. 411–442, 1992.

Hishida, K., Nagayasu, T., and Maeda, M., Augmentation of convective heat transfer by an effective utilization of droplet inertia, *Int. J. Heat Mass Transfer*, vol. **38**, pp. 1773–1785, 1995.

Hwang, C. B. and Lin, C. A., Improved low-Reynolds-number $k - \tilde{\varepsilon}$ model based on direct simulation data, *AIAA J.*, vol. **36**, pp. 38–43, 1998.

Leonard, B. P., A stable and accurate convective modelling procedure based on quadratic upstream interpolation, *Comput. Methods Appl. Mech. Eng.*, vol. **19**, pp. 59–79, 1979.

Lumley, J. L., ed., *The Second Order Model for Turbulent Flows*, Hemisphere, New York, 1980.

Mastanaiah, K. and Ganic, E. N., Heat transfer in two-component dispersed flow, *Trans. ASME J. Heat Transfer*, vol. **103**, pp. 300–306, 1981.

Ota, T., A survey of heat transfer in separated and reattached flows, *Appl. Mech. Rev.*, vol. **53**, pp. 219–235, 2000.

Patankar, S. V., *Numerical Heat Transfer and Fluid Flow*, Hemisphere, New York, 1980.

Ruck, B. and Makiola, B., Particle dispersion in a single-sided backward-facing step flow, *Int. J. Multiphase Flow*, vol. **14**, pp. 787–800, 1988.

Simonin, O., Prediction of the dispersed phase turbulence in particle-laden jet, in *Proc. First ASME–JSME Fluid Eng. Conf.*, pp. 197–206, ASME FED, New York-, 1991.

Simpson, R. L., Aspects of turbulent boundary-layer separation, *Prog. Aerospace Sci.*, vol. **32**, pp. 457–521, 1996.

Terekhov, V. I. and Pakhomov, M. A., The thermal efficiency of near-wall gas-droplets screens. I. Numerical modeling, *Int. J. Heat Mass Transfer*, vol. **48**, pp. 1747–1759, 2005.

Terekhov, V. I. and Pakhomov, M. A., Turbulent gas-dispersed flow in a pipe with sudden expansion: Numerical simulation, *Thermophys. Aeromech.*, vol. **15**, pp. 589–601, 2008.

Terekhov, V. I. and Pakhomov, M. A., The simulation of turbulent two-phase flow after an abrupt expansion of the pipe in the presence of evaporation of droplets, *High Temp.*, vol. **47**, pp. 384–391, 2009.

Terekhov, V. I. and Pakhomov, M. A., Predictions of turbulent flow and heat transfer in gas-droplets flow downstream of a sudden expansion, *Int. J. Heat Mass Transfer*, vol. **52**, pp. 4711–4721, 2009.

Terekhov, V. I., Pakhomov, M. A., Sharov, K. A., and Shishkin, N. E., The thermal efficiency of near-wall gas-droplets screens. II. Experimental study and comparison with numerical results, *Int. J. Heat Mass Transfer*, vol. **48**, pp. 1760–1771, 2005.

Van Doormaal, J. P. and Raithby, G. D., Enhancements of the SIMPLE method for predicting incompressible fluid flow, *Int. J. Numer. Heat Transfer A*, vol. **7**, pp. 147–164, 1984.

Vogel, J. C. and Eaton, J. K., Combined heat transfer and fluid dynamics measurements downstream of a backward-facing step, *Trans. ASME J. Heat Transfer*, vol. **107**, pp. 922–929, 1985.

Volkov, E. P., Zaichik, L. I., and Pershukov, V. A., *Numerical Modeling of Combustion of Solid Fuel* (in Russian), Nauka, Moscow, 1994.

Yua, K. F., Lau, K. S., and Chan, C. K., Numerical simulation of gas-particle flow in a single-side backward-facing step flow, *J. Comp. Appl. Math.*, vol. **163**, pp. 319–331, 2004.

Zaichik, L. I., Kozelev, M. V., and Pershukov, V. A., Prediction of turbulent gas-dispersed channel flow with recirculation zones, *Fluid Dyn.*, vol. **29**, pp. 65–75, 1994.

Zaichik, L. I., Pershukov, V. A., Kozelev, M. V., and Vinberg, A. A., Modeling of dynamics, heat transfer, and combustion in two-phase turbulent flow: 1. Isothermal flow, *Int. J. Exp. Thermal Fluid Sci.*, vol. **15**, pp. 291–310, 1997.

Zhang, H. Q., Chan, C. K., and Lau, K. S., Numerical simulation of sudden-expansion particle-laden flows using an improved stochastic separated flow model, *Int. J. Numer. Heat Transfer A*, vol. **40**, pp. 89–102, 2001.

EFFECTS OF HEAT SOURCE/SINK AND RADIATIVE HEAT TRANSFER ON HYDROMAGNETIC NATURAL CONVECTIVE FLOW THROUGH A VERTICAL CHANNEL[†]

Ajay Kumar Singh

Department of Mathematics, C. L. Jain College, Firozabad 283 203, India, E-mail: aksinghnpsingh@rediffmail.com

Effects of heat source and radiative heat transfer on unsteady hydromagnetic natural convective laminar flow of an incompressible homogeneous, electrical conducting, viscous fluid through a porous medium in a vertical channel consisting of semi-infinite parallel walls is studied. The fluid flows under the influence of uniform magnetic field applied normal to the flow. Using the Laplace transform technique, the solutions for velocity and temperature fields are obtained. Expressions for skin friction and rate of heat transfer are also derived. The effects of material parameters on temperature distribution, velocity field, skin friction, and rate of heat transfer are discussed for symmetrical cooling of the channel walls. The effects of material parameters on velocity are shown graphically, while those of skin friction and heat transfer rate are presented in tabular form and a corresponding discussion is made. The model finds applications in nuclear heat transfer processes, metallurgy, and energy systems.

KEY WORDS: *heat transfer, natural convection, convective flow, vertical channel, porous medium*

1. INTRODUCTION

Convective fluid flows through porous media are of fundamental importance due to their broad range of practical applications in science and technology. These include utilization of geothermal energy, thermal insulation in engineering, insulation of buildings, control of pollutant spread in groundwater, design of nuclear reactors, thermal energy storage system, insulation of high-temperature gas-cooled reactor vessels, heat exchangers, solar power collectors, nuclear waste repository, chemical catalytic reactors, food processing, and casting and welding of manufacturing processes. Cramer and Pai (1973) have introduced pioneer work on magnetohydrodynamic convective fluid flows through porous media. Recent monographs of

Ingham and Pop (1998), Nield and Bejan (1999), and Vafai (2000) have presented a comprehensive summary of experimental as well as theoretical research works on heat transfer and fluid flows through porous media in the presence and absence of a magnetic field.

Ostrach (1952, 1954) and Berman (1953) studied the behavior of steady free convective flow and heat transfer as well as combined free and forced convection and heat transfer in considering constant wall temperature and linearly varying wall temperature, respectively. In addition, Sparrow et al. (1959), Wooding (1963), Aung (1972), Miyatake and Fuzii (1972), and Haajizadeh and Tien (1984) have made major contributions on the convective flow of fluids in vertical channels. Singh (1988) presented an analysis on flow behavior of transient free convective flow when one of the channel walls is moving impulsively. Chandrasekhara and Narayanan (1989) have studied the laminar free convection flow under a pressure gradient through a vertical porous channel wherein

---

[†] This paper is dedicated to the memory of the late Professor E. R. G. Eckert (1904–2004), a well-known mathematician and pioneer in fluid mechanics.

NOMENCLATURE

B	Plank's constant	T	dimensional temperature
B_0	uniform magnetic field	T_w	wall temperature
C_p	specific heat at constant pressure	T_0	initial temperature
g	acceleration due to gravity	u'	component of velocity
Gr	free convection parameter	u	nondimensional component of velocity
h	distance between channel walls	u_m	mean velocity in the channel
k^*	mean absorption coefficient	y	nondimensional Cartesian coordinate
K'	permeability of the porous medium	y'	Cartesian coordinate
K	permeability parameter		
K_T	thermal conductivity of fluid	**Greek Symbols**	
M	magnetic parameter	ρ	fluid velocity
N	radiation parameter	θ	nondimensional temperature
N_R	modified radiation parameter	β	coefficient of volume expansion
Nu	rate of heat transfer		due to temperature
Pr	Prandtl number	μ	viscosity of the fluid
q'_r	radiative flux vector	σ	electrical conductivity of the fluid
S	heat source parameter	σ^*	Stefan-Boltzman constant
t'	time	τ	nondimensional skin friction
t	nondimensional time		at the plate $y = 1$

the walls of the channel are heated or cooled. The effects of rotation on free convection through a vertical channel, encountered in nature (e.g., in metrology), have been analyzed by Sacheti and Singh (1992). Jang and Chen (1992) studied forced convection in a parallel plate channel partially filled with a porous medium of high porosity and observed that the Nusselt number is sensitive to the open space ratio and also that the Nusselt number is a minimum at a certain porous layer thickness depending on the Darcy number. Hadim and Chen (1994a, 1994b) studied non-Darcy mixed convection in a vertical porous channel with discrete heat sources at the wall and with asymmetric wall heating, respectively. Singh et al. (1996) have studied analytically the transient free convective flow in a vertical channel considering asymmetric heating of the plate, while Paul et al. (1996) have studied the transient free convection flow in a vertical channel considering constant temperature and constant heat flux on the channel walls. Paul et al. (1998, 2001), Chen (2004), and Talukdar et al. (2004) have also studied convection flow between parallel vertical walls filled with a porous medium under different boundary conditions. Recently, Paul et al. (2006) have performed an analysis on the transient behavior of natural

convection flow in a porous region bounded by two vertical walls as a result of asymmetric heating and cooling of the walls.

Hydromagnetic heat transfer and fluid flow by natural convection as a result of the temperature difference between two parallel vertical walls have attracted the attention of researchers because of their many technological applications. Alpher (1961) has studied the problem of free convection between two infinite heated vertical plates embedded in a porous medium under the influence of a magnetic field. Terrill and Shreshtha (1965) have studied a problem on fully developed hydromagnetic free convection viscous fluid flow through a porous medium bounded by two vertical plates with symmetric heating of the channel walls. Thereafter many researchers, including Jha (1998), Singh et al. (2001), Singh (2005), and Singh et al. (2005), have studied hydromagnetic convective flows through parallel plate channels under different physical situations.

A general treatment of heat transfer by combined convection and radiation in boundary layer flow has been made by Arpaci (1968) to understand the nonequilibrium interaction between thermal radiation and laminar free

convection from a heated vertical plate immersed in a radiating gas. Shwartz (1968) investigated a viscous radiating nonsimilar boundary layer flow from a stagnation region and a flat plate. Cheng and Ozisic (1972) investigated the problem of simultaneous radiation and free convection from a vertical plate considering absorbing, emitting, and isotropically scattering fluid. Hossain and colleagues (Hossain and Takhar, 1996; Hossain et al., 1998, 1999) have studied the effect of radiation using Rosseland diffusion approximation [38], which leads to a nonsimilarity solution for the forced and free convection flow of an optically dense viscous incompressible fluid past a heated vertical plate with uniform free stream velocity and surface temperature. These authors used a group of transformations in their papers, and the boundary layer equations governing the flow were reduced to local nonsimilarity equations validated in both the forced and free convection regimes. Recently, Molla and Hossain (2007) have studied the effect of thermal radiation on a steady, laminar, two-dimensional mixed convection flow of viscous incompressible optically dense fluid along a vertical wavy surface.

According to the literature survey, it is noted that the free convection flow with radiation heat transfer channel walls has not been given due importance, although such flows are encountered in practical situations. This motivates the present study, which addresses the transient natural convection flow of a viscous and incompressible fluid between parallel vertical walls filled with a porous matrix under the influence of a uniform transverse magnetic field. The energy equation of the problem contains the terms due to the heat source as well as the radiation effect, and the convection phenomenon between the walls is set by changing the temperature of the walls to that of the fluid temperature. In the investigation, the mixed convection boundary layer flow of an optically dense and viscous incompressible fluid with the effect of thermal radiation is studied using Rosseland diffusion approximation (Brewster, 1972). Using Laplace transform technique, the expressions for the velocity field, temperature distribution, skin friction, and rate of heat transfer are derived and numerically discussed through graphs and tabulated for variations of the parameters encountered into the equations of momentum and energy.

2. PROBLEM FORMULATION

We consider the flow of an incompressible, electrically conducting viscous fluid through a vertical channel consisting of parallel walls embedded in a porous medium in the presence of a constant heat sink. In the Cartesian coordinate system, let the x' axis be chosen along a wall of the channel in the direction of flow and the y' axis normal to it. The channel walls are taken at a distance h apart. A uniform magnetic field of uniform strength $B_0 \left(= \mu_e H_0\right)$ is applied in the direction normal to the flow region. Initially, at $t' = 0$, the channel walls and fluid are at the same temperature T_0. When $t' > 0$, the temperature of the channel walls is instantaneously raised (or lowered) to T_w ($T_w \neq T_0$) and thereafter maintained constant. The formulation of mathematical equations is based on the following assumptions: (1) the plate is infinite in length so that the quantities involved in the governing equations are independent of x'; (2) the physical properties of the fluid are constant, except for variation in density in the buoyancy force term of the momentum equation; (3) the density is a linear function of temperature given by $\rho = \rho_0 \left[1 - \beta\left(T - T_0\right)\right]$, that is, Boussinesq approximation is taken into account (Nield and Bejan, 1999); (4) the magnetic Reynolds number is very small so that the induced magnetic field is negligible (Cramer and Pai, 1973); (5) the strength of the magnetic field is small enough to neglect Joule heating so that the term due to electrical dissipation is not included in the energy equation (Cramer and Pai, 1973); (6) the heat due to viscous dissipation is negligible; and (7) in the energy equation, radiative heat transfer is taken into account (Brewster, 1972).

Under the preceding stated assumptions, the equations governing the flow are

$$\frac{\partial u'}{\partial t'} = g\beta\left(T - T_0\right) + \vartheta\frac{\partial^2 u'}{\partial y'^2} - \frac{\sigma B_0^2}{\rho}u' - \frac{\vartheta}{K'}u' \quad (1)$$

$$\frac{\partial T}{\partial t'} = \frac{K_T}{\rho C_p}\frac{\partial^2 T}{\partial y'^2} - \frac{1}{\rho C_p}\frac{\partial q'_r}{\partial y'} - \frac{S'}{\rho C_p}\left(T - T_0\right) \quad (2)$$

For the radiative heat flux in Eq. (2), we invoke the differential approximation used by Elbarbary and Elgazeri (2004):

$$\nabla \cdot q'_r = 4\left(T - T_w\right)\int_0^\infty \alpha^2\left(\frac{\partial B}{\partial t}\right)d\lambda \quad (3)$$

For an optically thick fluid, in addition to emission, there is also self-absorption (Azzam, 2002), and the absorption coefficient depends on wavelength (Bestman, 1985). Hence the Rosseland approximation of Eq. (3) for the radiative heat flux (Datti et al., 2004) is simplified as

$$q'_r = -\frac{4\sigma^*}{3k^*}\frac{\partial T^4}{\partial y'} \quad (4)$$

We assume that the temperature differences within the flow are small so that the term T^4 may be expressed as a linear function of temperature. Hence, expending T^4 in a Taylor's series about T_0 and neglecting higher-order terms, we get

$$T^4 \cong 4T_0^3 T - 3T_0^4 \qquad (5)$$

The initial and boundary conditions are as follows:

$$
\begin{aligned}
&t' \le 0, \ u' = 0, \ T = T_0 \ \text{for all } 0 \le y' \le h \\
&t' > 0, \ u' = 0, \ T = T_w \ \text{at } y' = h \\
&u'_y = 0, \ T_y = 0 \ \text{at } y' = 0
\end{aligned}
\qquad (6)
$$

We introduce the following nondimensional quantities and parameters:

$$
y = \frac{y'}{h}, \quad t = \frac{t'\vartheta}{h^2}, \quad u = \frac{u'}{u_m}, \quad \theta = \frac{T - T_0}{T_w - T_0},
$$

$$
M_1 = M + \frac{1}{K}, \quad Gr = \frac{g\beta(T_w - T_0)h^2}{\vartheta u_m}, \quad Pr = \frac{\mu C_p}{K_T},
$$

$$
S = \frac{S'h^2}{\mu C_p}, \quad M = \frac{B_0^2 h^2 \sigma}{\mu}, \quad K = \frac{K'}{h^2},
$$

$$
N_R = \frac{N+4}{3N P_r}, \quad N = \frac{K_T k^*}{4\sigma^* T_0^3}.
$$

In view of Eqs. (4) and (5) and the previously stated nondimensional quantities and parameters, the Eqs. (1) and (2) transform to the following:

$$
\frac{\partial u}{\partial t} = Gr\theta + \frac{\partial^2 u}{\partial y^2} - M_1 u \qquad (7)
$$

$$
\frac{\partial \theta}{\partial t} = N_R \frac{\partial^2 \theta}{\partial y^2} - S\theta \qquad (8)
$$

The initial and boundary conditions (6) in nondimensional form are as follows:

$$
\begin{aligned}
&t \le 0, \quad u(y,t) = 0, \quad \theta(y,t) = 0, \\
&t > 0, \quad u(1,\ t) = 0, \quad \theta(1,\ t) = 1, \\
&u_y(0,\ t) = 0, \quad \theta_y(0,\ t) = 0
\end{aligned}
\qquad (9)
$$

3. SOLUTION OF THE PROBLEM

Using Laplace transform technique, the solutions of Eqs. (8) and (7), satisfying the conditions (9), are as follows:

$$
\begin{aligned}
\theta(y,t) = (-1)^n \sum_{n=0}^{\infty} \Big[& H_1(X_n, N_R, S, t) \\
& + H_2(Y_n, N_R, S, t) \Big]
\end{aligned}
\qquad (10)
$$

$$
\begin{aligned}
u(y,t) = (-1)^n \sum_{n=0}^{\infty} \frac{Gr}{M_2} \left(1 - e^{M_3 t}\right) \\
\times \left[H_1(X_n, N_R, S, t) + H_2(Y_n, N_R, S, t) \right] \\
- (-1)^n \sum_{n=0}^{\infty} \frac{Gr}{M_2} \left(1 - e^{M_3 t}\right) \Big[H_3(X_n, 1, M_1, t) \\
+ H_4(Y_n, 1, M_1, t) \Big]
\end{aligned}
\qquad (11)
$$

where

$$
M_2 = M_1 - N_R S, \quad M_3 = \frac{M_2}{N_R - 1},
$$

$$
M_4 = M_1 + M_3, \quad M_5 = S + M_3,
$$

$$
X_n = 2n + 1 - y, \quad Y_n = 2n + 1 + y,
$$

$$
\begin{aligned}
F(Z_1, Z_2, Z_3, Z_4) = \frac{1}{2} \Bigg[& \exp\left(-Z_1\sqrt{Z_2 Z_3}\right) \\
& erfc\left(\frac{Z_1\sqrt{Z_2}}{2\sqrt{Z_4}} - \sqrt{Z_3 Z_4}\right) + \exp\left(Z_1\sqrt{Z_2 Z_3}\right) \\
& erfc\left(\frac{Z_1\sqrt{Z_2}}{2\sqrt{Z_4}} + \sqrt{Z_3 Z_4}\right) \Bigg]
\end{aligned}
$$

4. SKIN FRICTION AND RATE OF HEAT TRANSFER

The skin friction (τ) at the plate $y = 1$ is

$$
\begin{aligned}
\tau = \left(\frac{\partial u}{\partial y}\right)_{y=1} = \sum_{n=0}^{\infty} (-1)^{n+1} \frac{Gr}{M_2} \\
\times \left[G_1(D_n, C_n, N_R, S, t) - G_2(D_n, C_n, 1, M, t) \right] \\
+ \sum_{n=0}^{\infty} (-1)^{n+1} \frac{G_r}{M_2} e^{M_3 t} \Big[G_3(D_n, C_n, N_R, M_5, t) \\
- G_4(D_n, C_n, 1, M_4, t) \Big]
\end{aligned}
\qquad (12)
$$

The rate of heat transfer (Nu) at the wall $y = 1$ is

$$
\begin{aligned}
Nu = \left(\frac{\partial \theta}{\partial y}\right)_{y=1} = \sum_{n=0}^{\infty} (-1)^{n+1} \\
\times J_1(C_n, D_n, N_R, M_5, t)
\end{aligned}
\qquad (13)
$$

where

$$
\begin{aligned}
f(X_1, X_2, X_3, X_4, X_5) = F_1(X_1, X_3, X_4, X_5) \\
- F_2(X_2, X_3, X_4, X_5),
\end{aligned}
$$

$$C_n = 2n + 2, \quad D_n = 2n, \quad X_n = 2n + 1 - y,$$

$$M_2 = M_1 - \mathrm{N_R}S, \quad M_3 = \frac{M_2}{\mathrm{N_R} - 1},$$

$$M_4 = M_1 + M_2, \quad M_5 = S + M_3$$

$$F(Z_1, Z_2, Z_3, Z_4) = \frac{1}{2}\sqrt{Z_2 Z_3}\left[\exp\left(-Z_1\sqrt{Z_2 Z_3}\right)\right.$$

$$erfc\left(\frac{Z_1\sqrt{Z_2}}{2\sqrt{Z_4}} - \sqrt{Z_3 Z_4}\right) + \exp\left(Z_1\sqrt{Z_2 Z_3}\right)$$

$$\left.erfc\left(\frac{Z_1\sqrt{Z_2}}{2\sqrt{Z_4}} + \sqrt{Z_3 Z_4}\right)\right] + \sqrt{\frac{Z_2}{\pi t}}$$

$$\exp\left(-\frac{Z_1^2 Z_2^2}{4Z_4} - Z_3 Z_4\right)$$

5. RESULTS AND DISCUSSION

In this study, we have examined the unsteady natural convective flow through a vertical channel embedded in a porous medium in the presence of a constant heat source and radiative heat transfer under the influence of a uniform magnetic field. The system of governing Eqs. (7) and (8) with the boundary conditions (9) is solved employing the Laplace transform technique. The temperature is coupled to the velocity by the free convection parameter Gr in Eq. (7). To illustrate the characteristics of velocity field, distribution of temperature, skin friction, and heat transfer rate (Nusselt number) of the flow field, the results are numerically studied and are presented graphically and in tabular form. These calculations show the variations in the velocity field, temperature distribution, skin friction, and heat transfer rate, influenced by the material parameters of the flow problem, namely, the magnetic parameter (M), the permeability parameter (K), the heat source parameter (S), the free convection parameter (Gr), the Prandtl number (Pr), the radiation parameter (N), and the time (t). An important case of general interest viz. cooling of the channel walls by free convection currents (Gr > 0) is considered, which is employed for practical applications in nuclear technology and also in geophysical and naval energy system applications. To be realistic, the values of Prandtl number are chosen to be 0.025, 0.71, 1.0, and 7.0, which correspond to mercury, air, electrolyte solution, and water at $20°\mathrm{C}$ and 1 atmospheric pressure, respectively—the fluids generally used in energy and naval/aerospace technologies (Kim, 2000; Rosa, 1968; Blums, 1987; Ferraro and Plumpton, 1966). The observations associated with variations in velocity field and temperature distributions are shown with the aid of a number of graphical figures, while that of skin friction and rate of heat transfer is recorded in tabular form.

Figure 1 shows variations in velocity field versus y due to a change in the magnitude of the magnetic parameter (M) for fixed values of the remaining parameter. the maximum magnitude of velocity is recorded for a minimum value of M, indicating that a rise in the magnitude of M leads to a decrease in the velocity consistent with many other studies (Kim, 2000; Rosa, 1968; Blums, 1987; Ferraro and Plumpton, 1966). Therefore the hydromagnetic drag embodied in the term $-Mu$ of the momentum Eq. (7) retards the velocity in the cooling case of the channel walls by free convection currents (Gr > 0), wherein the temperature is coupled to the velocity via the free convection parameter (Gr). This is an important controlling mechanism in nuclear energy systems heat transfer, where momentum development can be reduced by enhancing the magnetic field.

Figure 2 represents the variations in velocity versus y, influenced by the change in the permeability parameter (K) for fixed values of the other parameters. It is observed that the velocity is elevated with the rise in the magnitude of the permeability parameter for Gr > 0. In fact, an increase in permeability parameter declines the bulk porous resistance, which increases the momentum development
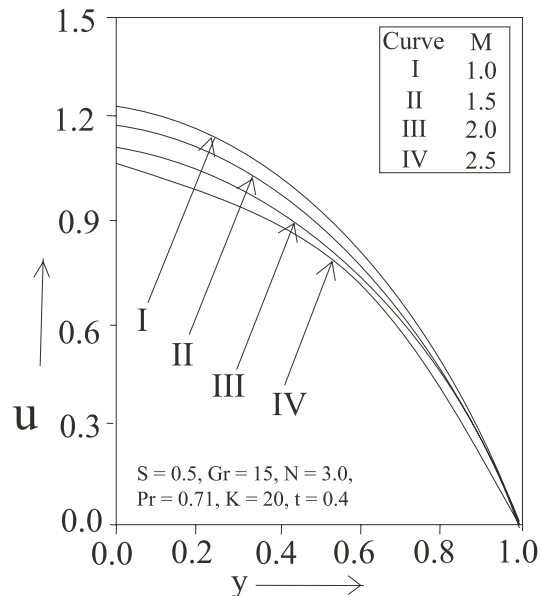
FIG. 1: Effect of magnetic parameter on velocity field when Pr = 0.71, Gr = 15, $S = 0.5$, $N = 3.0$, $K = 20$, and $t = 0.4$
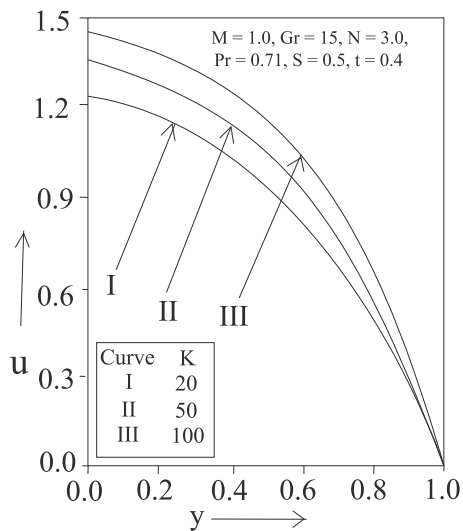
FIG. 2: Effect of parameter on velocity field when Pr = 0.71, Gr = 15, $N = 3.0$, $S = 0.5$, $M = 1.0$, and $t = 0.4$

locity for cooling of the channel walls (Gr > 0) as there would be a thinning of the thermal boundary layer as a result of reduced thermal conductivity, which in turn retards the velocity field.

Figure 4 illustrates the variations in the velocity profiles versus y due to a change in the free convection parameter (Gr) for fixed values of the other parameters. One can observe that the velocity is significantly enhanced with the increase in the magnitude of the free convection parameter. Increase in (Gr) physically implies heat removed from the channel walls, which results in thickening of the thermal boundary layer, which leads to an elevation in the transient velocity.

Figure 5 shows the variations in the transient velocity versus y due to a change in the Prandtl number (Pr), when other parameters have fixed numerical values. It is noted that the velocity decreases with an enhanced value of Prandtl number for externally cooled walls. The maximum magnitude of velocity is recorded for a minimum value of Prandtl number, that is, for mercury, and the minimum magnitude of velocity corresponds to water since the Prandtl number is mathematically defined as the ratio of the momentum diffusivity to the thermal diffusivity. Higher-Pr fluids transfer heat less effectively than do lower-Pr fluids, and consequently, a decrease in temperature takes place, which in turn reduces the velocity in the flow regime.

of the flow regime, thereby enhancing the transient velocity.

Figure 3 depicts the variations in the transient velocity versus y due to a change in the heat sink parameter (S) when other parameters have fixed values. It is recorded that an enhanced heat sink parameter decreases the ve-

FIG. 3: Effect of heat source/sink parameter on velocity field when Pr = 0.71, Gr = 15, $M = 1.0$, $N = 3.0$, $K = 20$, and $t = 0.4$
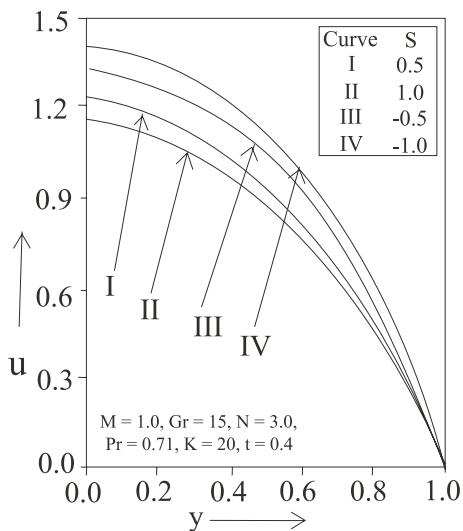

FIG. 4: Effect of free convection parameter on velocity field when $M = 1.0$, Pr = 0.71, $N = 1.0$, $S = 0.5$, $K = 20$, and $t = 0.4$
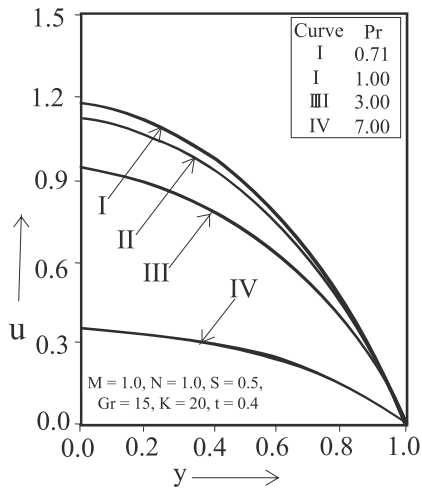
FIG. 5: Effect of Prandtl number on velocity field when $M = 1.0$, $N = 1.0$, $S = 0.5$, Gr $= 15$, $K = 20$, and $t = 0.4$

Figure 6 represents the variations in the transient velocity profiles versus y due to a change in the radiation parameter (N) for fixed values of the other parameters. It is recorded that the effect of enhanced radiation parameter is to decrease the velocity for cooling of the channel walls by free convection currents (Gr > 0). Increased radiation implies more extraction of heat, resulting in a thickened thermal boundary layer, which in turn decreases the velocity.

Figure 7 shows the variations in the velocity versus y due to a change in the time parameter (t) when other parameters are fixed. It is noted that the velocity increases as time increases and the flow attains steady state conditions for large times.

Figure 8 illustrates the variations in temperature versus y due to a change in heat sink parameter (S) for fixed values of the other parameters. It is observed that the temperature field decreases throughout the flow field with an increase in the heat sink parameter. In fact, the presence of a heat sink parameter reduces the velocity field due to thickening of the thermal boundary layer.

Figure 9 depicts the variations in the temperature versus y due to a change in the Prandtl number (Pr) for the fixed values of the other parameters. We note that the effect of enhanced value of the Prandtl number is to decrease the temperature in the entire flow regime as there would be a denseness of the thermal boundary layer due to reduced thermal conductivity.

Figure 10 illustrates the variations in the temperature distribution versus y due to a change in the radiation parameter (N) when the other parameters are treated as content. From the graph it is observed that the effect of the increased radiation parameter is to decrease the temperature in the flow field. An increase in the radiation parameter implies the release of more heat energy from the flow region by means of radiation, which leads to a decrease in the temperature.

Figure 11 shows the variations in the temperature field versus y due to a change in the time parameter (t) for

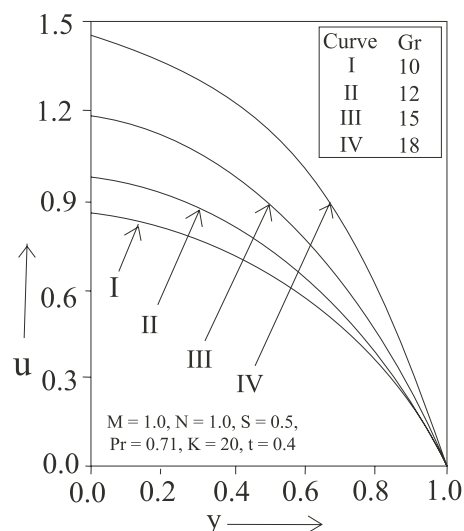**FIG. 6:** Effect of radiation parameter on velocity field when $M = 1.0$, Pr $= 0.71$, Gr $= 15$, $K = 20$, and $t = 0.4$
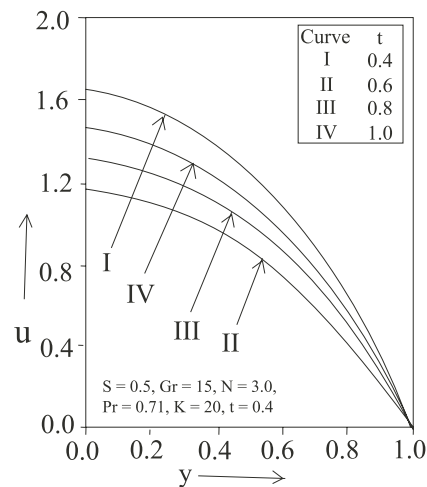
FIG. 7: Effect of time parameter on velocity field when Pr $= 0.71$, Gr $= 15$, $S = 0.5$, $N = 3.0$, $K = 20$, and $M = 1.0$
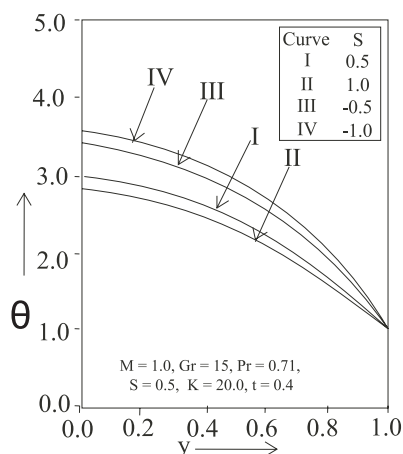
FIG. 8: Effect of heat source/sink parameter on temperature distribution when Gr = 15, $N = 3.0$, Pr = 0.71, $K = 20$, $M = 1.0$, and $t = 0.4$
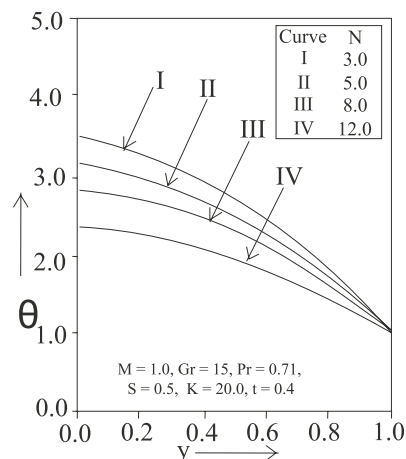
FIG. 10: Effect of radiation parameter on temperature distribution when Gr = 15, $S = 0.5$, Pr = 0.71, $K = 20$, $M = 1.0$, and $t = 0.4$
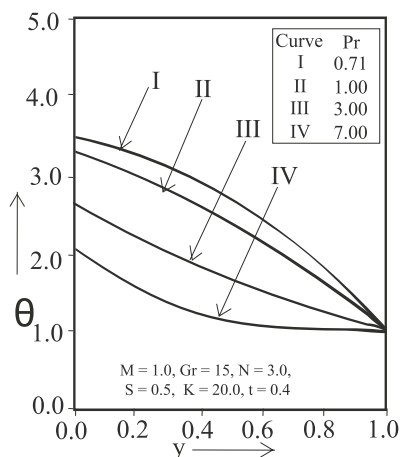
FIG. 9: Effect of Prandtl number on temperature distribution when Gr = 15, $S = 0.5$, $N = 3.0$, $K = 20$, $M = 1.0$, and $t = 0.4$
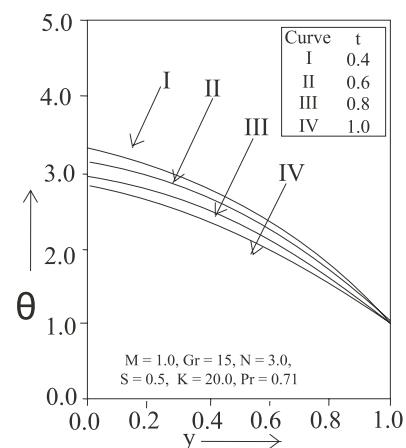
FIG. 11: Effect of time parameter on temperature distribution when Gr = 15, $N = 3.0$, $K = 20$, $M = 1.0$, and Pr = 0.71

TABLE 1: Variations in skin friction (τ) and rate of heat transfer (Nu) ($K = 20.0$ and $t = 0.1$)

M	S	Gr	N	Pr	τ	Nu
1.0	1.0	15.0	1.0	0.71	1.73275	2.16874
1.5	1.0	15.0	1.0	0.71	1.27154	–
1.0	2.0	15.0	1.0	0.71	1.92763	1.75437
1.0	1.0	20.0	1.0	0.71	2.06476	–
1.0	1.0	15.0	3.0	0.71	3.45873	1.98458
1.0	1.0	20.0	1.0	7.00	0.95824	7.36843

fixed values of the other parameters. We observe that the effect of the time parameter is to decrease the temperature. This is quite consistent with the fact that as time increases, the thermal boundary layer decreases, which in turn decreases the temperature in the flow region.

Table 1 represents the effects of M, S, Gr, N, and Pr on skin friction (τ) and heat transfer rate (Nu). The table is self-explanatory, and any discussion about the effects of the parameters on τ and Nu seems to be redundant.

6. CONCLUSIONS

In this article, we have sought to determine how the presence of a magnetic field, heat source, and radiation parameter affects the unsteady natural convection boundary layer flow through a vertical channel embedded in a porous medium for cooling of the channel walls by free convection currents (Gr $>$ 0). The conclusions of the study are as follows: (1) an increase in M, S, Pr, or N decreases the velocity field; (2) an increase in K or Gr increases the velocity field; (3) the flow velocity approaches steady state conditions as the time parameter t is increased nearly 15; (4) an increase in S, Pr, N, or t decreases the temperature in the boundary layer flow region; and (5) the general results of the study are in excellent agreement with the results of earlier studies.

REFERENCES

Alpher, R. A., Heat transfer in magnetohydrodynamic flow between parallel plates, *Int. J. Heat Mass Transfer*, vol. **13**, pp. 108–112, 1961.

Arpaci, V. S., Effect of thermal radiation on the laminar free convection from a heated vertical plate, *Int. J. Heat Mass Transfer*, vol. **11**, pp. 871–881, 1968.

Aung, W., Fully developed laminar free convection between vertical plates heated asymmetrically, *Int. J. Heat Mass Transfer*, vol. **15**, pp. 1577–1580, 1972.

Azzam, G. E. A., Radiation effects on the MHD free mixed convective flow past a semi-infinite moving vertical plate for high temperature difference, *Phys. Scripta*, vol. **66**, pp. 71–76, 2002.

Berman, A. S., Laminar flow in channels with porous walls, *J. Appl. Phys.*, vol. **24**, pp. 1232–1237, 1953.

Bestman, A. R., Free convection heat transfer to steady radiating non-Newtonian MHD flow past a vertical porous plate, *Int. J. Numer. Methods Eng.*, vol. **21**, pp. 899–908, 1985.

Blums, E., *Heat and Mass Transfer in MHD Flows*, World Scientific, Singapore, 1987.

Chandrasekhara, B. C. and Narayanan, R., Laminar convection in uniform heated vertical porous channel, *Ind. J. Technol.*, vol. **27**, pp. 371–376, 1989.

Chen, Y. C., Non-Darcy flow stability of mixed convection in a vertical channel filled with a porous medium, *Int. J. Heat Mass Transfer*, vol. **47**, pp. 1257–1266, 2004.

Cheng, E. H. and Ozisic, M. N., Radiation with free convection in an absorbing, emitting and scattering medium, *Int. J. Heat Mass Transfer*, vol. **15**, pp. 1243–1252, 1972.

Cramer, K. R. and Pai, S. I., *Magnetofluid Dynamics for Engineers and Applied Physicists*, McGraw-Hill, New York, 1973.

Datti, P. S., Prasad, K. V., Abel, M. S., and Joshi, A., MHD viscoelastic fluid flow over a non-isothermal stretching sheet, *Int. J. Eng. Sci.*, vol. **42**, pp. 935–946, 2004.

Elbarbary, E. M. E. and Elgazeri, N. S., Chebyshev finite difference method for the effect of variable viscosity on micropolar fluid flow with radiation, *Int. Commun. Heat Mass Transfer*, vol. **31**, pp. 409–419, 2004.

Ferraro, V. C. A. and Plumpton, C., *An Introduction to Magneto-Fluid Mechanics*, Clarendon, London, 1966.

Haajizadeh, M. and Tien, C. L., Combined natural and forced convection in a horizontal porous channel, *Int. J. Heat Mass Transfer*, vol. **27**, pp. 799–813, 1984.

Hadim, H. A. and Chen, G., Non-Darcy mixed-convection in a vertical porous channel with discrete heat sources at the walls, *Int. Commun. Heat Mass Transfer*, vol. **21**, pp. 377–387, 1994.

Hadim, H. A. and Chen, G., Non-Darcy mixed-convection in a vertical porous channel with asymmetric wall heating, *AIAA J. Thermophys. Heat Transfer*, vol. **8**, pp. 805–808, 1994.

Hossain, M. A. and Takhar, H. S., Radiation effect on mixed convection along a vertical plate with uniform surface temperature, *Heat Mass Transfer*, vol. **31**, pp. 243–248, 1996.

Hossain, M. A., Rees, D. A. S., and Pop, I., Free convection-radiation interaction from an isothermal plate inclined at a small angle to the horizontal, *Acta. Mech.*, vol. **127**, pp. 63–73, 1998.

Hossain, M. A., Alim, M. A., and Rees, D. A. S., The effect of radiation on free convection from a porous vertical plate, *Int. J. Heat Mass Transfer*, vol. **42**, pp. 181–191, 1999.

Ingham, D. B. and Pop, I., *Transport Phenomena in Porous Media*, Elsevier, Oxford, 1998.

Jang, J. Y. and Chen, J. L., Forced convection in a parallel plate channel partially filled with a high porosity medium, *Int. Commun. Heat Mass Transfer*, vol. **19**, pp. 263–273, 1992.

Jha, B. K., Effects of applied magnetic field on transient free convection flow in a vertical channel, *Ind. J. Pure Appl. Math.*, vol. **29**, pp. 441–445, 1998.

Kim, Y. J., Unsteady MHD convective heat transfer past a semi-

infinite vertical porous moving plate with variable suction, *Int. J. Eng. Sci.*, vol. **38**, pp. 833–845, 2000.

Miyatake, O. and Fuzii, T., Free convection heat transfer between vertical parallel plates—One plate isothermally heated and the other thermally insulated, *Heat Transfer Jpn. Res.*, vol. **3**, pp. 30–38, 1972.

Molla, M. M. and Hossain, M. A., Radiation effect on mixed convection laminar flow along a vertical wavy surface, *Int. J. Thermal Sci.*, vol. **46**, pp. 926–935, 2007.

Nield, D. A. and Bejan, A., *Convection in Porous Media*, Springer, New York, 1999.

Ostrach, S., Laminar natural convection flow and heat transfer of fluids with and without heat sources in channels with constant wall temperature, *NASA Tech. Note*, pp. 2863–2869, 1952.

Ostrach, S., Combined natural and forced convection laminar flow and heat transfer of fluids with and without heat sources in channels with linearly varying wall temperature, *NASA Tech. Note*, pp. 3141–3148, 1954.

Paul, T., Jha, B. K., and Singh, A. K., Transient free convection flow in a vertical channel with constant heat flux on walls, *Heat Mass Transfer*, vol. **32**, pp. 61–63, 1996.

Paul, T., Jha, B. K., and Singh, A. K., Free convection between vertical walls partially filled with porous medium, *Heat Mass Transfer*, vol. **33**, pp. 515–519, 1998.

Paul, T., Singh, A. K., and Mishra, A. K., Transient natural convection between two vertical walls filled with a porous material having variable porosity, *Math. Eng. Ind.*, vol. **8**, pp. 177–185, 2001.

Paul, T., Singh, A. K., and Mishra, A. K., Transient free convection flow in a porous region bounded by two vertical walls heated/cooled asymmetrically, *J. Energy Heat Mass Transfer*, vol. **28**, pp. 193–207, 2006.

Rosa, R. J., *Magnetohydrodynamic Energy Conversion*, McGraw-Hill, New York, 1968.

Rosseland, S., *Theoretical Astrophysics*, Oxford University Press, London, 1936.

Sacheti, N. C. and Singh, A. K., Free convection through a vertical channel in a rotating porous medium, *Int. Commun. Heat Mass Transfer*, vol. **19**, pp. 423–433, 1992.

Shwartz, J., Radiation coupled viscous flows, *Int. J. Heat Mass Transfer*, vol. **11**, pp. 689–697, 1968.

Singh, A. K., Natural convection in unsteady Couette motion, *Def. Sci. J.*, vol. **34**, pp. 35–41, 1988.

Singh, A. K., Gholami, H. R., and Soundalgekar, V. M., Transient free convection flow between two parallel vertical plates, *Heat Mass Transfer*, vol. **31**, pp. 329–332, 1996.

Singh, N. P., Singh, A. K., Yadav, M. K., and Singh, A. K., Unsteady free convective MHD flow of a viscous fluid in a vertical channel, *Ultra Sci.*, vol. **13**, pp. 378–381, 2001.

Singh, A. K., Effects of thermal diffusion on MHD free convection flow through a vertical channel, *J. Energy Heat Mass Transfer*, vol. **27**, pp. 109–123, 2005.

Singh, N. P., Singh, A. K., Yadav, M. K., and Singh, A. K., MHD free convection transient flow through a porous medium in a vertical channel, *Ind. J. Theor. Phys.*, vol. **53**, pp. 137–144, 2005.

Sparrow, E. M., Eichhorn, R., and Gregg, J. L., Combined forced and free convection in a boundary layer flow, *Phys. Fluids*, vol. **2**, pp. 319–328, 1959.

Talukdar, P., Mishra, S. C., Trimis, D., and Durst, F., Combined radiation and convection heat transfer in a porous channel bounded by isothermal parallel plates, *Int. J. Heat Mass Transfer*, vol. **47**, pp. 1001–1013, 2004.

Terrill, R. M. and Shreshtha, G. M., Laminar flow in a uniformly porous channel with an applied transverse magnetic field, *Appl. Sci. Res.*, vol. **12**, pp. 203–211, 1965.

Vafai, K., *Hand Book of Porous Media*, Marcel Dekker, New York, 2000.

Wooding, R. A., Convection in a saturated porous medium at large Rayleigh number or Peclet number, *J. Fluid Mech.*, vol. **15**, pp. 527–544, 1963.

HIGH ACCURACY NUMERICAL APPROACH FOR NON-SIMILAR MIXED CONVECTION BOUNDARY LAYER FLOW OVER A HORIZONTAL PLATE

K. Venkatasubbaiah

Assistant Professor, Department of Mechanical Engineering, Indian Institute of Technology Hyderabad, Hyderabad, 502205, India, E-mail: kvenkat@iith.ac.in

The mixed convection boundary layer flow over a heated horizontal plate is studied using high accuracy numerical method. Present analysis is valid when the buoyancy force effects are small compared to forced convection effects. The mixed convection boundary layer equations are given with the buoyancy term represented by Boussinesq approximation. The non-similar mixed convection boundary layer equations are solved directly using direct integration method without any approximation for non-similar terms. Numerical results are reported for assisting and opposing mixed convection flows for air. Reported results show that both the local Nusselt number and local friction factor values are increasing with increase in buoyancy parameter for assisting mixed convection flows and decreases with increasing buoyancy parameter for opposing mixed convection flows. Reported results reveal that both the local Nusselt number and the local friction factor values are high compared to local similarity and local non-similarity methods for assisting mixed convection flows and less compared to local similarity and local non-similarity methods for opposing mixed convection flows. Reported results show that velocity and temperature profiles in the boundary layer are exactly matches compared to local similarity method for low value of buoyancy parameter (ξ). For assisting mixed convection flows, the significant buoyancy effects are encountered for ξ ≥ 0.05 and the velocity exhibit an overshoot beyond the free stream velocity for high values of ξ. For opposing mixed convection flows, the effect of buoyancy is to reduce the velocity compared to pure forced convection. The thickness of thermal boundary layer decreases with increasing buoyancy parameter for assisting mixed convection flows and increases with increasing buoyancy parameter for opposing mixed convection flows. Present study provides an accurate numerical approach to solve non-similar mixed convection boundary flows.

KEY WORDS: *mixed convection flow, assisting flow, opposing flow, buoyancy parameter, non-similar solution*

1. INTRODUCTION

Mixed convection flows, resulting from simultaneous buoyancy and forced convection effects, arises in environmental and electronics cooling processes. In studying forced convective heat transfer flow over a horizontal surface, it is customary to neglect the effect of buoyancy forces. Such approach may not be justified because the buoyancy force arises when the velocity is small and the temperature difference between the surface and ambient is large. The buoyancy force induces a longitudinal pressure gradient which in turn alter the flow field and heat transfer rate from the surface. Thus the study of mixed convection flow is of practical interest.

In the literature, Mori (1961) and Sparrow and Minkowycz (1962) were first studied the buoyancy effects on mixed convection boundary layer flow over a horizontal plate using perturbation theory. Chen et al. (1977) have studied the mixed convection boundary layer flow over a horizontal plate using local similarity and local non similarity methods. However, one should note the critique of various local similarity and local non-similarity methods discussed in Brewster and Gebhart (1991). The local non-similarity method is an approximate method to

obtain the solution of non-similar boundary layer equations. In this method the equations are first subjected to a coordinate transformation, and non-similar terms in the equations are defined as new variables. The transformed boundary layer equations are then differentiated to provide differential equations for these new variables. Such a procedure of defining new variables and differentiating the transformed boundary layer equations may continue indefinitely. However, at some level non-similar terms are omitted from the formulation, which is to close the system of equations. This measure makes the accuracy of local non-similarity method difficult to assess. Schneider (1979) has obtained exact similarity solution for mixed convection boundary layer flow over a horizontal plate with the assumption of wall temperature to vary as the inverse square root of the distance from the leading edge of the plate. Hussain and Afzal (1988) were studied the mixed convection boundary layer flow on a horizontal plate using perturbation theory. A comprehensive review of mixed convection flows were given in Gebhart *et al.* (1988). Accurate numerical results does not exist in the literature without approximation for non-similar terms. This has been motivated the present investigation.

Here, non-similar mixed convection boundary layer equations are solved using direct integration method without any approximation for non-similar terms. Reported results show that velocity and temperature profiles are exactly matching compared to local similarity method for low value of buoyancy parameter. However, the velocity and temperature profiles are differ from local similarity method for high value of buoyancy parameter.

2. THE GOVERNING EQUATIONS

Consider the laminar two-dimensional motion of fluid past a semi-infinite horizontal plate, with the free stream velocity and temperature denoted by, U_∞ and T_∞. Consider the flow over isothermal horizontal plate, for which the surface temperature (T_w) is greater than the free stream temperature (T_∞). The leading edge of the plate is considered as the stagnation point. All fluid properties are assumed to be constant, except that the density variations within the fluid are considered only to the extent that they contribute to the buoyancy forces. Governing equations are obtained by invoking boundary layer approximation to the conservation equations. The steady boundary layer equations along with the Boussinesq approximation to represent the buoyancy effect, for the velocity and temperature fields are as given in Gebhart *et al.* (1988) by,

$$\frac{\partial u}{\partial x} + \frac{\partial v}{\partial y} = 0 \qquad (1)$$

$$u\frac{\partial u}{\partial x} + v\frac{\partial u}{\partial y} = -\frac{1}{\rho}\frac{\partial p}{\partial x} + \nu\frac{\partial^2 u}{\partial y^2} \qquad (2)$$

$$0 = \pm g\beta_t(T - T_\infty) - \frac{1}{\rho}\frac{\partial p}{\partial y} \qquad (3)$$

$$u\frac{\partial T}{\partial x} + v\frac{\partial T}{\partial y} = \alpha\frac{\partial^2 T}{\partial y^2} \qquad (4)$$

where u and v are the velocity components in the x and y directions; g is the gravitational force per unit mass; T is the fluid temperature; α and ν are the thermal diffusivity and kinematic viscosity respectively; β_t represents the volumetric thermal expansion coefficient. Positive and negative signs on the buoyancy term in Eq. (3) refer to assisting (flow above the plate) and opposing (flow below the plate) mixed convection flows.

The stream-wise pressure gradient induced by the buoyancy force which can be related to the temperature difference through Eq. (3) as

$$-\frac{1}{\rho}\frac{\partial p}{\partial x} = \pm g\beta_t\frac{\partial}{\partial x}\int\limits_{y}^{\infty}(T - T_\infty)dy \qquad (5)$$

Substitution of Eq. (5) into Eq. (2), one gets the momentum equation as,

$$u\frac{\partial u}{\partial x} + v\frac{\partial u}{\partial y} = \pm g\beta_t\frac{\partial}{\partial x}\int\limits_{y}^{\infty}(T - T_\infty)dy + \nu\frac{\partial^2 u}{\partial y^2} \qquad (6)$$

The boundary layer Eqs. (1), (4) and (6) are to be solved subject to boundary conditions are

at the wall $(y = 0):$ $u = v = 0;$ $T = T_w$

at the free-stream (as $y \to \infty$): $u = U_\infty;$ $\qquad (7)$

$T = T_\infty$

As the first step in solving the system of partial differential Eqs. (1), (4) and (6) are transformed into ordinary differential equations using the transformation from (x, y) coordinates to $(\xi(x), \eta(x, y))$ coordinates by introducing

$$\xi = \xi(x), \qquad \eta = y\left(\frac{U_\infty}{\nu x}\right)^{1/2} \qquad (8)$$

The coordinate $\eta(x, y)$ is a pseudo-similarity variable which reduces to a true similarity variable for boundary layers that are similar. The coordinate $\xi(x)$ depends only

x and is so chosen that x doest not appear explicitly in the transformed conservation equations and their boundary conditions. In addition, one introduces a dimensionless stream function $F(\xi, \eta)$ and a dimensionless temperature $\theta(\xi, \eta)$ defined as,

$$F(\xi, \eta) = \frac{\psi(x, y)}{\sqrt{\nu U_\infty x}}, \qquad \theta(\xi, \eta) = \frac{T - T_\infty}{T_w - T_\infty} \quad (9)$$

where $\psi(x, y)$ is the stream function that satisfy the continuity Eq. (1) automatically with

$$u = \frac{\partial \psi}{\partial y}, \qquad v = -\frac{\partial \psi}{\partial x} \quad (10)$$

Substitution of Eqs. (8) and (9) into Eqs. (6), (4) and (7), one gets the system of governing equations as,

$$F''' + \frac{1}{2}FF'' + \frac{1}{2}\xi\left[\eta\theta + \int_\eta^\infty \theta\, d\eta + \xi \int_\eta^\infty \left(\frac{\partial\theta}{\partial\xi}\right) d\eta\right]$$
$$= \frac{1}{2}\xi\left[F'\left(\frac{\partial F'}{\partial\xi}\right) - F''\left(\frac{\partial F}{\partial\xi}\right)\right] \quad (11)$$

$$\frac{1}{\mathrm{Pr}}\theta'' + \frac{1}{2}F\theta' = \frac{1}{2}\xi\left[F'(\frac{\partial\theta}{\partial\xi}) - \theta'(\frac{\partial F}{\partial\xi})\right] \quad (12)$$

$$F'(\xi, 0) = 0, \quad F(\xi, 0) = 0, \quad \theta(\xi, 0) = 1.0 \quad (13)$$

$$F'(\xi, \infty) = 1.0, \qquad \theta(\xi, \infty) = 0 \quad (14)$$

where the primes denote partial differentiation with respect to η; Pr is the Prandtl number; $\xi(x)$ is the buoyancy parameter and the expression as,

$$\xi = \frac{\mathrm{Gr}_x}{\mathrm{Re}_x^{5/2}} \quad (15)$$

where $\mathrm{Gr}_x = [g\beta_t(T_w - T_\infty)x^3]/\nu^2$ is the local Grashof number; $\mathrm{Re}_x = (U_\infty x)/\nu$ is the local Reynolds number. For assisting mixed convection flow (flow above the plate) when the buoyancy parameter (ξ) is positive value in Eqs. (11) and (12). For opposing mixed convection flow (flow below the plate) when ξ is negative value in Eqs. (11) and (12). The pure forced convection flow over a horizontal plate occurs when $\xi = 0$. As ξ is a function of x, the system of governing Eqs. (11) and (12) are called non-similar mixed convection boundary layer equations.

The non-similar mixed convection boundary layer Eqs. (11) and (12) to be solved with the boundary conditions as given in Eqs. (13) and (14) to obtain the velocity and temperature profiles in the boundary layer. The

physical quantities of interest are the local Nusselt number (Nu_x) and the local friction factor (C_f) to know the convective heat transfer rate and skin friction respectively. These quantities are defined as,

$$\mathrm{Nu}_x = \frac{h_x x}{k} = \frac{-k\left(\frac{\partial T}{\partial y}\right)_{y=0}}{T_w - T_\infty}\frac{x}{k} = -\sqrt{\mathrm{Re}_x}\,\theta'(\xi, 0) \quad (16)$$

$$C_f = \frac{\mu\left(\frac{\partial u}{\partial y}\right)_{y=0}}{1/2\rho U_\infty^2} = 2\mathrm{Re}_x^{-1/2}F''(\xi, 0) \quad (17)$$

where h_x is the local convective heat transfer coefficient; k is the thermal conductivity of the fluid; and μ is the dynamic viscosity of the fluid.

3. NUMERICAL METHODS

The non-similar mixed convection boundary layer Eqs. (11) and (12) are transformed into five first order ordinary differential equations. These ordinary differential equations are numerically integrated from the wall ($y = 0$) using fourth order Runge-kutta method (RK-4) with Newton-Raphson shooting method to satisfy the conditions at the edge of the boundary layer as given in Eq. (14).

The major differences in the numerical solution of the present problem and those encountered in conventional boundary layer problems lies in the handling of integral terms and differential terms with respect to ξ which appear in Eqs. (11) and (12). For the success of shooting technique using a Newton-Raphson method requires a very good initial guess values of $F''(\xi, 0)$ and $\theta'(\xi, 0)$. Here, grid-search method is used to obtain good initial guess values. Details of grid-search method are given in Venkatasubbaiah et al. (2006). Integral terms in Eqs. (11) and (12) are evaluated using Simpson's $1/3$ rule. For example, the evaluation of integral term in Eq. (11) using Simpson's $1/3$ rule is given below

$$\int_{\eta=0}^{\eta_{\max}} \theta\, d\eta = \frac{\Delta\eta}{3}\left[\theta(0) + 4\sum_{i=1,3,5}^{n-1}\theta(i) \right.$$
$$\left. + 2\sum_{i=2,4,6}^{n-2}\theta(i) + \theta(n)\right] \quad (18)$$

where $\theta(0)$ is the non dimensional temperature at the wall ($\eta = 0$); $\theta(n)$ is the non dimensional temperature at the free-stream condition ($\eta_{\max} = 10$) Differential terms with

respect to ξ in Eqs. (11) and (12) are evaluated using backward finite difference scheme. For example, the evaluation of differential term with respect to ξ in Eq. (11) using backward finite difference scheme is given below

$$\frac{\partial F'}{\partial \xi} = \frac{F'_{\xi_{current}} - F'_{\xi_{previous}}}{\xi_{current} - \xi_{previous}} \tag{19}$$

To solve the Eqs. (11) and (12) for a prescribed value of ξ, one needs to start by guessing the values of F, F' and θ to evaluate integrals in Eqs. (11) and (12) in addition to guessing the unavailable starting values of $F''(\xi, 0)$ and $\theta'(\xi, 0)$. The solution for $\xi = 0$ or $\xi = \xi_{previous}$ is considered as initial guess values to evaluate the integrals in Eqs. (11) and (12). These inputs enable the Eqs. (11) and (12) to be integrated using RK-4 across the boundary layer and simultaneously with this integration, F, F' and θ values are evaluated. These values are employed to replace the initial guess values for evaluating the integrals, but the initial guesses for $F''(\xi, 0)$ and $\theta'(\xi, 0)$ values are retained. With these inputs for the evaluation of integrals, integration of boundary layer equations are repeated and new values are used to evaluate integrals. This procedure is repeated by keeping $F''(\xi, 0)$ and $\theta'(\xi, 0)$ fixed values until the input and output F, F' and θ values lies with in a prescribed tolerance. Then, $F''(\xi, 0)$ and $\theta'(\xi, 0)$ values are altered with Newton-Raphson shooting method to satisfy the boundary conditions at the edge of the boundary layer. All numerical calculation are done here using double precision with $\eta_{max} = 10$ equally divided into 4000 points in the η direction. The error criterion in the shooting method converges to less than 10^{-8}.

4. RESULTS AND DISCUSSION

The non-similar mixed convection boundary layer Eqs. (11) and (12) are solved by Direct integration method as discussed in Section 3 without any approximation for non-similar terms. Results are reported for assisting and opposing mixed convection flows over a horizontal plate for air. Here, the value of Prandtl number (Pr) is 0.7 for all the cases. Results are reported for laminar flows with buoyancy parameter (ξ) varying from -0.025 to 0.3. The positive values of ξ refer to assisting mixed convection flow (flow above the plate) and the negative values of ξ refer to opposing mixed convection flow (flow below the plate).

The velocity and temperature profiles in the boundary layer have been obtained for the cases of $\xi = 1.0 \times 10^{-6}, 0.05$ as shown in Figs. 1 and 2. From Figs. 1(a) and
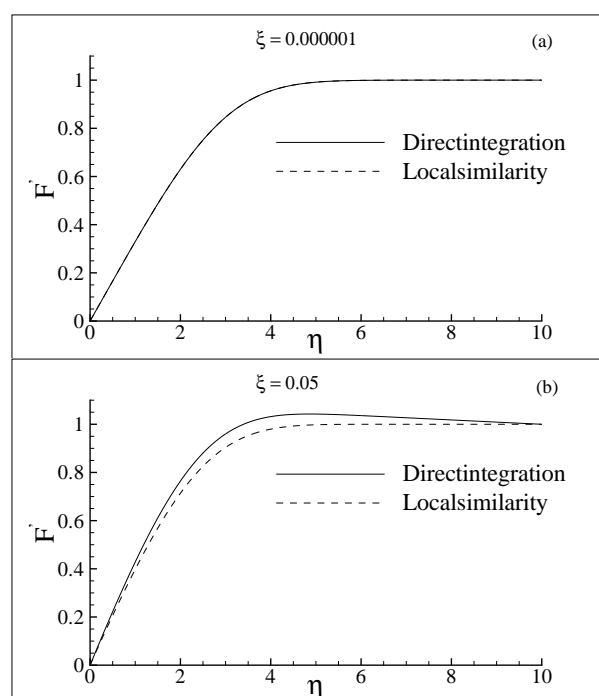
FIG. 1: Velocity profile in the boundary layer for **(a)** $\xi = 1.0 \times 10^{-6}$ and **(b)** $\xi = 0.05$.

2(a), one notice that the velocity and temperature profiles exactly matches compared to local similarity method. In Figs. 1(a) and 2(a), there is no visible difference between lines because Direct integration line is superposition on local similarity line. As the ξ increases to 0.05, the velocity and temperature profiles in the boundary layer are differ from local similarity method as shown in Figs. 1(b) and 2(b). Reported velocity and temperature profiles are high accuracy compared to local similarity method because non-similar terms are evaluated without any approximation. Local Nusselt number (Nu_x) and local friction factor (C_f) values are obtained using Eqs. (16) and (17) for $\xi = 1.0 \times 10^{-6}$. These values are slightly varying compared to local similarity and local non-similarity methods as shown in Figs. 3 and 4. As discussed in introduction, local similarity and local non-similarity methods solutions are based on approximation for non-similar terms.

Local Nusselt number (Nu_x) values are obtained with different buoyancy parameter (ξ) as shown in Fig. 3, with the results of present investigation shown by solid line. In Fig. 3, local similarity and local non-similarity solutions are shown by dotted lines and long dash lines re-

FIG. 2: Temperature profile in the boundary layer for **(a)** $\xi = 1.0 \times 10^{-6}$ and **(b)** $\xi = 0.05$.
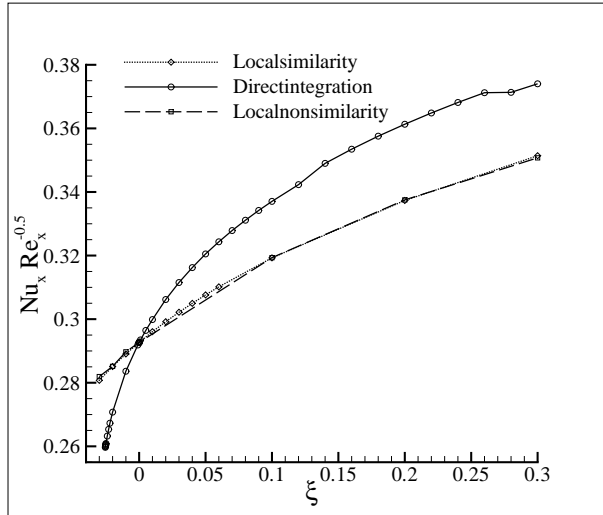
FIG. 3: Local Nusselt number (Nu_x) values for assisting and opposing mixed convection flows.

FIG. 4: Local friction factor (C_f) values for assisting and opposing mixed convection flows.

spectively. From Fig. 3, the variation of Nusselt number with ξ is consistent with the expected effects of favorable and adverse pressure gradients. When ξ is positive, the buoyancy induces a favorable pressure gradient which accelerates the flow and increases the Nusselt number. From Fig. 3, the convective heat transfer coefficient increases with increasing buoyancy parameter for assisting mixed convection flow. When ξ is negative, the buoyancy induces an adverse pressure gradient which retards the flow and decreases the Nusselt number. This also indicates convective heat transfer coefficient decreases with increasing buoyancy parameter for opposing mixed convection flow. From Fig. 3 , the local Nusselt number values are close agreement compared to local similarity and local non-similarity methods for very small values of ξ. As ξ increases in assisting mixed convection flow, the local Nusselt number values are high compared to local similarity and local non-similarity methods. As ξ increases in opposing mixed convection flow, the local Nusselt number values are less compared to local similarity and local non-similarity methods. Reported Nu_x values are of high accuracy compared to local similarity and local non-similarity methods because non-similar terms are evaluated without any approximation.

Local friction factor (C_f) values are obtained with different buoyancy parameter (ξ) as shown in Fig. 4, with the results of present investigation shown by solid line. In Fig. 4, local similarity and local non-similarit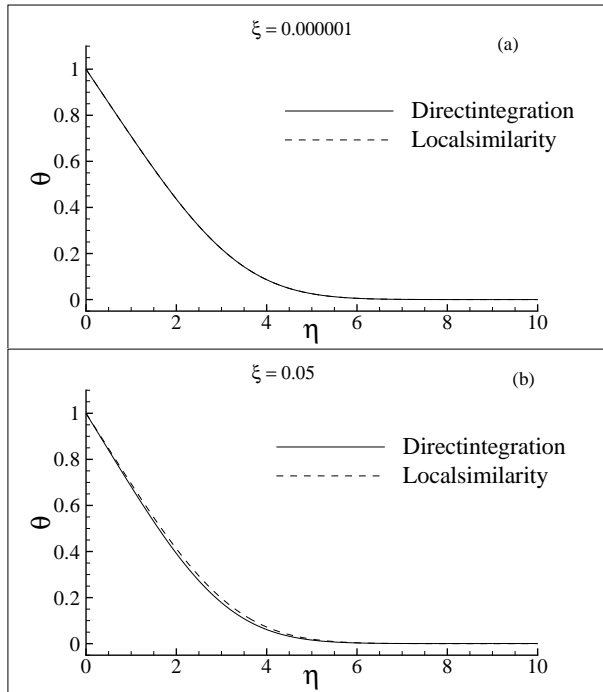y solutions are shown by dotted lines and long dash lines respectively. When ξ is positive, the buoyancy induces a favorable pressure gradient which accelerates the flow and increases the skin friction. From Fig. 4, the skin friction

increases marginally with increasing buoyancy parameter for assisting mixed convection flow. When ξ is negative, the skin friction drops off as the adverse pressure gradient retards the flow. From Fig. 4, the local friction factor values are close agreement compared to local similarity and local non-similarity methods for very small values of ξ. As ξ increases in assisting mixed convection flow, the local friction factor values are high compared to local similarity and local non-similarity methods. As ξ increases in opposing mixed convection flow, the local friction factor values are less compared to local similarity and local non-similarity methods.

Sudden dip of local Nusselt number and local friction factor values appears at a particular value of buoyancy parameter as shown in Figs. 3 and 4. Physically, this dip could be attributed to a pseudo-interference effect caused by the deceleration of the flow and piling up of the boundary layer. A combination of these effects tends to thicken the boundary layer and suppress the Nu_x and C_f values. Similar trends of Nu_x variation are reported experimentally by Wang (1982) for mixed convection flow over a horizontal plate.

The velocity and temperature fields in the boundary layer have been obtained with different buoyancy parameter (ξ) and representative velocity and temperature profiles are shown in Figs. 5 and 6. From Fig. 5, one can notice that for assisting mixed convection flows, velocity gradient at the wall is increases as the ξ increases. For assisting flows, the effect of buoyancy is to increase the velocity compared to pure forced convection case ($\xi = 0$) and an overshooting of the velocity beyond its free stream

FIG. 6: Temperature profiles in the boundary layer for different buoyancy parameter (ξ).

value as ξ increases. Figs. 1 and 5, shows that significant buoyancy force effects are occurring from $\xi = 0.05$ onwards compared to pure forced convection case. For opposing mixed convection flows, the effect of buoyancy is to reduce the velocity compared to pure forced convection. From Fig. 6, one can notices that for assisting mixed convection flows, temperature gradient at the wall is increases and the thermal boundary layer thickness is decreases as the ξ increases. The opposite trend is shown for opposing mixed convection flows.

5. CONCLUSIONS

Results of analysis have been presented here for non-similar laminar mixed convection boundary layer flow over a horizontal plate using high accuracy direct integration method without any approximation for non-similar terms. Results are given for assisting (flow above the plate) and opposing (flow below the plate) mixed convection flows in air when the buoyancy effects are small compared to forced convection effects. The non-similar mixed convection boundary layer Eqs. (11) and (12) are solved using Fourth order Runge-kutta method with Simpson's 1/3 rule to evaluate integrals and backward finite difference scheme for evaluating differential terms with respect to ξ as given in Section 3. The velocity and temperature profiles in the boundary layer have been obtained for small values of ξ as shown in Figs. 1 and 2. Results from Figs. 1(a) and 2(a), show that velocity and temperature profiles are exactly matching compared to local sim-

FIG. 5: Velocity profiles in the boundary layer for different buoyancy parameter (ξ).

ilarity method for $\xi = 1.0 \times 10^{-6}$. Local Nusselt number (Nu_x) and Local friction factor (C_f) values are obtained for different values of buoyancy parameter (ξ) as shown in Figs. 3 and 4. From Figs. 3 and 4, both the Nu_x and C_f values increase with increasing buoyancy parameter for assisting mixed convection flows and decreases with increasing buoyancy parameter for opposing mixed convection flows. Results also reveal that for assisting mixed convection flows, Nu_x and C_f values are high compared to local similarity and local non-similarity methods. For opposing flows, Nu_x and C_f values are less compared to local similarity and local non-similarity methods. The velocity and temperature profiles in the boundary layer have been obtained for varying ξ as shown in Figs. 5 and 6. As $\xi \geq 0.05$ the buoyancy effects become significant compared to pure forced convection case ($\xi = 0$). For assisting mixed convection flows, the effect of buoyancy is to increase the velocity compared to pure forced convection as shown in Fig. 5. For high values of ξ, the velocity exhibit an overshoot beyond the free stream velocity. For opposing flows, the effect of buoyancy is to reduce the velocity compared to pure forced convection as shown in Fig. 5. Results from Fig. 6, show that the thickness of the thermal boundary decreases with increasing buoyancy parameter for assisting mixed convection flows and increases with increasing buoyancy parameter for opposing mixed convection flows. Reported results are high accuracy compared to local similarity method since non-similar terms are evaluated correctly.

REFERENCES

Brewstar, R. A. and Gebhart, B., Instability and disturbance amplification in a mixed convection boundary layer, *J. Fluid Mech.*, vol. **229**, pp. 115–133, 1991.

Chen, T. S., Sparrow, E. M., and Mucoglu, A., Mixed convection in boundary layer flow on a horizontal plate, *J. Heat transfer, TRANS. ASME*, vol. **99**, pp. 66–71, 1977.

Gebhart, B., Jaluria, Y., Mahajan, R. L., and Sammakia, B., *Buoyancy-Induced Flows and Transport*, Hemisphere Publication, Washington DC, 1988.

Hussain, T. and Afzal, N., Mixed convection boundary layer flow on a horizontal plate in a uniform stream, *Int. J. Heat Mass Transfer*, vol. **31**(12), pp. 2505–2516, 1988.

Mori, Y., Buoyancy effects in forced laminar convection flow over a horizontal flat plate, *J. Heat transfer, TRANS. ASME*, vol. **83**, pp. 479–482, 1961.

Schneider, W., A similarity solution for combined forced and free convection flow over a horizontal plate, *Int. J. Heat Mass Transfer*, vol. **22**, pp. 1401–1406, 1979.

Sparrow, E. M. and Minkowycz, W. J., Buoyancy effects on horizontal boundary layer flow and heat transfer, *Int. J. Heat Mass Transfer*, vol. **5**, pp. 505–511, 1962.

Venkatasubbaiah, K., Amrita Mittal, and Sengupta, T. K., Non-unique solution for combined convection assisting flow over vertical plate, *Sādhanā*, vol. **31**(6), pp. 709–719, 2006.

Wang, X. A., An experimental study of Mixed, forced, and free convection heat transfer from a horizontal flat plate to air, *J. Heat Transfer, TRANS. ASME*, vol. **104**, pp. 139–144, 1982.

DEPRESSURIZATION EFFECTS ON THE THERMAL FIELDS AND HEAT TRANSFER DURING HEMI-SPHERICAL BUBBLE GROWTH ON A HEATED SURFACE

A. J. Robinson

Department of Mechanical and Manufacturing Engineering, Trinity College, Dublin, Ireland, E-mail: arobins@tcd.ie

A numerical simulation has been carried out which predicts the growth and wall heat-transfer characteristics of a bubble atop a heated flat surface in an otherwise quiescent pool of liquid. In accordance with the experimental conditions and observations of Merte et al. (1995), the simulations are carried out on a constant heat flux surface in microgravity, and the bubble maintains a hemispherical shape with no contribution of a microlayer. The model, computational technique, and interface tracking methodology provide very high spatial and temporal resolution. This is true for the micrometer-sized nucleus in metastable equilibrium with its surrounding liquid at the end of the measured waiting time, through the surface tension, transition, and heat transfer controlled growth domains where the bubble expands to macro-sized. The simulations indicate that the rapid depressurization of the vapor bubble as it expands occurs in conjunction with a like drop in the vapor temperature. This establishes a substantial temperature gradient and subsequent evaporative cooling effect of the heater surface near the moving triple interface. The influence of bulk liquid advection and transient conduction is discussed in relation to the bubble dynamics.

KEY WORDS: *bubble growth, nucleate boiling, contact line heat transfer*

1. INTRODUCTION

Perhaps the oldest and most widely used method for heat-transfer enhancement is nucleate boiling. Whether in pool boiling or convective boiling applications, the extremely high heat-transfer rates associated with the nucleate pool boiling phenomenon are intimately linked to the vapor bubbles which form, grow, and depart at the heated surface. Energy is introduced into the liquid by conduction from the heated solid surface and is stored within a thin thermal boundary layer adjacent to that surface. This stored energy is ultimately used to vaporize the liquid and cause bubbles to form and grow. In addition to evaporative cooling effects, fluid motions induced by bubble activity disrupt the thermal boundary layer in the vicinity of the bubbles, causing enhanced mixing and improved heat transfer in these regions (Dhir, 1991).

The earliest attempts at developing mechanistic models of nucleate boiling heat transfer in the isolated bubble regime mainly focused on heat-transfer enhancement during the waiting time between bubble departure and the nucleation of the next bubble. For single bubble events, the high heat-transfer rates were thought to be a result of the destruction of the thermal boundary layer at the wall due to the bubble growth and departure phase. As a consequence, the waiting time becomes a period of low thermal resistance due to transient thermal boundary-layer growth, i.e., transient conduction (Forster and Greif, 1959; Mikic and Rohsenow, 1969; Han and Griffith, 1965). A phenomenon first alluded to by Snyder and Edwards (1956) and validated experimentally by Moore and Mesler (1961) provided significant insight into the boiling process by providing evidence that during the initial rapid expansion phase, a very thin microlayer can form under-

NOMENCLATURE

Notation

A	area (m^2)
a	coefficient $\left\{z_\eta^2 + r_\eta^2\right\}$
b	coefficient $\left\{r_\varepsilon r_\eta + z_\varepsilon z_\eta\right\}$
c	coefficient $\left\{z_\varepsilon^2 + r_\varepsilon^2\right\}$
D_j	radial grid parameter (m)
d	coefficient $\left\{J^{-1}(r_\eta\beta_1 - z_\eta\beta_2)\right\}$
e	coefficient $\left\{J^{-1}(z_\varepsilon\beta_2 - r_\varepsilon\beta_1)\right\}$
C_p	specific heat (J/kg K)
h_{fg}	latent heat of evaporation (J/kg)
J	Jacobian $\left\{z_\eta r_\varepsilon - z_\varepsilon r_\eta\right\}$
k	thermal conductivity (W/m K)
n	normal direction
P	pressure (Pa)
r	radial direction (m)
R	bubble radius (m)
S_R	grid clustering parameter
t	time (s)
T	temperature (°C)
U	radial velocity (m/s)

V	axial velocity (m/s)
z	axial direction (mm)

Greek symbols

α	thermal diffusivity (m^2/s)
β_1	coefficient $\left\{az_{\varepsilon\varepsilon} - 2bz_{\eta\varepsilon} + cz_{\eta\eta}\right\}$
β_2	coefficient $\left\{ar_{\varepsilon\varepsilon} - 2br_{\eta\varepsilon} + cr_{\eta\eta}\right\}$
δ	thermal boundary-layer thickness (m)
ε	transformed computational coordinate
η	transformed computational coordinate
ρ	density (kg/m^3)
σ	surface tension (N/m)
γ	angle (-)
τ	time before bubble nucleation
τ^*	waiting time

Subscripts

l	liquid
sat	saturation condition
sup	superheat
v	vapor
ff, ∞	far field

neath the base of the growing bubble. During a complete bubble cycle, evaporation of the microlayer provides additional surface cooling during the bubble growth phase. With transient conduction during the waiting period and microlayer evaporation during the initial growth phase as the primary mechanisms of heat transfer, several models have been developed which attempt to quantify the heat removal rates during boiling (van Stralen et al., 1975; Zhao et al., 2002; Judd and Hwang, 1976; Fath and Judd, 1978).

Boiling dynamics are very sensitive to a vast array of interrelated parameters making exhaustive experimentation difficult. Furthermore, bubble dynamics are associated with small time and length scales such that measurements with adequate temporal and spatial resolution are difficult to obtain. It has been until very recently that reliable time- and space-resolved measurements in the vicinity of bubbles have been provided in the open literature (Wagner et al., 2006; Demiray and Kim, 2004; Golobic et al., 2007). In particular, the pioneering microscale heat-transfer experiments by Professor Jungho Kim's re-

search group at the University of Maryland have not only lead to a refined understanding of the relative contributions of transient conduction and microlayer evaporation, but have unveiled a significant mechanism of heat transfer which had not been considered previously. Utilizing micoscale surface-mount hot-wire-type technology, it has been shown conclusively that during the departure phase of the bubble the inward motion of the triple interface draws in cooler bulk liquid to the vicinity of the heater surface and establishes a period of enhanced heat transfer due to transient conduction (Demiray and Kim, 2004).

Lee and Nydahl (1989) were one of the first to put forth a numerical model of bubble growth and heat transfer for an isolated bubble growing atop a constant temperature surface. In the model both the contribution of the microlayer and the superheated macrolayer were included for a bubble of assumed truncated sphere geometry with a sharp wedge-shaped microlayer. For an assumed initial temperature profile based on one-dimensional transient conduction in a semi-infinite solid, the final solutions were obtained by tuning an adjustable parameter in

the expression for the leading edge thickness of the micro-layer until experimental bubble growth curves were adequately predicted. The results indicated that microlayer evaporation played the dominant role in determining the wall heat-transfer rates as well as the bubble growth rates, with 90% of the energy for bubble growth provided by the microlayer. However, recent experimental evidence (Demiray and Kim, 2004) tends to dispute these findings, with less than 15% of the energy required to produce the bubble being contributed by the microlayer, with the remaining provided by the relaxation macrolayer surrounding the bubble cap. Later, Mei et al. (1995a) presented a numerical formulation of bubble growth and heat transfer with geometrical simplifications similar to those of Lee and Nydahl (1989). Furthermore, Mei et al. (1995a) adopted an analogous parameter for the microlayer as in Lee and Nydahl (1989), albeit for a range of boiling conditions, together with a second empirical parameter to define the degree of truncation of the bubble based on the Jacob number. An important development in this work was including the solid phase and elucidating its influence on the energy transfer during bubble growth, which was deemed to be important (Mei et al., 1995b). Noting the reliance of previous computational models on empiricism, adjustable parameters, and other constraining assumptions such as assumed bubble shape, Welch (1998) developed a "correlation-free" numerical approach for bubble growth and heat transfer. This direct numerical simulation utilized a novel interface tracking method in conjunction with a finite volume method on a moving unstructured mesh. Although excessive compression and distorting of the mesh required that the simulations be terminated very early on in the bubble life, the results did seem to predict the possible formation of a microlayer region beneath the bubble.

Son et al. (1999) successfully implemented the level set method to capture and adequately represent the shape of the vapor–liquid interface during bubble growth on a constant temperature surface, thus alleviating much of the difficulty experienced by Welch (1998) with the unstructured mesh scheme. The level set method could also handle breaking and merging of interfaces, which provided physical insight into the hydrodynamics and heat transfer of bubble departure in a more realistic manner compared with Lee and Nydahl (1989). Son et al. (1999) also divided the computational domain onto two separate regions; the micro region, containing the thin film that forms beneath the bubble where lubrication theory was applied, and the macro region, consisting of the bubble and the surrounding liquid where the standard forms

of the equations of conservation were applied. Although the method did not rely on as many simplifying assumptions compared with Lee and Nydahl (1989) and Mei et al. (1995a, 1995b) and improved on the numerical stability of Welch (1998), the computation did rely on a priori knowledge of the dispersion constant relating the disjoining pressure to the film thickness in the microlayer. The choice of the dispersion constant influences the apparent contact angle, which in turn influences the bubble growth dynamics and heat transfer. Apart from a major advancement in computational methods for this type of problem, the main contributions of this work were the observation of the inward and outward motion of the triple contact line, more realistic contribution of the microlayer (∼20%), and the effect of contact angle, i.e., wettability, on the bubble growth characteristics.

The beginning of this century has seen a notable increase in the number of archival publications related to numerical modeling of heterogeneous bubble growth in partial nucleate boiling along with many other boiling scenarios, such as convective boiling, bubble merger, and boiling in minichannels. Regarding nucleate pool boiling in the isolated bubble regime, the works of Bai and Fujita (2000), Yoon et al. (2001), Robinson and Judd (2001), Genske and Stephan (2006), Fuchs et al. (2006), Dhir (2006), Wu et al. (2007), Stephan and Fuchs (2007), and Mukherjee and Kandlikar (2007) are particularly pertinent, and the work of Genske and Stephan (2006) and Stephan and Fuchs (2007) are relevant to contact line heat transfer. In these works the surface heat transfer in the immediate vicinity of the bubble was investigated for three distinct regions: an absorbed film region under the bubble where the thermal resistance is very high, a micro region where the heat flux is highest, and a macro region where the bubble interacts with the bulk liquid to influence the heat transfer. Genske and Stephan (2006) studied the relative contribution of the micro and macro regions, including the considerable influence of fluid flow on the heat transfer in the macro region. Stephan and Fuchs (2007) built upon previous work to describe the heat flow in all three phases in the vicinity of the bubble during all the bubble ebullition cycles. By performing energy budgets, it was shown that during the bubble growth and detachment period, more heat was consumed by evaporation into the bubble than was supplied, causing a cooling effect within the solid and liquid phases. The bubble rise and waiting time had associated with them a period of heating, as less heat was extracted by evaporation than supplied. Consistent with the observations of Mei et al. (1995a) and others such as Guo and El-Genk (1994), it was concluded that

the thermophysical properties of the solid phase, in particular, its ability to store and release heat, plays a nontrivial role in the bubble growth and heat transfer. Furthermore, they showed some qualitative agreement between the computations and recent high-resolution temperature measurements under a growing bubble in microgravity.

On this last point, one major deficiency in the literature is the lack of adequately controlled experiments for validation of numerical simulations of bubble growth dynamics for surface boiling. The initial thermal and flow fields are required as input parameters for numerical models, and these are rarely specified since the preponderance of measurements are taken at earth gravity and/or during steady boiling conditions. Natural convection and liquid agitation due to previous or neighboring bubbles not only negate exact specification of the initial and boundary conditions, but also result in large scatter in measured bubble growth curves for ostensibly the same condition (Lee and Nydahl, 1989). Typically, the computational community must resort to implementing a rather crude approximation of a linear temperature distribution in a liquid boundary layer of thickness prescribed from empirical correlations for free convection for both the initial and far-field conditions (Son et al., 1999; Genske and Stephan, 2006; Fuchs et al., 2006; Mukherjee and Kandlikar, 2007). In some instances (Genske and Stephan, 2006; Stephan and Fuchs, 2007; Mukherjee and Kandlikar, 2007), no validation against measured bubble growth curves is provided to establish the efficacy of the computations. In other cases (Lee and Nydahl, 1989; Son et al., 1999; Dhir, 2006, Wu et al., 2007), agreement with measurements is provided subsequent to tuning one or more adjustable parameters.

The boiling experiments reported in Lee (1993), Merte et al. (1995), and Lee and Merte (1996) partially overcome the ambiguity associated with earth gravity and steady surface boiling experiments by heating a stagnant pool of liquid to the onset of nucleate boiling in microgravity. The absence of any significant natural convection, combined with the fact that the thermal and flow fields are not influenced by previous or neighboring bubbles, provided the well-defined initial and boundary conditions required as input parameters for an accurately posed numerical simulation. Photographic evidence also indicated that microgravity bubble growth for this scenario can be characterized by a lengthy hemispherical growth stage due to the lack of buoyancy forces and the relatively low heat fluxes for the tests carried out. Admittedly, this type of controlled test environment and methodology is not exactly representative of fully developed steady-state nucleate boiling. Even still, the well-defined and controlled ex-

periments can, in conjunction with an appropriate numerical simulation, provide rich information with regard to the thermal-physics of heterogeneous bubble growth and heat transfer that is not necessarily available from other works.

Robinson (2002) and Robinson and Judd (2001) developed a two-dimensional model and numerical technique which was rigorously validated against all of the space microgravity and drop tower microgravity surface boiling measurements provided by Merte et al. (1995). The model developed in Robinson and Judd (2001) is specific to the test cases upon which it was validated and is at a disadvantage compared with other models which incorporate more advanced aspects such as bubble shape, departure and liftoff, micro region/microlayer evaporation, and conduction in the solid phase. Even still, the model utilized a grid generation and front tracking technique that, in conjunction with high temporal resolution, facilitated numerical stability for a mesh that was sufficient to resolve bubble growth dynamics from the microscale to the macroscale, including the immense acceleration between the *surface tension* and *transition* growth stages.

Although Robinson and Judd (2001) implemented their numerical model to investigate the dynamics of bubble growth on a heated surface in microgravity, they did not consider the influence of the bubble growth on the local thermal fields and heat transfer along the boiling surface, whereas Robinson (2007) showed that this may be significant. This investigation is a continuation of the works detailed in Robinson and Judd (2001) and Robinson (2007). Here, the influence of the bubble dynamics on the thermal field and heat-transfer augmentation near the advancing triple interface is quantified for a single test case and the physical mechanisms explained as the bubble transits through the *surface tension*, *transition,* and *heat-transfer* growth domains.

2. PHYSICAL MODEL, MATHEMATICAL FORMULATION, AND NUMERICAL SIMULATION

2.1 Governing Equations

Figure 1 illustrates the physical model employed in the mathematical modeling of this work. As consistent with the measurements provided in Merte et al. (1995), a hemispherical bubble is expanding atop a heated and flat solid surface. The conservation equations which adequately describe the bubble growth dynamics are those of conservation of mass, momentum, and energy within the liquid
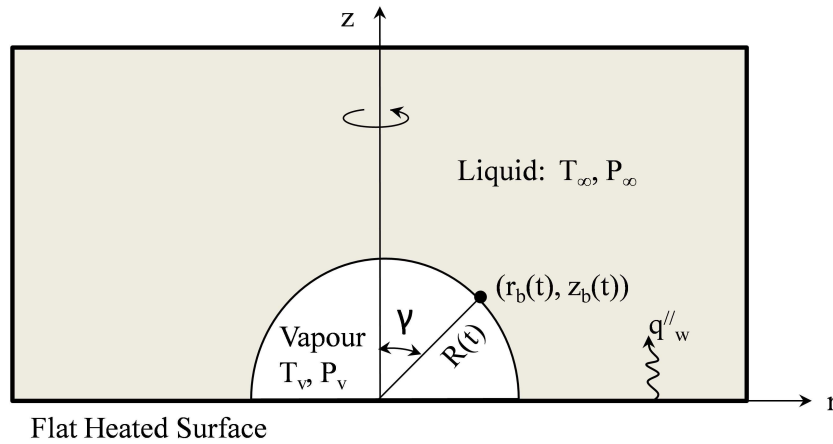
FIG. 1: Hemispherical bubble growth on a heated surface.

phase. As transport phenomena within the vapor phase has negligible influence on the heat-transfer coefficient (Fuchs et al., 2006), the fluid flow and heat transfer within the vapor phase is not considered and the vapor phase is thus modeled as a quiescent and uniform temperature and pressure region.

In this investigation the flow of the liquid phase is considered to be purely radial, and there is no contribution of the evaporating microlayer to bubble growth and heat transfer. As a result of the purely radial flow assumption, the conservation of mass within the liquid phase reduces to analytic solutions of the radial, U, and translational, V, liquid velocity distributions,

$$U = \frac{dR}{dt} \left(\frac{R}{(r^2 + z^2)^{1/2}} \right)^2 \sin(\gamma)$$
$$V = \frac{dR}{dt} \left(\frac{R}{(r^2 + z^2)^{1/2}} \right)^2 \cos(\gamma) \tag{1}$$

Furthermore, integration of the momentum equation results in the ordinary differential equation, which relates the net pressure differential between the bubble interface pressure, $P_L(R)$, and the ambient static pressure, P_∞, to the hydrodynamic stresses acting on the bubble interface,

$$P_L(R) - P_\infty = \rho_l R \frac{d^2R}{dt^2} + \rho_l \frac{3}{2} \left(\frac{dR}{dt} \right)^2 \tag{2}$$

In Eq. (2) the normal component of the viscous stress has been neglected, because for the case considered here it is negligible compared with the magnitude of the other terms (Robinson and Judd, 2001).

The thermal energy transfer within the liquid phase, and thus, the time varying temperature distribution within the liquid, is described by the energy equation for axisymmetric cylindrical coordinates;

$$\frac{\partial T}{\partial t} + U \frac{\partial T}{\partial r} + V \frac{\partial T}{\partial z} = \alpha_l \left(\frac{\partial^2 T}{\partial r^2} + \frac{1}{r} \frac{\partial T}{\partial r} + \frac{\partial^2 T}{\partial z^2} \right) \tag{3}$$

The final set of equations that is required for a solution to the bubble growth problem is related to the quasi-equilibrium force and energy balances at the vapor–liquid interface. A quasi-static force balance at the interface results in the Young–Laplace equation, which relates the pressure difference across the interface to the surface tension stresses such that;

$$P_v(t) = P_L(R) + \frac{2\sigma}{R} \tag{4}$$

Combining Eq. (4) with Eq. (2) results in the familiar extended Rayleigh equation,

$$P_v(t) - P_\infty = \rho_l R \frac{d^2R}{dt^2} + \rho_l \frac{3}{2} \left(\frac{dR}{dt} \right)^2 + \frac{2\sigma}{R} \tag{5}$$

Finally, an energy balance at the interface which equates the heat transfer within the liquid to the latent heat generation within the vapor phase results in the expression

$$\frac{dQ}{dt} = \int_{A_s} k_l \left(\frac{\partial T}{\partial n} \right)_{R(t)} dA = 2\pi R^2 \left(\rho_v h_{fg} \frac{dR}{dt} + h_{fg} \frac{R}{3} \frac{d\rho_v}{dt} \right) \tag{6}$$

where the temperature gradient is taken with respect to the normal direction, n, for the instantaneous bubble radius, $R(t)$.

2.2 Numerical Solution

To assure high temporal resolution, a fourth-order Runge–Kutta scheme was implemented to determine the updated variables at each progressive time step. The Runge–Kutta scheme involves the definition of three simultaneous ordinary differential equations for the variables T_v, R, and dR/dt such that

$$y_1 = T_v, \quad y_2 = R, \quad y_3 = \frac{dR}{dt} \qquad (7)$$

where

$$\frac{dy_1}{dt} = \left(\frac{h_{fg}}{3} \frac{d\rho_v(y_1)}{dT_v} y_2 \right)^{-1} \left(\frac{1}{2\pi R^2} \int_A k_l \left. \frac{\partial T}{\partial n} \right|_R dA \right. \qquad (8)$$
$$\left. - h_{fg} \rho_v y_3 \right)$$

$$\frac{dy_2}{dt} = y_3 \qquad (9)$$

and

$$\frac{dy_3}{dt} = \frac{P_v(y_1) - P_\infty}{\rho_l y_2} - \left(\frac{3}{2} \frac{y_3^2}{y_2} + \frac{2\sigma}{\rho_l y_2^2} \right) \qquad (10)$$

Equation (8) is obtained by defining the vapor density, ρ_v, as a function and vapor temperature, T_v, and rearranging Eq. (6). The last differential equation listed above was developed by defining the vapor pressure, P_v, as a function of vapor temperature, T_v, and rearranging Eq. (5). For a given time step, the solution of the above system of equations requires that the values y_1, y_2, and y_3 be known at the beginning of the time interval, and the fourth-order Runge–Kutta scheme is implemented to determine the updated values.

The solution of the three ordinary differential equations requires that the instantaneous thermal field be provided for the liquid at each time step. This provides the temperature gradients normal to the interface required in Eq. (8). The two-dimensional temperature distribution in the liquid phase was determined by solving Eq. (3). The energy equation was solved numerically on a grid which was constructed using an algebraic grid generation technique. The grid variables in the physical domain are depicted in Fig. 2(a). Grid clustering near the vapor–liquid interface, as well the moving boundary, were facilitated by defining the instantaneous grid such that
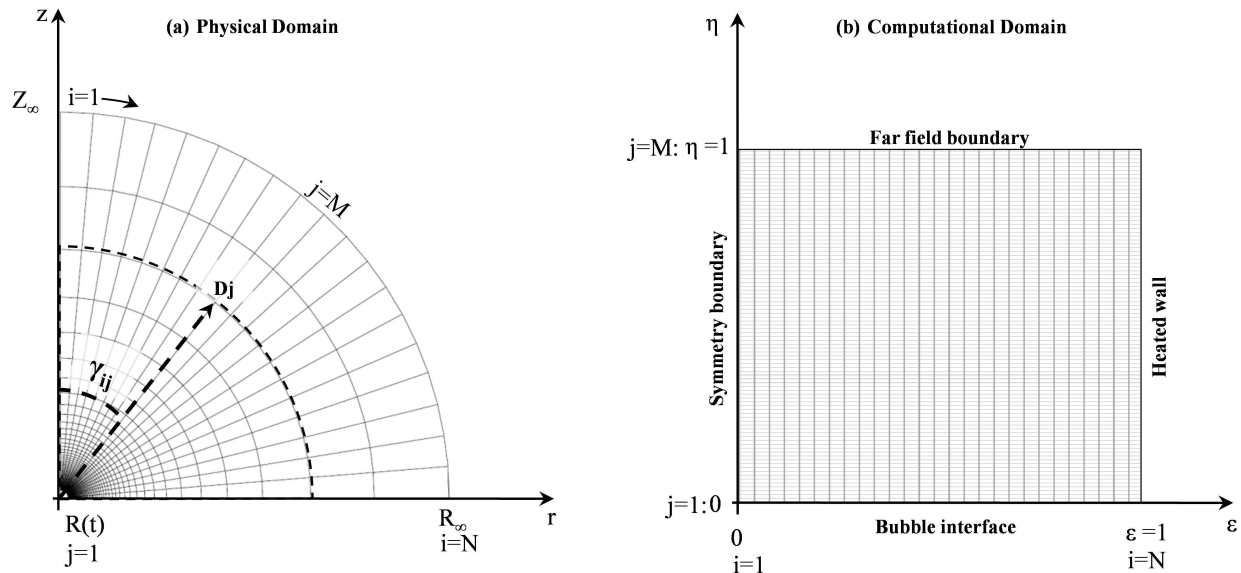

FIG. 2: Mesh and relevant parameters in the **(a)** physical domain and **(b)** the computational domain subsequent to coordinate transformation.

$$r_{ij} = D_j \sin(\gamma_{ij}), \quad z_{ij} = D_j \cos(\gamma_{ij}) \qquad (11)$$

where

$$\gamma_{ij} = \frac{\pi}{2}\left(\frac{i-1}{N-1}\right)$$

$$D_j = R + (R_\infty - R)\left(1 - S_R \tan^{-1}\right. \qquad (12)$$

$$\left.\times\left[\left(1 - \frac{j-1}{M-1}\right)\tan\left(\frac{1}{S_R}\right)\right]\right)$$

R_∞ was maintained at 2.5 cm for all simulations, and the term S_R, which determines the percentage of grid points near the interface, was kept constant at $S_R = 0.65$. An example of the grid is depicted in Fig. 2(a). In order to capture the rapidly moving interface, a front fixing technique was employed whereby the moving physical domain with spatial coordinates (r,z), depicted in Fig. 2(a), was transformed onto a stationary and rectangular grid within a transformed coordinate domain (ε, η), illustrated in Fig. 2(b). The transformation is given by

$$r = r(\varepsilon, \eta, \lambda), \quad z = z(\varepsilon, \eta, \lambda), \quad t = \lambda \qquad (13)$$

Using subscript notation to denote partial differentiation with respect to the subscript variable, the first derivatives of temperature become;

$$T_r = (z_\eta T_\varepsilon - z_\varepsilon T_\eta)/J$$

$$T_z = (r_\varepsilon T_\eta - r_\eta T)/J \qquad (14)$$

$$T_t = T_\lambda - T_r r_\lambda - T_z z_\lambda$$

The contravarient velocities are defined as

$$U^c = (U - r_\lambda)z_\eta - (V - z_\lambda)r_\eta$$
$$V^c = (V - z_\lambda)r_\varepsilon - (U - r_\lambda)z_\varepsilon \qquad (15)$$

The transformed energy equation on the stationary rectilinear computational domain is thus

$$T_\lambda + \frac{U^c T_\varepsilon}{J} + \frac{V^c T_\eta}{J} = \left(\frac{\alpha}{J^2}\right)\left(aT_{\varepsilon\varepsilon} - 2bT_{\varepsilon\eta} + cT_{\eta\eta}\right.$$
$$\left. + dT_\varepsilon + eT_\eta\right) + \left(\frac{\alpha}{Jr}\right)(z_\eta T_\varepsilon - z_\eta T_\eta) \qquad (16)$$

where coefficients a through e and the Jacobian, J, are defined in the Nomenclature section.

Equation (16) was discretized using second-order central difference representations of the spatial derivatives and a fully implicit first-order representation of the time derivatives. At a given time step, the temperature field

was determined using successive over-relaxation (SOR) by lines. For each line the resulting system of algebraic expressions was solved utilizing the tri-diagonal matrix algorithm (TDMA). The code was developed in FORTRAN 90.

The initial and boundary conditions used were chosen to be consistent with the experimental conditions and observations of Merte et al. (1995). The initially quiescent and uniform temperature liquid was allowed to heat due to a step increase in wall heat flux of $q_w^{//}$ at $\tau = 0$. At the end of the waiting time, $\tau = \tau^*$, bubble nucleation occurs and the initial temperature field is that which is determined from the analytic solution of transient thermal conduction in a semi-infinite solid,

$$T(r, z, t = 0) = T(z, \tau^*) = T_\infty$$
$$+ \frac{2q_w^{//}\sqrt{\alpha_l \tau^*/\pi}}{k_l}\exp\left(-\frac{z^2}{4\alpha_l\tau^*}\right) \qquad (17)$$
$$- \frac{q_w^{//} z}{k_l}\mathrm{erfc}\left(\frac{z}{\sqrt{w\alpha_l\tau^*}}\right)$$

For a given heat flux the magnitude of the waiting time determines how much energy is stored within the thermal boundary layer adjacent to the heated wall and thus influences the bubble growth dynamics. This has been investigated by Liao et al. (2004), where it was found that the longer waiting times have associated higher bubble growth rates. From the moment of bubble nucleation, i.e., $t = \tau - \tau^* \geq 0$, the boundary conditions are as follows;

$$T(r_b, z_b, t) = T_v(t)$$

$$T(R_\infty, Z_\infty, t) = T_\infty + \frac{2q_w^{//}\sqrt{\alpha_l(t+\tau^*)/\pi}}{k_l}$$
$$\times \exp\left(-\frac{z^2}{4\alpha_l(t+\tau^*)}\right) - \frac{q_w^{//} z}{k_l}\mathrm{erfc}\left(\frac{z}{\sqrt{w\alpha_l(t+\tau^*)}}\right) \qquad (18)$$

$$\frac{\partial T}{\partial r}(0, z, t) = 0, \quad \frac{\partial T}{\partial z}(r, 0, t) = \frac{q_w^{//}}{k_l}$$

The inner boundary of the liquid phase is in contact with the vapor bubble. Here, the interface temperature is assumed to be equal to that of the instantaneous vapor temperature, $T_v(t)$. In the undisturbed far-field region, the temperature increased in accordance with the analytic solution of transient thermal conduction in a semi-infinite solid. Along $r = 0$ a symmetry boundary condition is imposed, whereas the wall heat flux is kept constant along the heated wall at $z = 0$.

During heterogeneous boiling, a bubble nucleates from a vapor nucleus which has been trapped within a small pit, scratch, or crevice existing on the surface. The radius of the mouth of the cavity is believed to be an important factor in determining the time it takes for the vapor nucleus to begin significant growth because it partially dictates the initial thermodynamic state of the bubble. This dimension is extremely difficult to measure and is rarely, if ever, given as a part of the measured variable set, which corresponds to an experimental bubble growth curve. With no knowledge of the cavity size from which the bubble nucleates, the initial bubble radius was determined by assuming that the vapor is initially saturated with a temperature equal to that of the wall temperature at the end of the experimentally determined waiting time, i.e., $T_v(0) = T(r, 0, \tau^*)$, as predicted by Eq. (17). The stationary hemispherical vapor nucleus exists in metastable thermodynamic equilibrium with the quiescent surroundings with internal pressure $P_{\text{sat}}(T_v)$ and extends from the mouth of a cavity with a radius predicted by the Young–Laplace equation,

$$R_c = \frac{2\sigma}{P_{\text{sat}}\left[T_v(0)\right] - P_\infty} \tag{19}$$

2.3 Solution Algorithm

The main components of the solution algorithm are similar to those described in Lesage et al. (2009) and are as follows;

1. Set the input system pressure P_∞, heat flux $q_w^{//}$, and waiting time τ^* along with relevant geometric grid and time step parameters.

2. Calculate the initial temperature profile in the liquid utilizing Eq. (17) and calculate the initial nucleus radius with Eq. (19).

3. Set / update the variables $y_1 = T_v$, $y_2 = R$, $y_3 = dR/dt$ in Eq. (7).

4. Apply a time step and implement the fourth-order Runge–Kutta for the system of ordinary differential equations (Eqs. (8)–(10). The interfacial heat flux distribution required in Eq. (8) is determined at each phase of the fourth-order Runge–Kutta scheme by solving the energy equation using SOR lines as discussed earlier.

5. If the growth time is less than the preset termination time, go to step 3. If the growth time is equal to the termination time, update all relevant variables and stop the simulation.

2.4 Validity of Assumption in Physical Model and Simulations

The adequacy of the physical modeling and numerical solution technique has been confirmed by comparing the simulations against analytical, numerical, and experimental data for spherically symmetric bubble growth in a uniformly superheated liquid over an extremely wide range of boiling conditions (Robinson and Judd, 2001; Robinson, 2002). This is accomplished by simply setting $q_w^{//} = 0.0$ W/cm^2 in Eq. (18), which simulates a symmetry boundary condition along $z = 0$, i.e., $(\partial T/\partial r)(r, 0, t) = 0$, as well as posing a constant and uniform temperature initially and on the far-field boundary. The case of boiling on a heated surface in which the thermal field is two-dimensional has also been validated by showing excellent agreement with all of the available drop tower microgravity and space microgravity experiments provided in Merte et al. (1995) and Lee (1993). Some of the one-dimensional spherically symmetric and two-dimensional nonsymmetric results are plotted in Fig. 3. Robinson (2002) performed a full numerical sensitivity analysis, including, but not limited to, ensuring that the simulated results were grid- and time step–independent, and the placement of the far-field boundary was sufficiently large to approximate a semi-infinite domain. Since $R_\infty \gg R(t)$, the final term on the right side of Eq. (12) is not sensitive to the instantaneous bubble size. Thus, as the bubble expands the grid locations are redistributed within the computational domain in such a way that the grid points near the interface are approximately the same distance from the interface at all times ($\sim$0.1 μm). In this way adequate resolution of the thermal field can be achieved for the 3 orders of magnitude increase in bubble size. Furthermore, in conjunction with the high temporal resolution afforded by the fourth-order Runge–Kutta scheme, the large thermal gradients associated with the early growth stages, particularly when the bubble accelerates away from the *surface tension* domain entering *transition* domain (Robinson and Judd, 2001), are adequately resolved.

Because this work is approximate and not an exact numerical simulation, it is important to briefly discuss the major assumptions which have been made during the physical modeling of the problem since they ultimately determine the usefulness and limitations of any conclusions which are drawn from the results. Furthermore, any conclusions drawn from the simulations must not be ap-
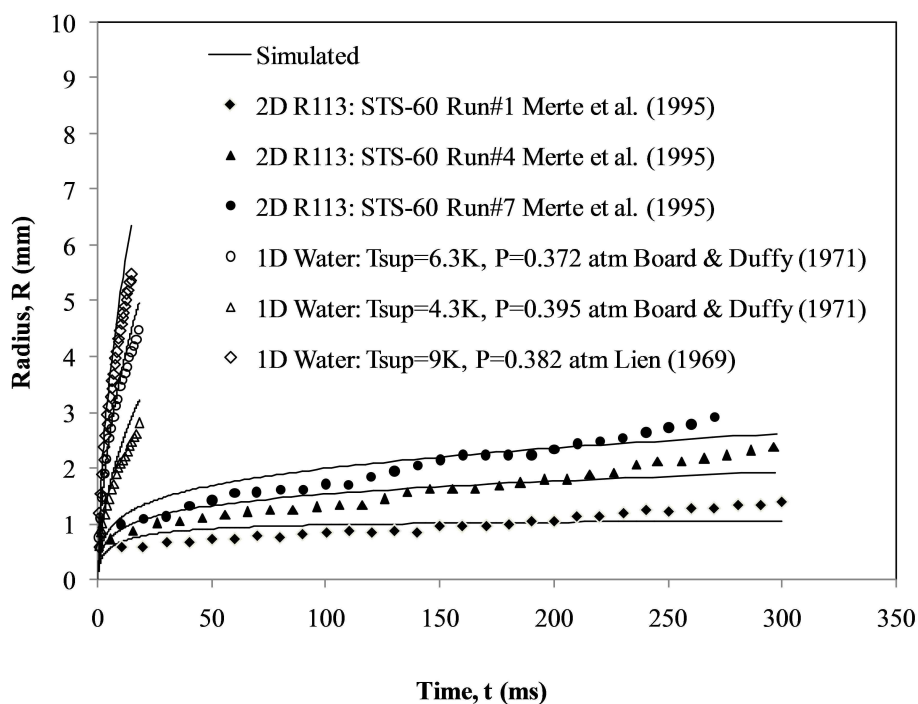
FIG. 3: Simulations versus experimental measurements for both homogeneous bubble growth (open markers) and heterogeneous growth in microgravity (filled markers).

plied directly to situations for which the assumptions are inappropriate. The soundness of the assumptions must be specific to the experiments to which the simulations have been compared and validated. As has been mentioned, for the case considered here, the surface boiling validation experiments have been provided by Merte et al. (1995). The assumed initial and boundary conditions on the thermal and flow field are all very reasonable considering the experimental setup and procedure, as discussed previously. In-depth numerical analysis is provided by Merte et al. (1995), which further supports these assumptions. Even still, the constant heat flux boundary condition is difficult to realize experimentally, since the triple interface is a strong heat sink and may induce lateral conduction within the heater substrate toward this region. Guo and El-Genk (1994) performed calculations within a thin conductive heater layer of SnO_2 upon a thick glass substrate for the case of microlayer evaporation, also a very strong heat sink. During the growth phase, temperature variations were mostly confined within the 30-μm-thick SnO_2 layer. During the waiting period subsequent to bubble departure, the change in the temperature field in the glass substrate layer is noticeable. Because the quartz sub-

strate has a similar conductivity to glass and the gold film heaters used in the experiments of Merte et al. (1995) were between 400 and 1400 Å thick, it is reasonable as a first approximation to assume minimal lateral conduction, provided the simulations are for the bubble growth stage. Even still, since the wall substrate has not been included in the physical model, the heat-transfer coefficients determined in this study must be considered as conservative, because lateral conduction will tend to increase the evaporative heat flux near the triple interface (Dhir, 2006). The wall temperature beneath the bubble is not considered and the vapor is considered insulated from the heated wall. Since the bubble accelerates to a radius of approximately $R \approx 1.0$ mm very rapidly, the characteristic timescale for the vapor bubble during the subsequent transient can be approximated as $(R/2)^2/\alpha_v \approx 150$ ms. Considering the bubble as a lumped system, this would indicate that neglecting the influence of the heated wall beneath the bubble on the bubble growth rate is appropriate for smaller time values and would become gradually less so as time progresses beyond ~150 ms. This may partially explain why the experimental growth curves of bubbles STS-60.#1,4, & 7 and the numerical simulations

shown in Fig. 3 tend to diverge for values of time beyond approximately 200 ms.

The geometric simplification that the bubble expands with a fixed and hemispherical shape with no microlayer decreases the complexity of the problem considerably. The physical mechanisms of microlayer formation, growth, and dryout are not established theoretically. Apart from Welch (1998), who observed only the possible beginning of microlayer formation, the microlayer is typically defined in an ad hoc manner and is often tuned to match simulations with experiments. Including a microlayer in this manner for the work carried out here would increase the growth rate and size of the bubbles by a considerable margin, possibly up to 20%. The agreement between experiments and the simulation would suggest that this is not rational, and for the low-heat-flux cases under investigation, no microlayer was formed. This is somewhat confirmed by the observations made from simultaneous high-speed photographs taken from the side and from the underside of the bubbles which were growing on a transparent surface. Here the radius of the dry patch on the underside grew at the approximate rate of the side-view radius.

Some other key assumptions which were made in simplifying the problem include the fact that non-thermodynamic equilibrium effects and thermocapillary convection have been ignored. It is somewhat difficult to provide indisputable arguments as to the validity of these assumptions, since they are topics of considerable debate in the open literature. However, it is generally true that the more pure and degassed the liquid is, the more valid these assumptions become. In the experiments provided in Merte et al. (1995), special care was taken to ensure that the R113 was very pure and degassed.

3. RESULTS AND DISCUSSION

3.1 Bubble Growth Dynamics

The bubble growth dynamics have been discussed in detail by Robinson and Judd (2001, 2004) and are summarized here for completeness. The test case under consideration corresponds with the growth of a R113 vapor bubble on a heated plane surface in zero gravity for an imposed wall heat flux of $q_w^{//} = 1.138$ W/cm^2, which is 17.5% of the total heat input for bubble number STS-60 Run#4 in Lee (1993). Experimental and numerical results indicated that this fraction of the heat input was transferred into the bulk liquid with the rest conducted through the quartz substrate (Merte et al., 1995). The sys-

tem conditions were $P_\infty = 117.3$ kPa, $T_{\text{sat}} = 52°$C, $T_\infty = 48.8°$C, $\tau^* = 0.74$ s, and $T_w(\tau^*) = 83.2°$C, where τ^* is the experimentally determined waiting time for bubble STS-60 Run#4.

As the bubble grows from a micrometer-sized nucleus to a millimeter-sized bubble it passes through three distinct growth domains. These are depicted in Fig. 4 as the *surface tension domain*, the *transition domain*, and the *heat-transfer domain*. As shown in Fig. 4(a), the early *surface tension domain* of growth is characterized by almost imperceptible changes in bubble radius. As such, the bubble interface velocity shown in Fig. 4(b) is so small that hydrodynamic forces on the bubble are negligible and surface tension is the dominant stress term on the right side of Eq. (5). Since the bubble is expanding the vapor pressure is decreasing, albeit very slowly. Consequently, the rate at which the vapor temperature decreases is very low as well, as seen in Fig. 4(b). Even still, a minute increase in radius, as a result of the positive flow of energy into the bubble, causes a slight drop in the vapor pressure with a corresponding drop in the vapor temperature. This drop in temperature increases the driving temperature difference, which increases the rate of heat transfer, which in turn raises the growth rate. In this way, the bubble expansion accelerates due to positive thermal feedback, whereby the growth of the bubble is responsible for escalating its own rate of growth.

At approximately $t = 0.0001$ ms a sufficiently high heat flux into the bubble is generated and the bubble growth accelerates very rapidly. This is evident in Fig. 4(b), where a rapid rise of the bubble interface velocity from nearly zero to 6.5 m/s in the span of about 1.0 μs is observed. If the bubble were to expand unconstrained, the thermal feedback would become exceptional and the vapor temperature would drop to its minimum value of $T_{\text{sat}}(P_\infty)$ nearly instantly, causing physically unrealistic heat flux levels and subsequent growth rates and bubble sizes. To mitigate this, the rate at which the vapor pressure and temperature drop is held back by the influence of the hydrodynamic forces at the vapor–liquid interface. In the *transition domain*, the surface tension force in Eq. (5) decreases due to the expanding radius while at the same time the hydrodynamic force terms, generated because the bubble must set the surrounding liquid into significant motion, increase to such an extent as to become dominant. This is primarily the term proportional to $(dR/dt)^2$ in Eq. (5). The increased hydrodynamic forces result in a more gradual rate of decrease in the vapor temperature beyond approximately 0.001 ms, which in turn influences the rate of heat transfer and the growth rate.
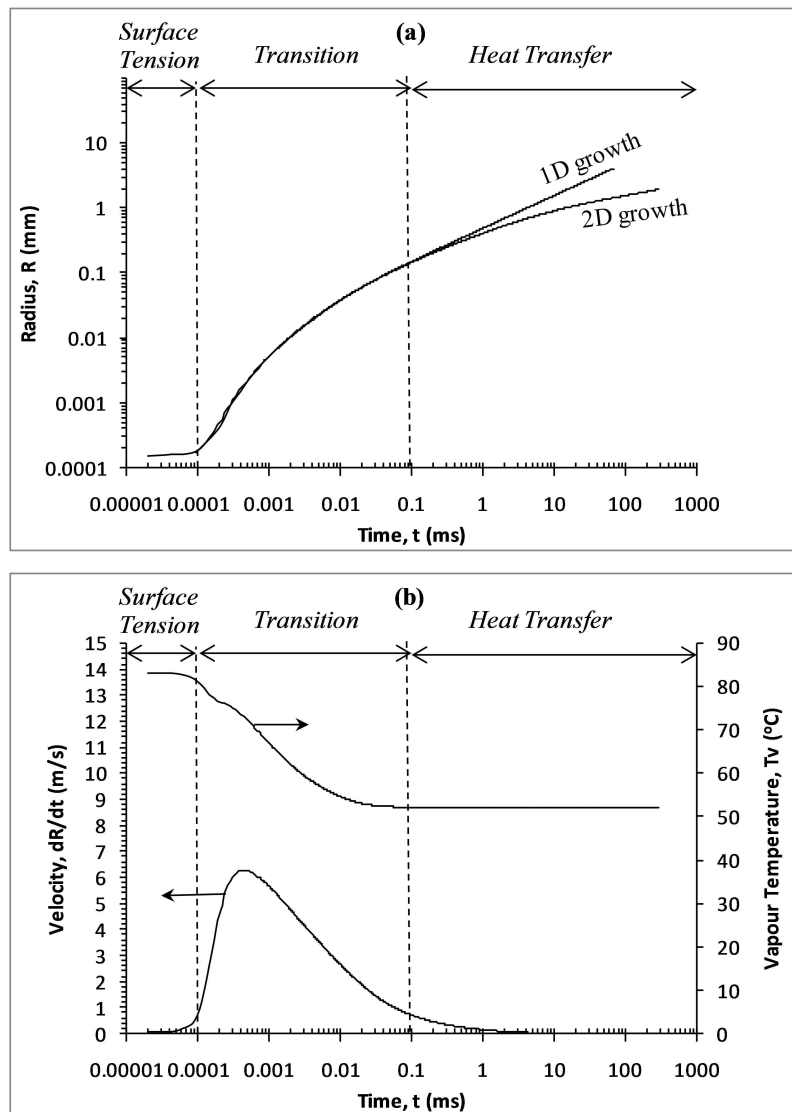
FIG. 4: **(a)** Bubble growth curves for 1D simulation and 2D simulation, and **(b)** vapor temperature and bubble interface velocity histories.

Even though the acceleration associated with this growth domain is considerable, the mass of the bubble is so small that the rate of change of linear momentum is still negligible compared with the magnitude of the forces acting on the bubble (Lesage, 2009). As such, a quasi-static force balance which includes the dynamical effects of the liquid interfacial pressure is still justified.

The final *heat-transfer domain* is characterized by the fact that the bubble has expanded to such an extent that the vapor temperature has reached its minimum value of $T_{\mathrm{sat}}(P_\infty) = 52°C$. As a result, the thermal feedback effect, which is fundamental in determining the growth characteristics in the previous two domains, is no longer important because bubble expansion is now occurring at constant vapor temperature. Furthermore, Fig. 4(b) indicates that the bubble interface velocity diminishes substantially in this domain as well.

An important effect in this late stage of growth is that the rate of heat transfer, and thus, the bubble growth rate, becomes highly nonuniform around the bubble surface.

The one-dimensional homogeneous bubble growth curve, assuming that the liquid temperature distribution was initially uniform and equal to the wall temperature at nucleation ($T_v = 83.2°C$), is also plotted in Fig. 4(a). From the figure it is evident that the heterogeneous (2D) bubble growth curve is nearly the same as that for homogeneous (1D) growth in a uniformly superheated liquid during the *surface tension* and *transition* growth domains. This occurs because the bubble is small enough compared with the thickness of the thermal boundary layer above the heated wall that the temperature of the liquid around the bubble is nearly uniform. This is illustrated in Fig. 5(a), where the isotherms are plotted around the bubble for an instant within the transition domain ($t = 0.01$ ms). Conversely, Figs. 5(b) and 5(c) illustrate that during the *heat-transfer domain* the bubble has grown to such an extent that it protrudes from the thermal boundary layer, thus exposing a significant portion of its surface to the subcooled bulk liquid. This has the effect of reducing the net rate of heat transfer into the bubble, and thus the observed growth rate, as compared with the one-dimensional growth case.

3.2 Heat Transfer Near the Triple Interface

3.2.1 Data Reduction

The primary objective of this work is to elucidate the mechanism of heat transfer near the moving triple interface that was noted by Robinson (2007). Figure 6 shows a schematic of the side view of the bubble in order to illustrate the main parameters. As will be discussed, the presence of the expanding bubble on the constant heat flux surface considered here causes a cooling effect along the wall near the triple interface. Since localized events are being considered and the effective wall heat transfer is characterized by the intensity of the evaporative heat transfer at the triple interface, the local heat-transfer coefficient is defined as

$$h(r) = \frac{q_w^{//}}{T(r,t) - T_v(t)} \tag{20}$$

Here, $T(r,t)$ denotes the local wall temperature, and the instantaneous vapor temperature, $T_v(t)$, has been chosen because the primary heat sink near the triple interface is
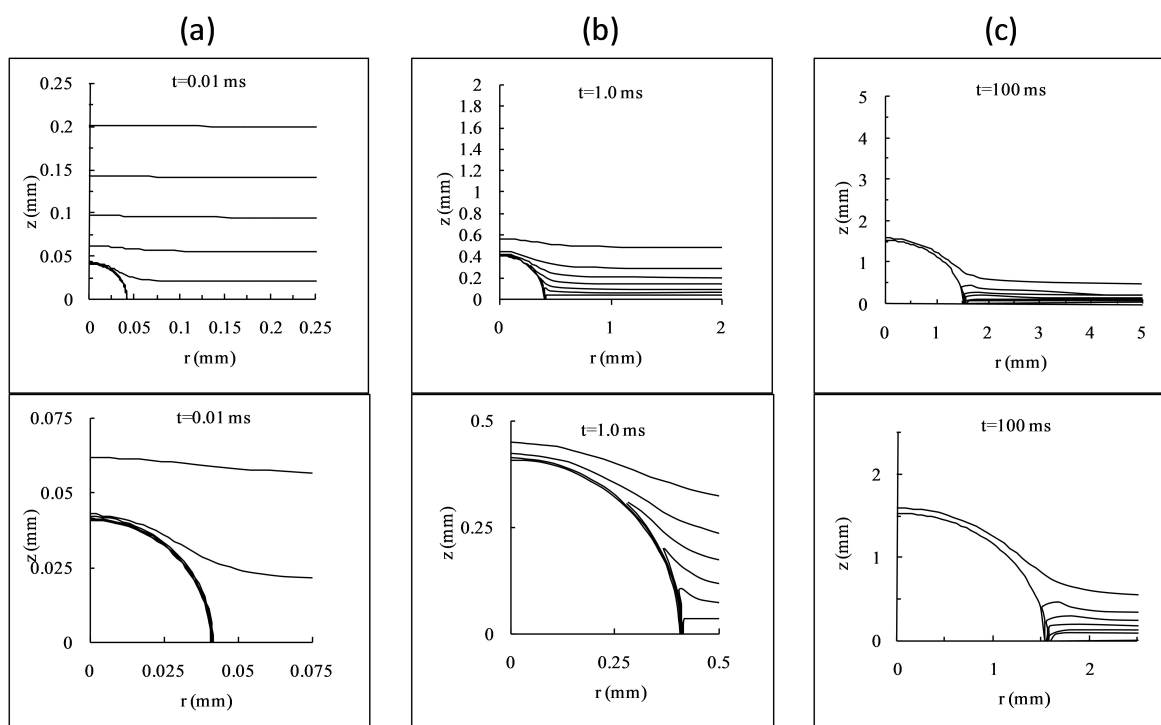

FIG. 5: Isotherms surrounding the growing bubble at different times during growth: **(a)** within the transition domain, $t = 0.01$ ms; **(b)** near the beginning of the heat-transfer domain, $t = 1.0$ ms; and **(c)** within the heat-transfer domain, $t = 100$ ms; (top) exploded view and (bottom) closeup. In each figure the isotherms are separated by $5°C$ increments.
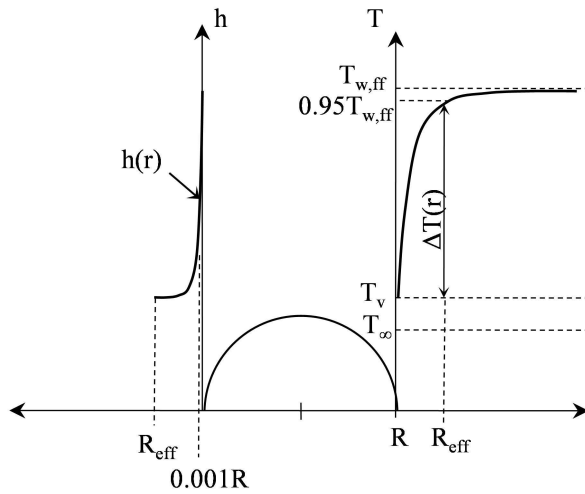
FIG. 6: Heat transfer near the moving triple interface.

the vapor bubble itself and not the bulk liquid. This differs from Robinson (2007) in which the bulk liquid temperature, T_∞, was selected. As depicted in Fig. 6, the effective radius within which the heat - transfer coefficient is considered "enhanced" is to be defined as the radius at which the wall temperature has increased to 95% of the far-field temperature;

$$R_{\text{eff}} = r|_{T(r)=0.95T_{w,ff}} \qquad (21)$$

Likewise, the instantaneous effective area over which this enhancement occurs can be defined as

$$A_{\text{eff}} = \pi(R_{\text{eff}}^2 - R_o^2) \qquad (22)$$

The area average heat-transfer coefficient acting over the affected area is given by the expression

$$h_{\text{avg}} = \frac{1}{A_{\text{eff}}} \int_{Ro}^{R_{\text{eff}}} 2\pi r \cdot h(r)\, dr \qquad (23)$$

Since $T(r,t) \to T_v(t)$ as $r \to R$, the heat-transfer coefficient, as defined by Eq. (20), approaches infinity at the triple interface. To provide some qualitative information regarding the instantaneous area-averaged heat-transfer coefficient, the lower limit of integration in Eq. (23) was chosen as $R_o = 1.001R$ from the bubble interface. The region $R_o \leq r \leq R_{\text{eff}}$ can be considered an effective region of bulk enhancement, where evaporative effects are significant with regard to heat transfer. As such, h_{avg} and $h(R_o)$ can be considered to represent the relative strength of the heat transfer within this area.

For qualitative comparison of the relative intensity of the heat transfer near the triple interface and the far-field regions, the instantaneous thermal conductance at the wall in the undisturbed far field was determined by applying an approximation of Newton's law of cooling for an effective thermal boundary-layer thickness of $\delta(t)$ in a semi-infinite medium with wall temperature $T(\infty, 0, t)$ and bulk fluid temperature T_∞ such that

$$\left(\frac{k_l}{\delta(t)}\right)_{ff} \cong -\frac{q_w^{//}}{T(\infty, 0, t) - T_\infty} \qquad (24)$$

This can be seen to represent the intensity of the heat transfer if there were no bubble present, although the bulk temperature T_∞ is used in Eq. (24), not $T_v(t)$ as in Eq. (20).

3.2.2 Mechanism of Heat Transfer

Figure 7 shows the heater wall temperature distribution measured from the triple interface at different times during the bubble growth where the temperature at $r/R(t) = 1$ represents the instantaneous vapor temperature, $T_v(t)$.

As was discussed previously and shown in Fig. 4(a), within the *transition domain* of bubble growth the vapor temperature decreases from a maximum of $T_v(t = 0) = 83.2°C$ to a minimum of $T_{\text{sat}}(P_\infty) = 52°C$ due to depressurization of the bubble as it expands away from its nucleus radius. The rate at which this occurs is determined by the relative influence of hydrodynamic and surface tension forces acting on the bubble. In the earliest stage of the transition domain (roughly 0.001 ms$\leq t \leq$ 0.005 ms), Fig. 4(b) indicates that the interface velocity increases to its maximum. As a consequence, the strong liquid advection near the interface causes the temperature profiles to be less steep relative to the bubble radius, as indicated in Fig. 7(a). Beyond $t \approx 0.005$ ms the interface velocity decreases and thus, the influence of liquid advection diminishes, causing the thermal gradients to become steeper. This combined with the fact that $T_v(t)$ is near its minimum value results in temperature profiles which nearly overlap as the influence of transient conduction becomes more important. During the *heat-transfer domain* the bubble vapor temperature remains virtually constant at $T_{\text{sat}}(P_\infty)$ and the interfacial velocity diminishes to the extent that it has little influence on the wall temperature distribution. Here the thermal profiles develop as a result of transient conduction, as depicted in Fig. 7(b), with the thermal boundary layer adjacent to the bubble growing with time. The far-field temperature increases above

FIG. 7: Heater surface temperature distribution near the triple interface at different times during the bubble growth phase for **(a)** transition domain and **(b)** heat-transfer domain.

$T_v(t = 0)$ for $t > 10$ ms due to transient conduction in the semi-infinite medium.

The local heat-transfer coefficient distributions near the triple interface are depicted in Fig. 8, where only the data for the region of $0 \leq R \leq R_{eff}$ is plotted for each curve. Figure 8(a) indicates that the during the *transition domain* the general trend is for the magnitude of the local heat-transfer coefficient in the affected area to decrease

with time. In the immediate vicinity of the interface this is because the increased strength of liquid advection causes the slope of the temperature profiles to be smallest for the smaller values of time as the cooler liquid penetrates deeper into the bulk. In the far field this effect is combined with the fact that heat sink temperature, $T_v(t)$, is decreasing with time, reducing the intensity of the heat transfer as the driving temperature differential in Eq. (20)
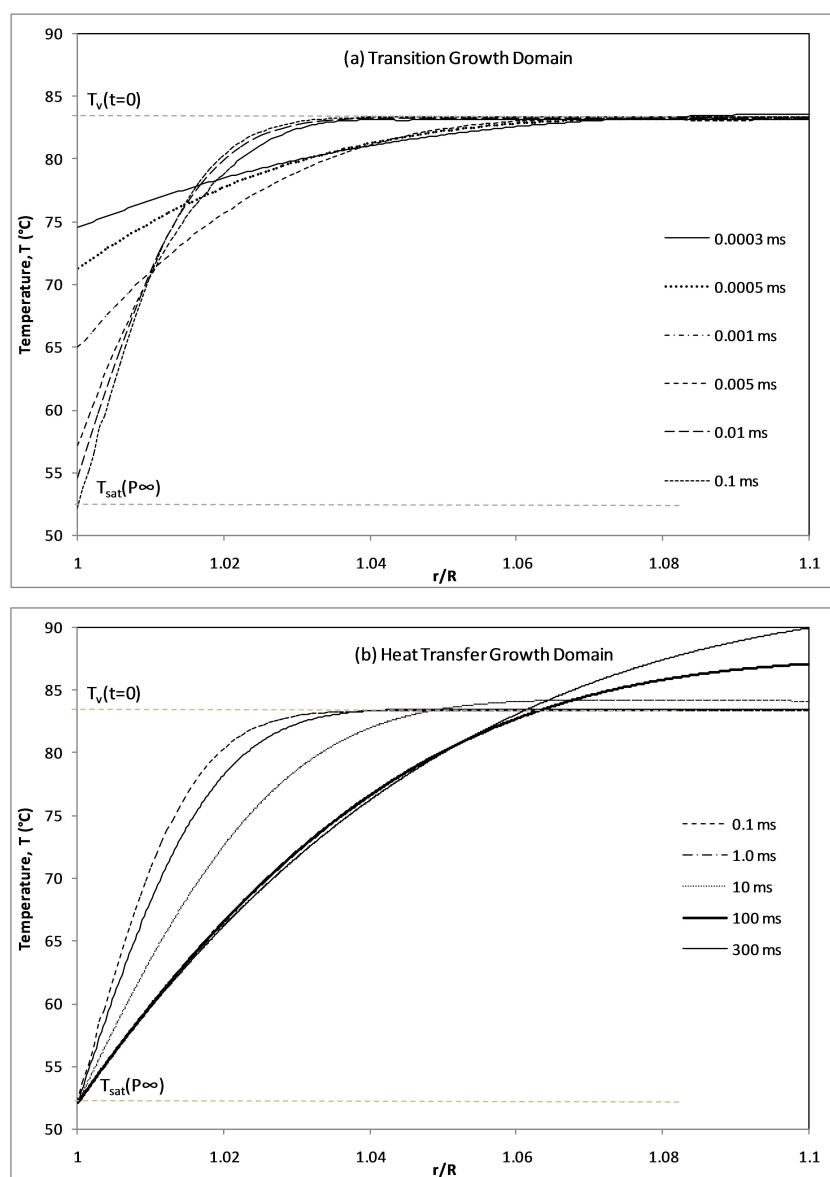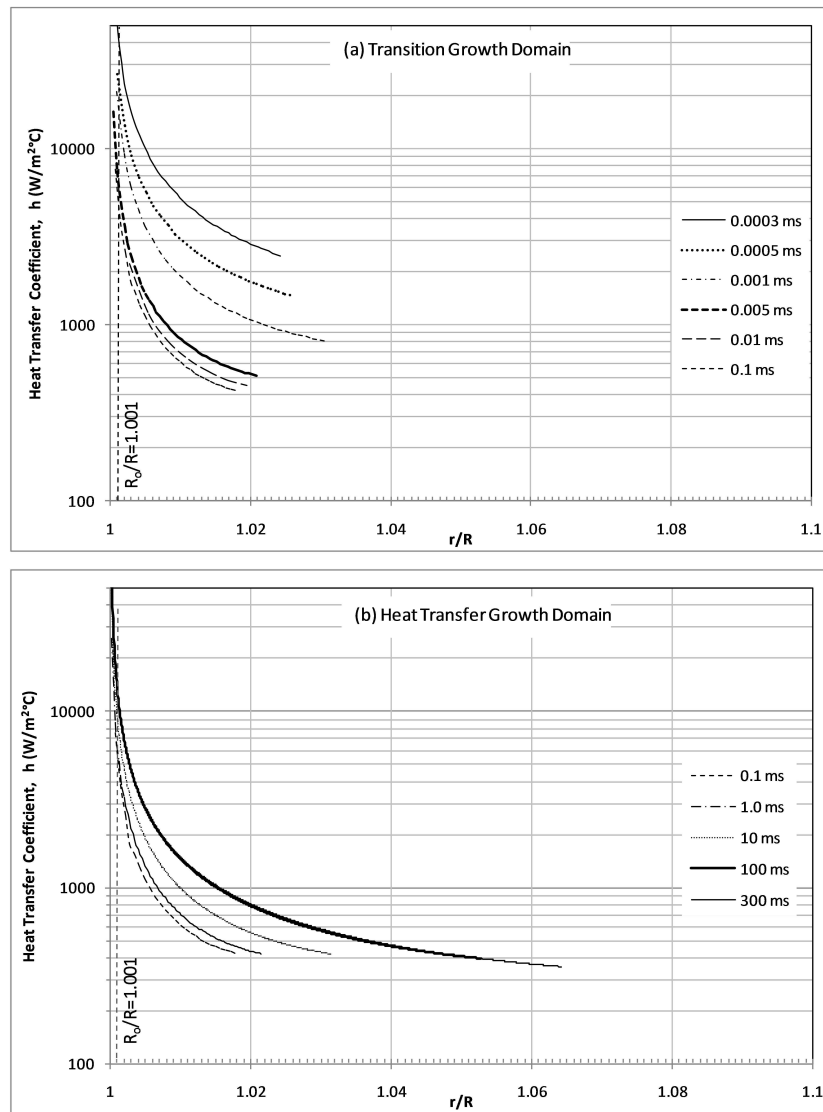
FIG. 8: Heat-transfer coefficient distribution near the triple interface at different times during the bubble growth phase for **(a)** transition domain and **(b)** heat-transfer domain.

increases in magnitude for a fixed level of heat flux. Further, it is also evident that the relative penetration depth, R_{eff}, initially increases and then decreases with time. This is better illustrated in Fig. 9, where R_{eff}/R shows a local maximum that corresponds with the maximum in the interfacial velocity in Fig. 4(b) and confirms the notion that stronger liquid advection is responsible for larger relative penetration depths and heat transfer.

In terms of more qualitative information regarding the heat-transfer coefficient, Fig. 10 illustrates the change of the representative near-field $h(R_o)$, the area averaged h_{avg}, and the far-field conductance with time. In the figure it is clear that both $h(R_o)$ and h_{avg} decrease substantially with time during the *transition domain* for the reasons discussed above. Here h_{avg} decreases from about 8500 W/m^2 °C at 0.0003 ms to 1100 W/m^2 °C at 0.1 ms. Even still, as the bubble passes from the *transition domain* to the *heat-transfer domain*, it is evident from the local minimums observed in Figs. 9 and 10 that a change in the mechanism of heat transfer is occurring. Here, the
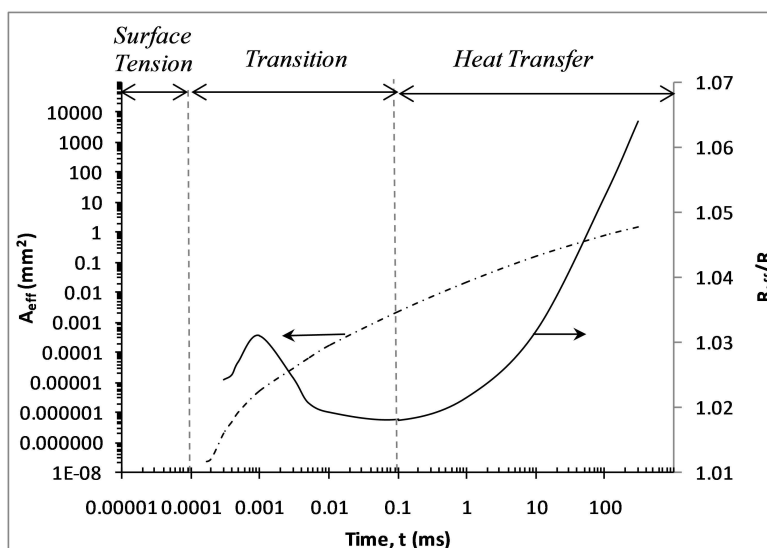
FIG. 9: Effective area and the relative distance of heat-transfer enhancement.
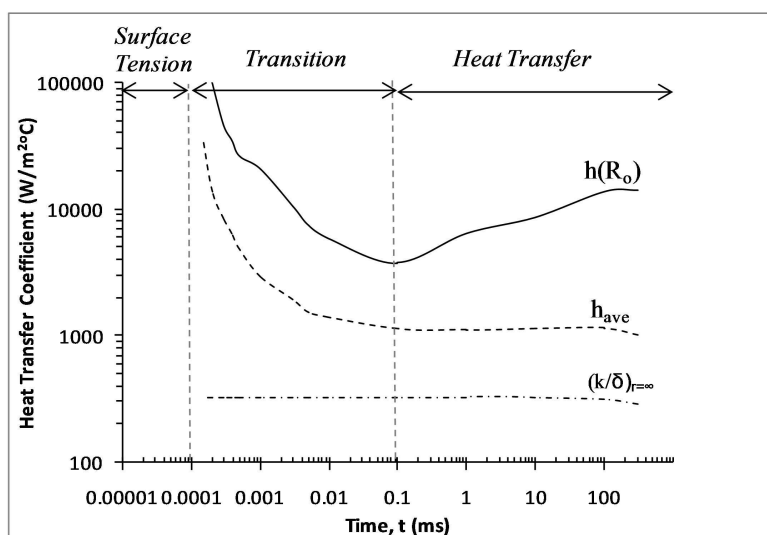
FIG. 10: Representative wall heat-transfer coefficient values near the triple interface, $h(R_o)$, averaged over the effective area of enhancement, h_{avg}, and due to conduction in the far field, $(k/\delta)_{ff}$.

decreasing influence of liquid advection due to the drop in interfacial velocity becomes countered by the fact that the $T_v(t)$ has reduced to an extent that transient conduction becomes an increasingly more important mode of heat transfer.

At the beginning of the *heat-transfer domain* of bubble growth, Fig. 8(b) shows a reversal in the trend observed in the local heat-transfer coefficient of Fig. 8(a)

for the *transition domain*. Here the magnitude of the heat-transfer coefficient increases with time relative to the bubble size. The physical mechanism by which this occurs becomes apparent upon examination of Figs. 5(b) and 5(c). It is evident that the presence of the now large and relatively cold bubble causes the isotherms to bend sharply and cluster themselves around the vapor–liquid interface. This concentrates the isotherms radially around

the bubble, thus establishing the temperature gradient normal to the bubble interface which is responsible for the evaporative heat flux into the bubble. As illustrated qualitatively in Figs. 5(a) and 5(b), the penetration distance from the triple interface where significant deformation of isotherms occurs increases with time due to transient conduction with possible liquid advection influence at the beginning of this growth domain. This is quantified in Fig. 9, where it is observed that the relative penetration depth, R_{eff}/R, begins to increase at the beginning of the heat-transfer domain and continues to do so as time progresses. Since the bubble is much larger, the effective surface area of enhancement, A_{eff}, increases beyond ~ 1.0 mm^2, which is significant. Furthermore, Fig. 10 shows that the magnitude of $h(R_o)$ increases with time, indicating an increase in the intensity of the wall heat transfer in the immediate vicinity of the triple interface as transient conduction takes hold. Even still, the representative area averaged h_{ave} tends to level out within the *heat-transfer domain*, remaining just above $h_{\mathrm{ave}} \approx 1000$ W/m^2 °C. Although Fig. 8(b) indicates that relative to the bubble size the local heat-transfer coefficient tends to increase with time, this is offset by the fact that h_{ave} is determined by area averaging within a radial coordinate system. Thus, as time progresses the proportion of the surface area where $h(r)$ is "low" compared with $h(R_o)$ increases disproportionately with time as the bubble radius and effected radius increase.

4. CONCLUSIONS

A numerical simulation of the hemispherical bubble growth on a heated surface in microgravity has been performed in order to elucidate the mechanism of heat transfer near the moving triple interface. The simulation test case is specific to the transient microgravity test case for the onset of nucleate boiling of STS-60 Run#4 in Lee (1993). For this case study it has been proposed that the enhanced region of heat transfer, due solely to the presence and motion of the triple interface, depends on the bubble growth dynamics. During the *surface tension* controlled growth stage enhancement is negligible, because the nearly stationary and extremely small bubble is contained within a local thermal field that is nearly uniform. In the early stage of the *transition domain* the interfacial bubble velocity increases substantially, causing substantial rates of heat transfer and better penetration along the heated wall due to liquid advection near the triple interface. Furthermore, the increase in the liquid velocity induces a hydrodynamic force on the bubble that restrains

the rate at which the bubble depressurizes. Even still, the reducing influence of liquid advection on the heat transfer near the triple interface is partially offset by an increase in the influence of transient conduction, as the vapor temperature within the bubble decreases as it depressurizes. During the *heat transfer* controlled growth stage the bubble has become sufficiently large and the interface velocity is low enough that transient conduction progressively becomes the dominant mode of heat transfer. Here, the intensity of the heat transfer in the immediate vicinity of the bubble as well as the area along the heated surface over which the influence is important both increase as the bubble grows. However, the representative area averaged heat-transfer coefficient changes very little, remaining at approximately $h_{\mathrm{ave}} \approx 1000$ W/m^2 °C.

ACKNOWLEDGMENTS

REFERENCES

Bai, Q. and Fujita, Y., Numerical simulation of bubble growth in nucleate boiling—Effects of system parameter, *Multiphase Sci. Technol.*, vol. **12**(3–4), pp. 195–214, 2000.

Board, S. J. and Duffy, R. B., Spherical vapour bubble growth in superheated liquids, *Chem. Eng. Sci.*, vol. **26**, pp. 263–274, 1971.

Demiray, F. and Kim, J., Microscale heat transfer measurements during pool boiling of FC-72: Effect of subcooling, *Int. J. Heat Mass Transfer*, vol. **47**, pp. 3257–3268, 2004.

Dhir, V. K., Nucleate and transition boiling heat transfer under pool and external flow conditions, *Int. J. Heat Fluid Flow*, vol. **12**(4), pp. 290–314, 1991.

Dhir, V. K., Mechanistic prediction of nucleate boiling heat transfer–Achievable or a hopeless task?, *J. Heat Transfer*, vol. **128**(1), pp. 1–12, 2006.

Fath, H. S. and Judd, R. L., Influence of system pressure on microlayer evaporation heat transfer, *ASME J. Heat Transfer*, vol. **100**, pp. 49–55, 1978.

Forster, D. E. and Greif, R., Heat transfer to a boiling liquid, Mechanisms and correlation, *ASME J. Heat Transfer*, vol. **81**, pp. 43–53, 1959.

Fuchs, T., Kern, J., and Stephan, P., A transient nucleate boiling model including microscale effects and wall heat transfer, *J. Heat Transfer*, vol. **128**(12), pp. 1257–1265, 2006.

Genske, P. and Stephan, K., Numerical simulation of heat trans-

fer during growth of single vapor bubbles in nucleate boiling, *Int. J. Thermal Sci*., vol. **45**(3), pp. 299–309, 2006.

Golobic, I., Petkovsek, J., Baselj, M., Papez, A., and Kenning, D. B. R., Experimental determination of transient wall temperature distributions close to growing vapor bubbles, *Heat Mass Transfer*, Special Issue, 2007.

Guo, Z. and El-Genk, M. S., Liquid microlayer evaporation during nucleate boiling on the surface of a flat composite wall, *Int. J. Heat Mass Transfer,* vol. **37**(11), pp. 1641–1655, 1994.

Han, C. Y. and Griffith, P., The mechanism of heat transfer in nucleate pool boiling, Part II. The heat flux-temperature difference relation, *Int. J. Heat Mass Transfer*, vol. **8**, pp. 903–914, 1965.

Judd, R. L. and Hwang, K. S., A comprehensive model for nucleaye pool boiling heat transfer including microlayer evaporation, *ASME J. Heat Transfer*, vol. **98**, pp. 623–629, 1976.

Lee, H. S., *Vapour Bubble Dynamics in Microgravity*, PhD, University of Michigan, 1993.

Lee, H. S. and Merte, Jr., H., Hemispherical bubble growth in microgravity: Experiments and model, *Int. J. Heat Mass Transfer*, vol. **39**, pp. 2449–2461, 1996.

Lee, R. C. and Nydahl, J. E., Numerical calculation of bubble growth in nucleate boiling from inception through departure, *J. Heat Transfer*, vol. **111**(2), pp. 474–479, 1989.

Lesage, F. J., Cotton, J. S., and Robinson, A. J., An equation of motion for bubble growth, *ECI Int. Conf. on Boiling Heat Transfer*, Paper BG2, Florianópolis-SC-Brazil, 2009.

Lesage, F., Judd, R. L., and Robinson, A. J., Numerical method for spherical bubble growth in superheated liquids, *Comput. Thermal Sci*., vol. **2**(1), pp. 19–31, 2009.

Liao, J., Mei, R., and Klausner, J. F., The influence of the bulk liquid thermal boundary layer on saturated nucleate boiling, *Int. J. Heat Fluid Flow*, vol. **25**, pp. 196–208, 2004.

Lien, Y. C., Bubble Growth Rates at Reduced Pressure, DSc, Massachusetts Institute of Technology, MIT, 1969.

Mei, R., Chen, W., and Klausner, J. F., Vapor bubble growth in heterogeneous boiling—I. Formulation, *Int. J. Heat Mass Transfer*, vol. **38**(5), pp. 909–919, 1995a.

Mei, R., Chen, W., and Klausner, J. F., Vapor bubble growth in heterogeneous boiling—II. Growth rate and thermal fields, *Int. J. Heat Mass Transfer*, vol. **38**(5), pp. 921–934, 1995b.

Merte, Jr., H., Lee, H. S., and Keller, R. B., Report on pool boiling experiment flown on STS-47-57-60, Report no. UM-MEAM-95-01, Dept. of Mechanical Engineering and Applied Mechanics, The University of Michigan, Ann Arbor, MI, NASA contract 3-25812, 1995.

Mikic, B. B. and Rohsenow, W. M., A new correlation of pool boiling data including the effect of heating surface characteristics, *Int. J. Heat Mass Transfer*, vol. **9**, pp. 245–250, 1969.

Moore, F. D. and Mesler, R. B., The measurement of rapid surface temperature fluctuations during nucleate pool boiling of water, *AIChE J*., vol. **7**, pp. 620–624, 1961.

Mukherjee, A. and Kandlikar, S. G., Numerical study of single bubbles with dynamic contact angle during nucleate pool boiling, *Int. J. Heat Mass Transfer*, vol. **50**(1–2), pp. 127–138, 2007.

Robinson, A. J. and Judd, R. L., Bubble growth in a uniform and spatially distributed temperature field, *Int. J. Heat Mass Transfer*, vol. **44**, pp. 2699–2710, 2001.

Robinson, A. J., *Bubble Growth Dynamics in Boiling*, PhD, McMaster University, 2002.

Robinson, A. J. and Judd, R. L., The dynamics of spherical bubble growth, *Int. J. Heat Mass Transfer*, vol. **47**(23), pp. 5101–5113, 2004.

Robinson, A. J., Heat transfer near the contact line during boiling in microgravity, *Microgravity Sci. Technol*., vol. **XIX**(3–4), pp. 139–140, 2007.

Snyder, N. R. and Edwards, D. K., Summary of conference on bubble dynamics and boiling heat transfer, Memo 20-137, Jet Propulsion Laboratory, Pasadena, CA, pp. 14–15, 1956.

Son, G., Dhir, V. K., and Ramanujapu, N., Dynamics and heat transfer associated with a single bubble during nucleate boiling on a horizontal surface, *J. Heat Trans.,* vol. **121**(3), pp. 623–631, 1999.

Stephan, P. and Fuchs, T., Local heat flow and temperature fluctuations in wall and fluid in nucleate boiling systems, *Heat Mass Transfer*, DOI:10.1007/s00231-007-0320-1, 2007.

van Stralen, J. D., Sohal, M. S., Cole, R., and Sluyter, W. M., Bubble growth rates in pure and binary systems: Combined effect of relaxation and evaporating microlayers, *Int. J. Heat Mass Transfer*, vol. **18**, pp. 453–467, 1975.

Welch, S. W. J., Direct simulation of vapor bubble growth, *Int. J. Heat Mass Transfer,* vol. **41**(12), 1655–1666, 1998.

Wagner, E., Sodtke, C., Schweizer, N., and Stephan, P., Experimental study of nucleate boiling heat transfer under low gravity conditions using TLCs for high resolution temperature measurements, *Heat Mass Transfer*, vol. **42**, pp. 875–883, 2006.

Wu, J., Dhir, V. K., and Qian, J., Numerical simulation of subcooled nucleate boiling by coupling level-set method with moving-mesh method, *Numer. Heat Transfer, Part B*, vol. **51**(6), pp. 535–563, 2007.

Yoon, H. Y., Koshizuka, S., and Oka, Y., Direct calculation of bubble growth, departure, and rise in nucleate pool boiling, *Int. J. Multiphase Flow*, vol. **27**, pp. 277–298, 2001.

Zhao, Y. H., Masuoka, T., and Tsuruta, T., Unified theoretical prediction of fully developed nucleate boiling and critical heat flux based on a dynamic microlayer model, *Int. J. Heat Mass Transfer*, vol. **45**, pp. 3189–3197, 2002.

THERMAL-FLUID MODELING OF A VISI-COOLER

S. Joseph Sekhar,[1,*] B. Raja,[2] & D. Mohan Lal[3]

[1]*St. Xavier's Catholic College of Engineering, Chunkankadai, Nagercoil 629 807, Tamil Nadu, India*

[2]*Indian Institute of Information Technology, Design, and Manufacturing (IIITD&M)–Kancheepuram, Indian Institute of Technology-Madras, Chennai 600 036, Tamil Nadu, India*

[3]*Refrigeration and Air-Conditioning Division, Department of Mechanical Engineering, College of Engineering, Anna University, Chennai 600 025, Tamil Nadu, India*

*Address all correspondence to S. Joseph Sekhar E-mail: josephsekhar@hotmail.com

The steady state thermofluid behavior of a visi-cooler has been mathematically modeled using a distributed parameter technique for R-12 and R-134a/R-290/R-600a mixtures. The pressure drop in condenser and evaporator tubes, pressure-volume diagram, temperature glide, compressor power, and per day energy consumption for various operating conditions have been extracted. Experiments also have been conducted for both the refrigerants for similar operating conditions. The simulation revealed that a mixture of R-134a, R-290, and R-600a with mass percentage of 91%, 4.068%, and 4.932%, respectively, is more efficient than R-12 in all performance aspects. The deviation of experimental results from the simulated values is observed to be within ±12%. The experiments also showed that the percentage reduction in the per day energy consumption with the mixture is between 10.8% and 19.6% for the tested conditions.

KEY WORDS: *distributed parameter modeling, two-phase heat transfer coefficient, hermetic compressor*

1. INTRODUCTION

Ever since Molina and Rowland (1974), which led to the Montreal Protocol (United Nations Environment Programme, 1989), proved the adverse effect of chlorofluoro-carbons (CFCs) on the ozone layer, the search for alternatives to R-12 became a pressing need among the research community in the refrigeration sector. The Protocol had urged both the developed and developing countries to show intense curiosity with a sense of participation to find definitive ways to mitigate the impact of ozone depletion posed by the CFCs on Earth. Subsequent meetings held in many countries called for a gently declining asymptotic production of CFCs. Even as scientists subscribed to a number of alternatives to the R-12 refrigerants, the effort to find the best alternative is still ongoing. Spauschus (1988), Hambraeus (1991), and many others have recommended R-134a as a prominent substitute for R-12. However, Jung and Radermacher (1991) and Carpenter (1992)

revealed that the Coefficient of Performance (COP) of R-134a, retrofitted in an existing R-12 system, was 15% lower than that of the actual R-12 system. Furthermore, Devotta and Gopichand (1992) had reported that due to higher polarity of R-134a, the solubility with nonpolar mineral oil, which is the compressor lubricant, was poor and led to accumulation of oil in the evaporator. After a prolonged run, the compressor would be starving for oil, which is required for lubrication. Jung et al. (1996), Colbourne (2000), and Granryd (2001) recommended hydrocarbons as prominent substitutes for R-12. Furthermore, hydrocarbons are miscible with mineral oil, which is a propitious factor opting those as suitable retrofit alternatives, but their flammable nature caused severe concern. Moreover, many countries had posted restrictions on the permissible quantity of hydrocarbons in domestic appliances. Therefore, against the backdrop of rising problems caused by ozone depletion, it was prudent to devise a retrofit substance that could circumvent all the preceding

NOMENCLATURE

A	area (m^2)		η	efficiency
A_1, B_1	constants		ν	specific volume ($m^3\ kg^{-1}$)
C	coefficient		ρ	density ($kg\ m^{-3}$)
D	diameter (m)		**Subscripts**	
f	friction factor		amb	ambient
G	mass flux ($kg\ m^{-2}\ s^{-1}$)		c	compressor
h	specific enthalpy ($J\ kg^{-1}$)		con	contraction
k	thermal conductivity ($W\ m^{-1}\ K^{-1}$)		cr	critical
L	length (m)		cyl	cylinder
$\dot{m}$	mass flow rate ($kg\ s^{-1}$)		d	discharge
Nu	Nusselt number		el	electrical
P	pressure (kPa)		f	liquid phase
Pr	Prandtl number		fg	liquid vapor mixture
Q	heat (J)		flash	flash point
Re	Reynolds number		is	isentropic
t	time (s)		i	inlet
T	temperature (°C)		iv	inlet vapor
u	velocity ($m\ s^{-1}$)		init	initial
V	volume (m^3)		l	liquid
W	work (W)		me	mechanical
x	refrigerant quality		o	outlet
X_{tt}	Martinelli parameter		ref	refrigerant side
Z	compressibility factor		s	suction
Greek Symbols			sh	shell
μ	dynamic viscosity (Pa s)		sp	single phase
ω	angular velocity ($rad\ s^{-1}$)		swept	swept volume
α	convective heat transfer coefficient ($W\ m^{-2}K^{-1}$)		V	valve
			v	vapor

issues. Janssen and Engels (1995) had reported that the oil miscibility and oil return to the compressor casing in the existing R-12 system was possible by an addition of hydrocarbon to R-134a. On the basis of this, Sekhar et al. (2004a, 2004b) experimented with real-time R-12 appliances using different mixtures of R-134a, R-290, and R-600a. It was reported that a zeotropic mixture, termed M09 (R-134a/R-290/R-600a: 91/4.068/4.932% by mass) worked with enhanced performance in an existing R-12 system that which had mineral oil as a compressor lubricant. The authors also recommended the mixture to be a drop-in substitute for R-12.

Chi and Didion (1982) modeled the components of a vapor compression system as lumped bodies and ana-

lyzed the transient behavior of a heat pump. Owing to the complexities involved in modeling the two-phase flow in evaporator and condenser, the model failed to predict results close to experimental ones. William and Thompson (1988) analytically modeled a hermetically sealed compressor of a refrigerator into three sections, namely, top, sides, and bottom. Suitable correlations for convective heat transfer coefficient were used to capture the heat transfer interaction with the ambient. The results obtained from the computer program were closer to the experimental values. However, the heat transfer in suction, discharge plenum, and the compression process were not included in the simulation. Jung and Radermacher (1991) simulated the single evaporator refrigerator to compare

the performance of pure and zeotropic mixtures. Constant refrigeration effect for all the refrigerants, isentropic efficiency of 0.55 to compressor, and logarithmic mean temperature difference (LMTD) method for all the heat exchangers were considered in the preceding model. With the Newton-Raphson method, the results proved the evaporator performance of R-134a to be 7%–30% less than R-12. Wang and Touber (1991) recommended a distributed parameter model for large-duration simulation and coupled a steady state refrigeration machine with a dynamic refrigerated room model. Many processes are characterized by state variables evolving not only in time but also in space. The description of such processes, called distributed parameter systems, requires the use of partial differential equations. A distributed parameter technique is accurate because it directly accounts for the internal physics of the devices. The continuity, momentum, and energy equations throughout the components, such as the heat exchanger, are numerically solved. The outputs from the model contain details like the refrigerant temperatures, pressures, and vapor qualities. Hence, because of the increased accuracy and reduced dependence on empirical data, this method has been used to model all the components used in this work. Zhi and Wei (1991) had simulated a small-scale refrigerator with tube-coil evaporator and tube-coil condenser using a lumped parameter model and predicted that the experimental results would be close to simulated ones. Domanski and McLinden (1992) developed a simulation program (CYCLE 11) to evaluate the performance of refrigerant and refrigerant mixtures. The heat exchangers were modeled using effective temperature difference and pressure drop. For the zeotropic mixture, the heat exchanger area was divided into a number of small sections, and LMTD was applied to every section. A polytropic compression efficiency of 85% was fixed, and for different volumetric efficiencies, the performance was comparable with the experimental results. Geoffrey and Chen (1994) introduced the pinch method to facilitate the refrigerant cycle simulation for zeotropic refrigerants and proved that the COP of the R-22 system was increased from 3.5 to 4.5 for a condenser pinch of 6.5°C, and the power savings was 35%. However, for a pinch of 10°C, the COP was increased to 3.77, with power savings of 22%, for a binary mixture (R-22/R-142b). Chung et al. (1996) developed a one-dimensional model to evaluate the heat transfer and pressure drop characteristics of zeotropic refrigerants such as R-134a/R-32 and observed that the liquid near the fully evaporated state of the zeotropic refrigerant required a correspondingly higher temperature than that of the less volatile compo-

nent. The nonlinear properties of the zeotropic mixtures were found to play a major role in heat and momentum transfer. John and Radermacher (1997) developed a heat exchanger model and reported that the refrigerant-side heat transfer depended on the accuracy of the air-side heat transfer coefficient. Since the air-side heat transfer resistance was larger than the refrigerant-side heat transfer resistance, the inaccuracy of the heat transfer coefficient in the refrigerant-side had not significantly affected the overall heat transfer coefficient. A 20% decrease in the evaporation heat transfer coefficient resulted in a 2.7% decrease in the overall heat transfer coefficient. Metin and Nilufer (2002) tested the performance of exchangers having different geometries under dry conditions. The heat transfer coefficient's dependency on the heat exchanger geometry and Reynolds number has been proved.

However, an appropriate mathematical simulation for the entire refrigeration system is not discussed in existing studies to validate the use of zeotropic refrigerant in medium-temperature refrigeration systems such as the visi-cooler, which is mainly used for vending cool drinks. In this article, a generalized thermal-fluid model that was used to simulate a vapor compression appliance to finalize the refrigerant mixture is refined and presented.

2. DESCRIPTION OF THE PRESENT SIMULATION MODEL

The components of a visi-cooler such as a hermetically sealed compressor, air-cooled condenser, capillary tube, and evaporator, were modeled individually, and their governing equations were coupled to evolve the total system model. The thermophysical properties are extracted from REFPROP, a National Institute of Standards and Technology thermo physical property database (McLinden et al., 1998). The basic components and their respective upstream and downstream interactions are shown in Fig. 1.

2.1 Compressor

The distributed parameter modeling was used for a compressor with constant angular velocity of the crank shaft and assumed polytropic efficiency. Furthermore, the heat transfer to the oil and pressure drops in the compressor shell and the discharge tubes were assumed to be negligible. Equation (1) (William and Thompson, 1988) governs the instantaneous swept volume of the compressor. Considering the valve as an orifice and flow as isentropic, the mass flow rate ($\dot{m}_s$) through the suction or discharge valve was calculated from Eq. (2). Equations (3) and (4)
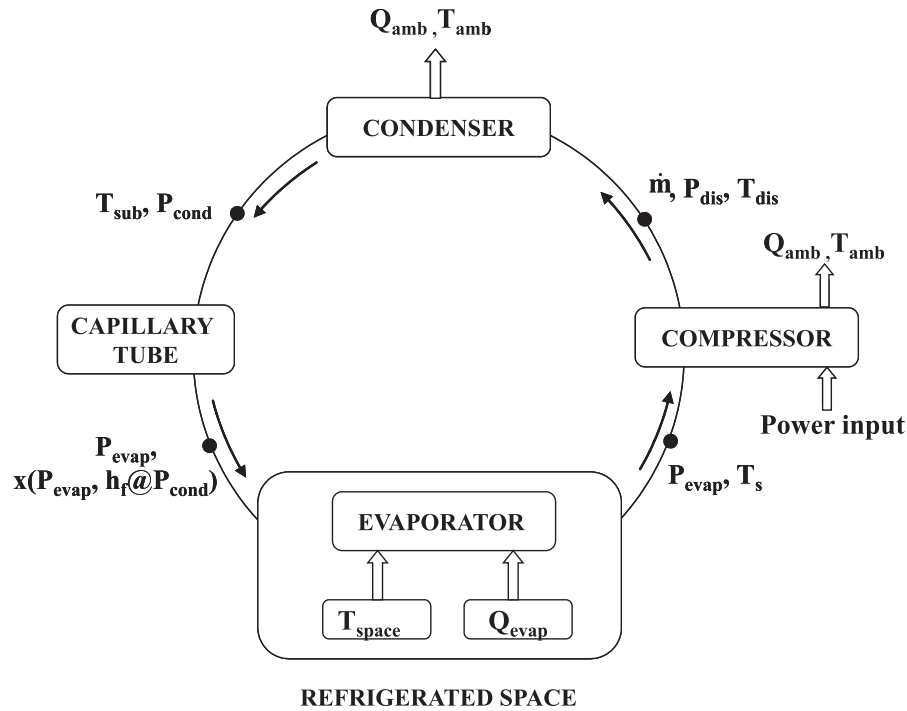
FIG. 1: Schematic of the distributed model

govern the pressure drop in the values and the energy in the swept volume:

$$V(t) = V_{\text{cyl}} + \frac{\pi D_{\text{cyl}}^2}{8} L_{\text{swept}} \left[1 - \cos\left(\omega t\right)\right] \quad (1)$$

$$\dot{m}_s = \rho_{iv} Z C_d A_{cr} u_{is} \quad (2)$$

$$\Delta P_V = C_V \frac{u^2}{2} \quad (3)$$

$$\dot{m}_o h_o = Q_c + \frac{dW}{dt} + \dot{m}_i h_i - \Delta P_V \quad (4)$$

The overall heat transfer coefficient inside the compressor swept volume, outside the compressor shell (α_o), and inside the compressor shell (α_i) was calculated as per the correlations used by Padhy (1992). The refrigerant mixture is assumed to experience negligible change in the concentration. With negligible kinetic and potential energies, the energy balance equation of the entire compressor with the airflow over it is derived as follows:

$$\dot{m}_o h_o = \dot{m}_i h_i + Q_{sh} \quad (5)$$

$$Q_{sh} = Q_{me} + Q_{el} + Q_{\text{amb}} + Q_c + Q_d \quad (6)$$

2.2 Condenser and Evaporator

The condenser and evaporator used in the visi-cooler were plate-finned-type heat exchangers. The components were modeled using a one-dimensional equation of mass, momentum, and energy, and the overall heat transfer coefficient was calculated for negligible fouling resistance (Incropera and DeWitt, 1996). The evaporator and condenser were divided into two-phase and superheated regions. In evaporator and condenser, the single-phase convective heat transfer coefficients in the refrigerant side were calculated from the Dittus-Boelter correlation (Perry and Chilton, 1984). In the two-phase region, forced convection heat transfer coefficients were obtained from the following correlation (Traviss et al., 1973):

For $F_1 < 1$:

$$\frac{h_{\text{ref}} D_i}{k_{r,l}} = \text{Pr}_l \text{Re}_l^{0.9} \left(\frac{F_1}{F_2}\right) \quad (7)$$

For $1 \leq F_1 \leq 15$:

$$\frac{h_{\text{ref}} D_i}{k_{r,l}} = \text{Pr}_l \text{Re}_l^{0.9} \left(\frac{F_1^{1.15}}{F_2}\right) \quad (8)$$

$$F_1 = 0.15 \left(\frac{1}{X_{tt}} + 2.88 X_{tt}^{-0.476} \right) \qquad (9)$$

where

$$X_{tt} = \left(\frac{\mu_l}{\mu_v} \right)^{0.1} \left(\frac{\rho_v}{\rho_l} \right)^{0.5} \left(\frac{1-X}{X} \right)^{0.9} \qquad (10)$$

For $\mathrm{Re} < 50$:

$$F_2 = 0.707 \, \mathrm{Pr} \, \mathrm{Re}^{0.5} \qquad (11)$$

For $50 \le \mathrm{Re} \le 1125$:

$$F_2 = 5 \, \mathrm{Pr} + 5 \ln \left[1 + \mathrm{Pr} \, (0.09636 \mathrm{Re} - 1) \right] \qquad (12)$$

For $\mathrm{Re} > 1125$:

$$F_2 = 5 \, \mathrm{Pr} + 5 \ln (1 + \mathrm{Pr}) + 2.5 \ln \left[0.00313 \mathrm{Re}^{0.812} \right] \qquad (13)$$

The air-side convective heat transfer coefficient for a plate-finned heat exchanger was calculated using appropriate correlation (Manglik and Bergles, 1995). In the two-phase region, the convective heat transfer coefficient was also calculated from correlations available in the literature (Wattelet et al., 1994; Cooper, 1984; Chang et al., 2000).

2.3 Capillary Tube

In the capillary tube, the pressure drop is caused by momentum loss, friction, and gravitational effects. With negligible gravitational effects, the pressure drop due to sudden contraction (entrance correction) was calculated using Eq. (14) (Chung, 1998). The capillary was divided into a single-phase zone and a two-phase zone. The capillary length in the single-phase region is defined as Eq. (15) (Bansal and Rupasinghe, 1998). The P_{flash} is the pressure at which the two-phase region starts. The single-phase friction factor f_{sp} was calculated using Eq. (16):

$$P_i - P_{\mathrm{init}} = \frac{G^2 v_f}{2} \left\{ \left(\frac{1}{C_{\mathrm{con}}} - 1 \right) + \left(1 + \frac{A^2}{A_1^2} \right) \right. $$
$$\left. \times \left[1 + \frac{V_{fg}}{v_f} \times x \right] \right\} \qquad (14)$$

$$L_{sp} = \frac{1}{2} \frac{D\rho}{fG^2} (P_{\mathrm{init}} - P_{\mathrm{flash}}) \qquad (15)$$

$$f_{sp} = 8 \left[\left(\frac{8}{\mathrm{Re}} \right)^{12} + \frac{1}{(A_1 + B_1)^{\frac{3}{2}}} \right]^{\frac{1}{12}} \qquad (16)$$

where

$$A_1 = \left\{ 2.457 \ln \left[\frac{1}{\left(\frac{7}{\mathrm{Re}} \right)^{0.9} + 0.27\varepsilon} \right] \right\}^{16}$$

$$B_1 = \left(\frac{37530}{\mathrm{Re}} \right)^{16}$$

The two-phase region was modeled using Fanno line expansion relations (Stoecker and Jones, 1983). The total pressure drop, outlet quality, and outlet pressure of the capillary tube were calculated.

2.4 Overall System Simulation

The system shown in Fig. 1 has been simulated by coupling the governing equations of individual components. An initial guess of pressure, also called the system's equalization pressure, was assumed to be prevailing in both evaporator and condenser. The mass flow rate of refrigerant, discharge temperature, pressure, and work required for the compression were calculated by compressor subroutine. The output was then fed as input to the condenser subroutine, in which the quality of the refrigerant at the outlet, degree of subcooling, and condenser duty were estimated. The condenser results were fed into the capillary subroutine to estimate the evaporator pressure and the quality of the refrigerant at the capillary outlet. Finally, the evaporator subroutine was used to find the evaporator duty and the degree of superheat. A convergence was assumed if the calculated values were close to the initial assumptions with a criterion of 10^{-3} kg/s for mass flow rate and 10^{-6} J for energy. The entire program, which is a compilation of many subroutines, took as many as 25–35 iterations for the solution to converge. The new values had to be assigned judiciously taken for the compressor inlet condition, and the analysis was repeated. It is to be noted that the program will make appropriate reference to property subroutines as and when required. Following are the major assumptions considered in this modeling: (1) the property variation in all the components is one-dimensional; (2) the mass flow rate and ambient temperature are constant and steady; (3) the pressure drop is negligible in condenser and evaporator; (4) fouling resistance is negligible in the heat exchangers; (5) the thermophysical properties are taken from REFPROP (McLinden et al., 1998); (6) no fluctuation in the angular speed; (7) polytropic compression and electrical motor efficiency is 85%; and (8) negligible oil accumulation in evaporator and condenser.

3. TEST FACILITY

The experimental setup used for this study is schematically shown in Fig. 2. The basic circuit of the visi-cooler was modified to accommodate the measuring instruments. To measure the temperature, resistance temperature detectors (RTD) temperature sensors (PT100) with ±0.15°C accuracy were placed across all the basic components. Since capillary tube optimization was required, four capillaries having 0.86 mm diameter and length 2.13 m, 2.44 m, 2.74 m, and 3.05 m were suitably fixed. A sight glass was provided in the liquid line to check the condition of the refrigerant entering into the capillary. Pressure gauges with ±0.5% accuracy were fixed across the condenser, evaporator, and capillary. To measure the temperature of the refrigerated space, four RTDs were placed at different locations suitably and connected to a data logger. The compressor was connected with a watt meter (±1 W accuracy) and energy meter (±0.25% accuracy) to measure the energy consumption.

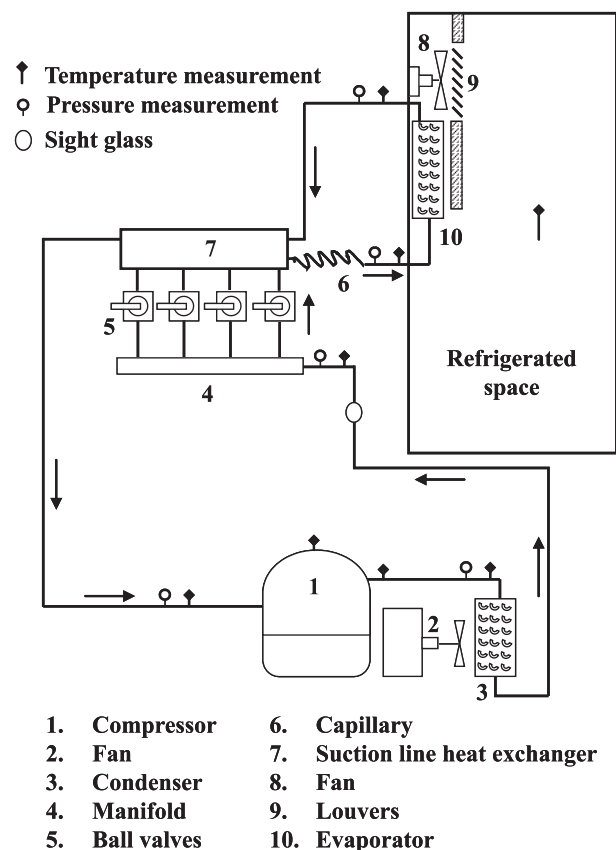|			
1.	Compressor	6.	Capillary
2.	Fan	7.	Suction line heat exchanger
3.	Condenser	8.	Fan
4.	Manifold	9.	Louvers
5.	Ball valves	10.	Evaporator

FIG. 2: Schematic of the visi-cooler test bench

To conduct tests at various ambient conditions, the whole setup was kept inside a temperature-controlled room. Since the refrigerant circuit of the visi-cooler has to be modified to fix measuring instruments, the quantity of charge specified by the manufacturer (300 g) may not be sufficient, and hence charge optimization will be needed. To optimize the charge, the system was charged with 250–350 g of R-12 in steps of 10 g, and the energy consumption test was conducted for 32°C ambient temperature and with a thermostat setting of 1°C cutoff and 4°C cut-in temperatures. The standard capillary (2.44 m) was used for the study. The per day energy consumption with respect to charge quantity was observed, and it was found that the energy consumption per day was minimum for a 300 g charge. The obtained quantity of R-12 was taken as the reference to arrive at the equivalent quantity of mixtures as discussed by Sekhar et al. (2004b). The thermostat inside the refrigerated space was adjusted to 1°C cutoff and 4°C cut-in. The performance details are experimentally measured based on a per day energy consumption test for different ambient temperatures 22°C, 26°C, 32°C, 36°C, and 43°C. A pull-down test was also performed, for which we used the temperature, energy, and power consumption from a watt meter, and the refrigerated space temperature was recorded in a data logger for an interval of 15 s to calculate the COP; the readings were logged until the average space temperature reached 1°C. The experiments were first conducted for R-12, followed by the refrigerant mixtures, and the testing conditions are shown in Table 1.

4. RESULTS AND DISCUSSION

The experiments were conducted for R-12, M07, M09, and M11 for different charge, ambient temperature, and capillary length. A sample experimental result of pressure drop, power consumption, and so on, is shown in Table 2. The results obtained from the experimental and simulated studies are compared for the all the tested conditions, and selected results are discussed in this section. The simulated $P - V$ diagram of the compressor during the compression process of different refrigerants at 32°C ambient and 1°C refrigerated cabin temperatures is plotted in Fig. 3, which shows that the compression ratio for M09 and R-12 is 6.65 and 6.9, respectively. The x-axis consists of percentage swept volumes as the compression and expansion process takes place (total swept volume is 0.758×10^{-5} m³). From the calculation, it is found that M09 has nearly 1% higher compression work than R-12. Even though the operating pressures of M09 are 10%–

TABLE 1: Testing conditions

Parameters	Values
Refrigerants	R-12, M07 (R-134a: hydrocarbon (HC) blend: 93%: 7% by mass) M09 (91%: 9 %) and M11 (89%: 11%)
Capillary length to check optimum charge quantity	2.13, 2.44, 2.74, and 3.05 with 0.86 mm inner diameter
Ambient temperature	22°C, 26°C, 32°C, 36°C, and 43°C

TABLE 2: Experimental data of the refrigerants for a tested condition.

Refrigerant	R-12	M09	M11	R-12	M09	M11
Capillary length (m)	2.44	2.44	2.44	2.44	2.44	2.44
T_{amb} (°C)	26	26	26	32	32	32
Temperature at typical points inside refrigerated space (°C)						
1	1.0	1.0	1.0	1.1	1.1	1.0
2	1.2	1.1	0.9	1.0	1.2	1.1
3	0.9	1.0	1.1	0.9	0.9	1.0
4	1.0	0.9	1.1	1.1	0.9	1.0
Temperature at some specific points (°C)						
Evap. inlet	−14.0	−18	−18.4	−13.2	−17.0	−17.4
Evap. outlet	−12.2	−13.4	−13.5	−10.8	−11.2	−11.5
Comp. inlet	18.5	16.2	16.2	21.0	18.2	18.4
Comp. outlet	75.5	68.5	71.0	83.0	76.0	80.0
Cond. outlet	40.2	38.0	38.4	44.0	42.0	42.5
Capill. inlet	36.6	35.2	35.6	40.0	38.0	38.6
Comp. dome 1	63.0	60.4	61.5	67.0	63.5	65.4
Comp. dome 2	63.5	60.0	60.5	66.8	63.6	64.8
Pressure at some specific points (kPa)						
Evap. inlet	107	118	120	110	124	126
Evap. outlet	95	110	114	103	118	120
Cond. inlet	1180	1300	1305	1223	1358	1356
Cond. outlet	1170	1285	1295	1210	1342	1344
Comp. inlet	94	108	112	100	116	118
Comp. power (W)	286	290	298	310	314	325
Energy consumption (kWh/d)	3.92	3.36	3.58	5.1	4.25	4.54

20% higher than for R-12, because of its reduced density and viscosity, the compression work shoots up by 1% only. During the compression cycle, the maximum temperature reached in the compressor for M09 and M11 is 142°C and 147°C, respectively, while it is 187°C for R-12, which is also for the reason for higher COP of the system with M09.

The simulated pressure drop along the length of the capillary is plotted in Fig. 4, which shows that even though the inlet pressure is high (16.5 bar) as compared to R-12 (14.2 bar), the required pressure drop was obtained with the existing capillary length itself. It is to be noted that the density and viscosity of M09 and M11 are less than those of R-12, and hence the pressure drop should be less than that of R-12. However, the simulation study revealed that the mixtures M09 and M11 have a higher dryness fraction at the exit of the capillary, which forces one to think that the refrigeration capacity of M09 will be lower than that of R-12. But even though the dryness fraction is more for mixtures, because of their high latent heat of vaporization, the mixtures have higher refrigeration capacity than R-12.
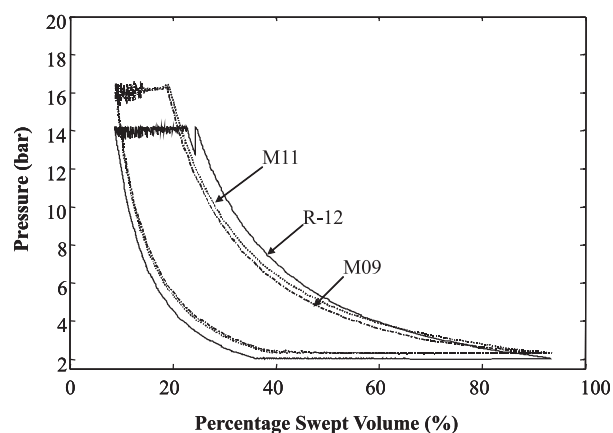
FIG. 3: $P - V$ diagram of the compression process at $32°C$ ambient and $1°C$ cabin temperatures
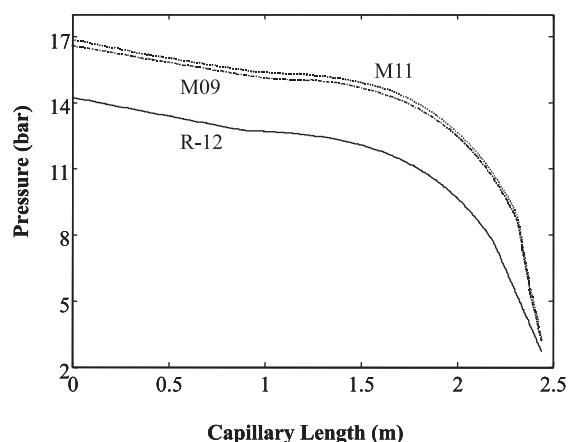

FIG. 4: Pressure drop along the length of the capillary tube at $32°C$ ambient and $1°C$ cabin temperatures

The variations of temperature along the evaporator and condenser coils obtained from the simulation study are plotted in Figs. 5 and 6, respectively. In the case of both mixtures, the boiling and condensation processes are non-isothermal, which is due to the zeotropic nature of the mixture. The length required for complete vaporization of the mixtures is almost 20% less than for R-12, which indicates that the mixtures possess higher heat transfer co-efficients. This is a reason in the evaporator for the super-heating of M09 and M11 to start earlier by 0.25 m than in R-12. In the condenser, it is seen that the degree of sub-

cooling is $4°C$ for R-12 and $3°C$ for M09. The preced-ing observations with respect to heat transfer character-istics indicate that the existing evaporator and condenser are sufficient to operate the system with the new mixture.

The experimental results obtained from the per day energy consumption test are tabulated in Table 3. When compared to R-12, the M09 has 10.8%–17.3% and 13%–9.6% less energy consumption at $22°C$ and $43°C$ ambi-ent temperatures, respectively. This is not only due to the better heat transfer characteristics and heat transfer co-efficient of the mixture, as discussed earlier, but also to

TABLE 3: Per day energy consumption of refrigerants

| Thermostat Settings	Refrigerant	Per day energy consumption (kWh/d)				
		22°C	26°C	32°C	36°C	43°C
Cut-in = 0°C, cutoff = 3°C	R-12	3.26	4.1	5.18	5.8	7.12
	M09	2.91	3.57	4.51	5.03	6.2
	M11	3.03	3.76	4.72	5.22	6.52
Cut-in = 1°C, cutoff = 4°C	R-12	3.23	3.92	5.04	5.77	7.07
	M09	2.83	3.35	4.25	4.84	6.04
	M11	3.04	3.54	4.54	5.18	6.46
Cut-in = 2°C, cutoff = 5°C	R-12	3.08	3.76	4.73	5.32	6.76
	M09	2.62	3.21	3.99	4.58	5.64
	M11	2.9	3.58	4.29	4.78	5.97
Cut-in = 3°C, cutoff = 6°C	R-12	2.83	3.49	4.4	5.0	6.38
	M09	2.38	2.84	3.62	4.19	5.24
	M11	2.56	3.12	4.07	4.69	6.0
Cut-in = 4°C, cutoff = 7°C	R-12	2.76	3.43	4.25	4.87	6.12
	M09	2.28	2.77	3.57	4.02	4.92
	M11	2.6	3.13	3.84	4.37	5.51
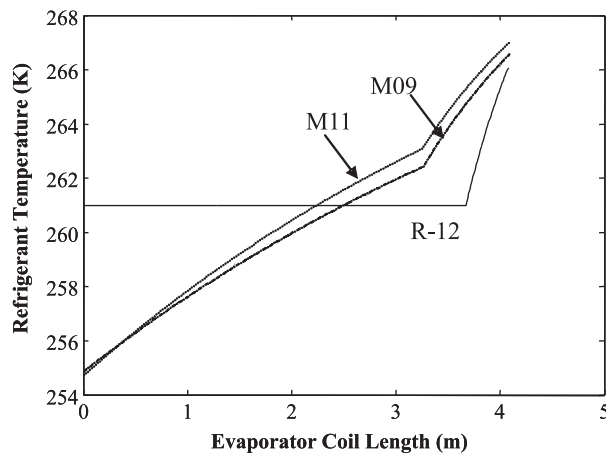
FIG. 5: Temperature distribution along the length of the evaporator coil at 32°C ambient and 1°C cabin temperatures
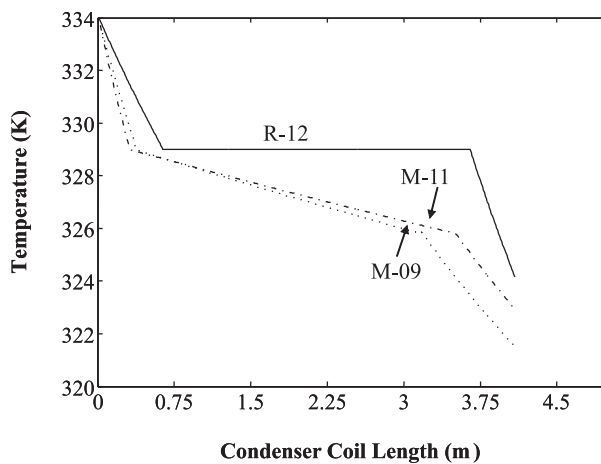

FIG. 6: Temperature distribution along the length of the condenser at 2°C ambient and 1°C cabin temperatures

a lower compression ratio exhibited in the $P - V$ diagram. Furthermore, even though M11 has a pressure ratio closer to R-12, the energy consumption is still better than R-12, which is due to the presence of hydrocarbon in the mixture. Jung et al. (1989a, 1989b) reported that under fully suppressed nucleate boiling conditions, the heat transfer coefficient of two different fluids could be directly rated based on the liquid property group ($\Phi = (c_{pL}/\mu_L)^{0.4} k_L^{0.6}$). This property group was evolved by regrouping the thermophysical property in the Dittus-Boelter heat transfer correlation. The prop-

erty groups of R-12 and M09 are between 166–144 and 236–200, respectively, for the pressures between 1 and 5 bar. Therefore the property group of M09 is higher than R-12 by 30%–50%, which is the reason for better heat transfer characteristics of M09. Even though 30%–50% of increased heat transfer can be expected in M09 theoretically, the actual increase with reference to the lesser length required vaporization is around 15%, and this is due to the preferential boiling and mass transfer resistance present in the mixture. The heat transfer coefficient of a refrigerant mixture degrades from the concentration-averaged values of its individual component, called degradation of the heat transfer coefficient. During the boiling process of mixtures, the more volatile component (MVC), which is R-290, is stripped out first from the fluid stream. Hence the vapor at the initial stage is rich in MVC, and the liquid is rich in the low volatile component (LVC), which is R-600a. Thus the concentration of the LVC in the liquid is higher than at the vapor-liquid interface, and the concentration of the MVC at the vapor-liquid interface is lower than in the vapor phase. Hence the MVC has to diffuse from the bulk liquid to the interface and then to the bulk vapor phase, which results in an increase in mass transfer resistance. This resistance increases when the composition difference of MVC is large between the liquid and vapor. This mass transfer resistance is one of the reasons for the degradation of the heat transfer coefficients. Furthermore, the temperature glide in mixtures affects the heat transfer process as a result of the temperature variation (equilibrium temperature) with the depletion of liquid even if the pressure is constant. In mixtures, because of the temperature glide, the wall superheat decreases as the vapor quality increases. Therefore the influence of the nucleate boiling component, which depends on wall superheat, also decreases due to the temperature glide. Therefore, even though R-134a has better heat transfer characteristics than R-12, the presence of the preceding phenomena reduces the enhancement in heat transfer that can be achieved with pure R-134a.

The compressor power with respect to time during pull-down test is plotted in Fig. 7. From the simulation studies, it is found that M09 is superior among the all the mixtures, and hence it is taken for experimental comparison with R-12. The figure shows that the compressor consumes 2%–4% higher power for M09 as compared to R-12. But for the same thermostat settings, the pull-down time for M09 is only 39 min, whereas it is 49 min in the case of R-12. From the power consumption test, it is observed that the total energy consumed during pull-down is 0.214 kWh for M09, whereas it is 0.255 kWh for R-
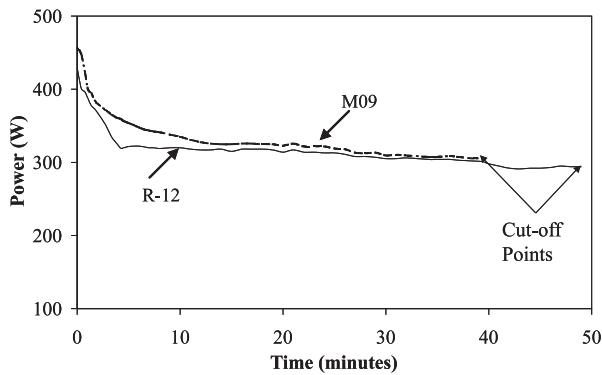
FIG. 7: Variation of compressor power with time during pull-down at 32°C ambient and 1°C cutoff temperatures

FIG. 9: Variation of experimental and predicted COP with ambient temperature at 1°C cabin temperature

12. The compressor work obtained from simulation and experimental study is plotted in Fig. 8. The deviation of predicted values from the experimental results is less than 12%, which proves the validity of the simulation model. The curves also show that the mixture M09 has 1.6%–2.5% and 0.7%–1% higher compressor work than R-12 in theoretical and experimental studies, respectively.

The COP values calculated from both the simulation and experimental studies are compared in Fig. 9, which shows that the COP decreases with an increase in ambient temperature. It is to be noted that the predictions for R-12 are closer to experimental results than M09 because the existing heat transfer correlations are well defined for a pure substance. The mixture M09 shows 15.5%–18.55%
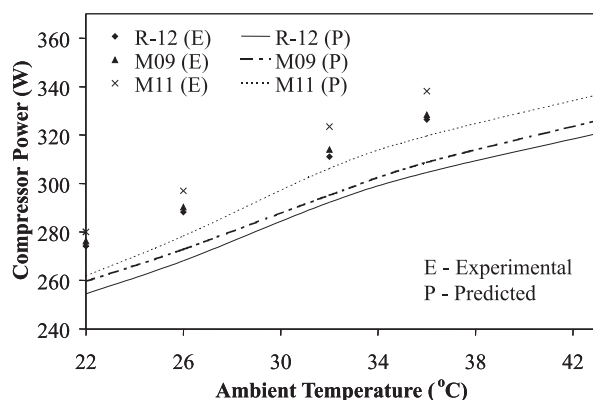

FIG. 8: Variation of experimental and predicted compressor power with ambient temperature at 1°C cabin temperature
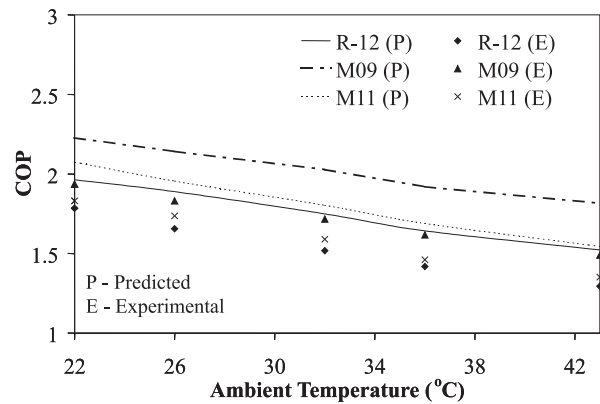
improvement in COP as compared to R-12 in simulation. Also, by experiments, the improvement in COP of M09 was found to be 10.4%–16.3%. Even though the compressor work of the M09 is higher than that of R-12, due to its higher refrigeration effect, higher COP is possible.

5. CONCLUSIONS

On the basis of the results obtained from both simulation and experimental studies, the flowing conclusions are made.

1. The *P-V* diagram of the compressor used in the visi-cooler shows that the M09 has 20% and 16% higher pressure in suction and discharge, respectively, than R-12. However, the pressure ratio of M09 was 5.8% less than that of R-12 for the same system operating conditions. Even though the operating pressures of M09 are higher than R-12, it shows only 1% higher compression work than R-12.

2. The theoretical investigation on visi-coolers shows that the existing condenser and evaporator are sufficient for M09.

3. The better heat transfer characteristics of M09 have resulted in a 20.4% shorter pull-down time, leading to 10.8%–19.6% less per day energy consumption in spite of a 2%–4% higher compressor power.

4. The capillary tube used for M09 is the same as that used in the R-12 system. Hence there is no need to change the capillary tube while M09 is charged.

5. Since the HC component in the M09 is only 0.09, mass fraction flammability of the refrigerant will not be a serious issue.

6. The maximum deviation of the predicted results from experimental values falls within 12%. This validates the model. The continuous safe running of the system for 18 months proved the oil miscibility of the M09 with mineral oil.

ACKNOWLEDGMENTS

REFERENCES

Bansal, P. K. and Rupasinghe, A. S., An homogeneous model for adiabatic capillary tubes, *Appl. Thermal Eng.,* vol. **18**, pp. 207–219, 1998.

Carpenter, N. E., Retrofitting HFC 134a into existing CFC 12 systems, *Int. J. Refrigeration,* vol. **15**, pp. 332–348, 1992.

Chang, Y. S., Kim, M. S., and Ro, S. T., Performance and heat transfer characteristics of hydrocarbon refrigerants in a heat pump system, *Int. J. Refrigeration,* vol. **23**, pp. 232–242, 2000.

Chi, J. and Didion, D., A simulation model of the transient performance of a heat pump, *Int. J. Refrigeration,* vol. **5**, pp. 176–184, 1982.

Chung, M. A., Numerical procedure for simulation of Fanno flows of refrigerants or refrigerant mixtures in capillary tubes, *ASHRAE Trans.,* vol. **104**, pp. 1031–1043, 1998.

Chung, B. C., Ding, C. L., and Chi, C. W., Analysis of evaporation of non-azeotropic refrigerants in a horizontal tube, *Appl. Thermal Eng.,* vol. **16**, pp. 817–827, 1996.

Colbourne, D., An overview of hydrocarbons as replacement refrigerants in commercial refrigeration and air conditioning, in *Refrigeration,* pp. 1–15, Northern Ireland Centre For Energy Research and Tech, Belfast, 2000.

Cooper, M. G., Heat flow rated in saturated nucleate pool boiling-wide ranging examination using reduced properties, *Adv. Heat Transfer,* vol. **16**, pp. 157–239, 1984.

Devotta, S. and Gopichand, S., Comparative assessment of HFC134a and some refrigerants as alternatives to CFC12, *Int. J. Refrigeration,* vol. **15**, pp. 112–118, 1992.

Domanski, P. A. and McLinden, M. O., A simplified cycle simulation model for the performance rating of refrigerants and refrigerant mixtures, *Int. J. Refrigeration,* vol. **15**, pp. 81–88, 1992.

Geoffrey, G. H. and Chen, J. A., Computer simulation program for mixed refrigerant air conditioning, *Int. J. Refrigeration,* vol. **17**, pp. 343–350, 1994.

Granryd, E., Hydrocarbons as refrigerants: An overview, *Int. J. Refrigeration,* vol. **24**, pp. 15–24, 2001.

Hambraeus, K., Heat transfer coefficient during two-phase flow boiling of HFC-134a, *Int. J. Refrigeration,* vol. **14**, pp. 357–362, 1991.

Incropera, F. P. and DeWitt, D. P., *Fundamentals of Heat and Mass Transfer,* 4th ed., John Wiley, New York, 1996.

Janssen, M. and Engels, F., The use of HFC134a with mineral oil in hermetic cooling equipment, report 95403/NO 07, International Congress of Refrigeration, the Hague, 1995.

John, J. and Radermacher, R., A heat exchanger model for mixtures and pure refrigerant cycle simulations, *Int. J. Refrigeration,* vol. **20**, pp. 244–255, 1997.

Jung, D. S., McLinden, M., Radermacher, R., and Didion, D., Horizontal flow boiling heat transfer experiments with a mixture of R22/R114, *Int. J. Heat Mass Transfer*, vol. **32**, pp. 131–145, 1989a.

Jung, D. S., McLinden, M., Radermacher, R., and Didion, D., A study of flow boiling heat transfer with refrigerant mixtures, *Int. J. Heat Mass Transfer*, vol. **32**, pp. 1751–1764, 1989b.

Jung, D. S. and Radermacher, R., Performance simulation of single-evaporator domestic refrigerators charged with pure and mixed refrigerants, *Int. J. Refrigeration*, vol. **14**, pp. 223–232, 1991.

Jung, D., Kim, C. B., Lim, B. H., and Lee, H. W., Testing of a hydrocarbon mixture in domestic refrigerators, *ASHRAE Trans.,* vol. **19**, pp. 1077–1084, 1996.

Manglik, R. M. and Bergles, A. E., Heat transfer and pressure drop correlations for the rectangular offset-strip-fin compact heat exchanger, *Exp. Thermal Fluid Sci.,* vol. **10**, pp. 171–180, 1995.

McLinden, M. O., Klein, S. A., Lemmon, E. W., and Peskin, A. P., NIST thermodynamic and transport properties of refrigerant mixtures—REFPROP, version 6.01, NIST Standard Reference Database 23, National Institute of Standards and Technology, Gaithersburg, 1998.

Metin, T. and Nilufer, E. A., Mathematical model for finned tube heat exchangers for thermal simulation software for air conditioners, *Int. Commun. Heat Mass Transfer,* vol. **29**, pp. 547–556, 2002.

Molina, M. J. and Rowland, F. S., Stratospheric sink for chlorofluoromethanes: Chlorine atom-catalysed destruction of ozone, *Nature,* vol. **249**, pp. 810–812, 1974.

Padhy, K. S., Heat transfer model of a rotary compressor,

in *Proc. Int. Compressor Engineering Conf.,* pp. 405–417, 1992.

Perry, R. H. and Chilton, C. H., *Perry's Chemical Engineering Hand Book,* 6th ed., McGraw-Hill Professional, New York, 1984.

Sekhar, S. J., Kumar, K. S., and Lal, D. M., Ozone friendly HFC134a/HC mixture compatible with mineral oil in refrigeration system improves energy efficiency of a walk in cooler, *Energy Conversion Manage.,* vol. **45**, pp. 1175–1186, 2004a.

Sekhar, S. J., Lal, D. M., and Renganarayanan, S., Improved energy efficiency for CFC domestic refrigerators retrofitted with ozone-friendly HFC134a/HC refrigerant mixture, *Int. J. Thermal Sci.,* vol. **43**, pp. 307–314, 2004b.

Spauschus, H. O., HFC134a as a substitute refrigerant for CFC 12, *Int. J. Refrigeration,* vol. **11**, pp. 389–392, 1988.

Stoecker, W. F. and Jones, J. W., *Refrigeration and Air Conditioning,* 2nd ed., McGraw-Hill, New York, 1983.

Traviss, D. P., Rohsenhow, W., and Baron, A., Forced convective condensation in tubes: A heat transfer correlation for condenser design, *ASME Trans.,* vol. **79**, pp. 157–165, 1973.

United Nations Environment Programme, Montreal protocol on substances that deplete the ozone layer—Final act (1989).

Wang, H. and Touber, S., Distributed and non-steady-state modelling of an air cooler, *Int. J. Refrigeration,* vol. **14**, pp. 98–319, 1991.

Wattelet, J. P., Chato, J. C., Souza, A. L., and Christoffersen, B. R., Evaporative characteristics of R12, R134a and a mixture at low mass fluxes, *ASHRAE Trans. Symposia,* vol. **2**, pp. 603–615, 1994.

William, A. M. and Thompson, H. D., An experimental investigation into heat transfer to the suction gas in low side hermetic refrigeration compressor, in *Proc. Int. Compressor Conf.*, pp. 908–916, 1988.

Zhi, J. C. and Wei, H. L., Dynamic simulation and optimal matching of a small-scale refrigeration system, *Int. J. Refrigeration,* vol. **14**, pp. 329–339, 1991.

ESTIMATION OF THE ABLATIVE PARAMETERS IN ABLATIVE COMPOSITES USING NONLINEAR PARAMETER ESTIMATION METHODS

A. Hakkaki-Fard,[1] F. Kowsary,[1] A. Pourshaghaghy,[2,] & M. Sefidgar[1]*

[1]*Department of Mechanical Engineering, University of Tehran, Tehran, Iran*

[2]*Islamic Azad University, Qazvin Branch, Qazvin, Iran*

*Address all correspondence to A. Pourshaghaghy E-mail: apoursh@gmail.com

In this article, nine ablative parameters of ablative composites are estimated using nonlinear inverse methods. The mathematical model of the ablative composite when exposed to a thermally harsh condition has been developed on the basis of the decomposition of the resin and formation of the char layer at a critical temperature. Three zones of virgin material, pyrolysis zone, and char layer along with two moving boundary surfaces are incorporated into the thermal model. The Levenberg-Marquardt method is used for estimating the unknown properties. Considering the nonlinear behavior of the inverse problem and the insulating behavior of the composite, the convergence of the solution method is acceptable and the estimated parameters are reliable.

KEY WORDS: *modeling, high-temperature properties, thermal properties, carbon fibers, parameter estimation*

1. INTRODUCTION

As a result of the growing need for high-strength, low-density, and high-temperature materials in the aerospace industry, composite materials are increasingly used in demanding structural applications in which they may be exposed to thermally harsh conditions. A good estimation of their thermophysical properties is required for predicting their performance in actual working conditions. As there is no available standard for testing these materials, there is a need for an inverse code that estimates required properties using measured temperatures in working conditions. In this article, nine ablative parameters of ablative phenolic composite, designed for thermal protection, are estimated using parameter estimation methods.

Inverse methods are commonly used for thermophysical parameter estimation problems. Beck (1966) estimated the thermal conductivity simultaneously with the volumetric heat capacity of nickel using the one-dimensional transient temperature measurements. Scott and Beck (1992a) estimated these thermal properties for carbon/epoxy composites as a function of the tempera-

ture and fiber orientation. They also developed a methodology for the estimation of these two properties in the same composite materials during curing (Scott and Beck, 1992b). Subsequent studies have been devoted to the inverse solution of different parameter estimation problems in composites (Taktak et al., 1993; Carvalho and Neto, 1999).

Owing to the importance of the ablative insulators in the aerospace industry, much research has been carried out regarding the behavior of this type of composite, some of which can be found in reference books (Rohsenow, 1973). Some other works regarding thermal properties of ablative composites (Ohlhorst et al., 1997), ablation characteristics of ablating insulators (Norman and Ronald, 1961; Firouzmanesh and Aref Azar, 2004; Nesmelov et al., 2003), and use of these kinds of insulators in the aerospace industry (Sohi, 1971) are concerned with direct problems in ablative composites.

There are few publications on the inverse problems in ablative composites. Four notable works in this field include Wilson (1965), Cozzens and Fox (1978), Hakkaki-Fard and Kowsary (2008), and Kanevce and Kanevce

NOMENCLATURE

B_p	Arrhenius constant (1/s)	$\dot{m}_c$	specific ablation mass flow rate
c	specific heat (J/kgK)		(specific mass flow rate of ablated char)
E	activation energy per unit mass (J/kg)		(kg/m^{2}s)
H_p	enthalpy of gases from pyrolysis per	M	total number of temperatures measured
	unit mass (J/kg)		by each of the sensors
I	identity matrix	$\tilde{m}$	total number of temperature measurement
k	thermal conductivity (W/mK)		by all sensors ($\tilde{m} = m \times M$)
m	number of sensors	n	number of unknown parameters
Greek Symbols		p	pyrolysis
ε	very small value or the fraction of	$q(t)$	heat flux (W/m^2)
	resin transformed to gas	R	gas constant
ΔH_p	specific pyrolysis heat (J/kg)	s	surface
ΔH_c	specific heat of ablation (J/kg)	S	objective function, Eq. (13)
ρ	density (kg/m^3)	v	virgin material
σ	standard deviation of the measured	**Superscripts**	
	temperature errors	i	number of iteration
Subscripts		T_a	ablation temperature
ab	ablation	T	temperature
c	char	t	time (s)
g	gases from pyrolysis	T	transpose of a matrix
$\dot{m}_p$	specific pyrolysis mass flow rate (kg/m^{2}s)	x	position (m)

(1999). The first two ones used experimental techniques for estimation of unknown properties in ablating composites. The third one is a function estimation solution of surface heat flux in a charring ablator using the conjugate gradient method with adjoint problems. In the work of Kanevce and Kanevce (1999), seven parameters of the ablating composites are estimated using the inverse technique and the Levenberg-Marquardt method. In that work, ablation temperature and the specific heat of the composite are assumed to be known, but in the present study, it is assumed that all of the ablation parameters of the composite are unknown. This is because the ablation temperature plays an important role in the ablation process, and this parameter differs for a specific composite while using different working conditions.

2. DIRECT PROBLEM

The geometry of a one-dimensional ablation problem is illustrated in Fig. 1. When the composite is subject to ex-

treme heat loads, decomposition of the resin and formation of char layer are begun. When the temperature at the surface of the char layer reaches the critical ablation temperature, the outer layer of the formed char begins to ablate. In this situation, two processes (char formation and ablation) take place simultaneously. Three zones can be formed in the material: the virgin material, the pyrolysis zone, and the char layer (Fig. 1). In the mathematical formulation presented in the following, we assume there are two zones (Fig. 2): the virgin and the char zone; that is, a simplification is made, and we assume the pyrolysis is collapsed on the interface of the virgin and the char layer. It can be seen in Fig. 1 that the boundaries s_1 and s_2 are two moving boundaries and s_3 is a stationary one. Also, the region identified by δ_1 represents the char layer, and the region represented by δ_2 is the virgin material's zone. The governing differential equations for the thermal fields in two regions are (Hakkaki-Fard and Kowsary, 2008; Kanevce and Kanevce, 1999; Hakkaki-Fard, 2006) as follows:
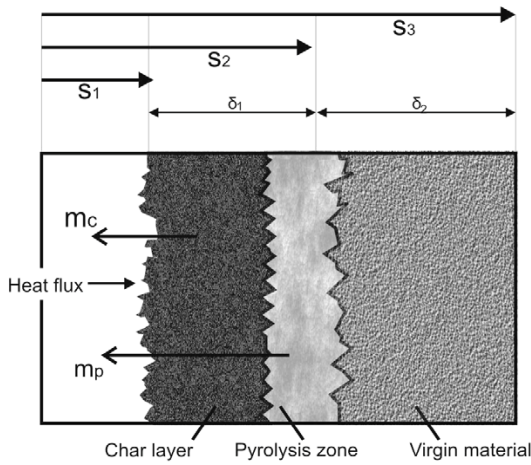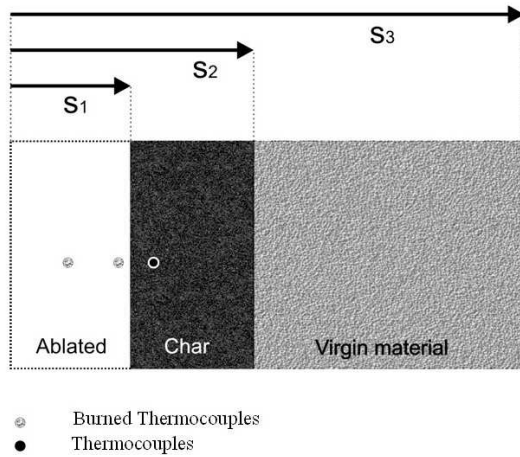
FIG. 1: Zones within the ablating composite

FIG. 2: States of the zones and the sensors at the end of the experiment

$$
\begin{cases}
k_c \dfrac{\partial^2 T}{\partial x^2} + \dot{m}_p c_g \dfrac{\partial T}{\partial x} = \rho_c c_c \dfrac{\partial T}{\partial \tau} & (1) \\[2mm]
s_1(t) < x < s_2(t) & \\[4mm]
k_v \dfrac{\partial^2 T}{\partial x^2} = \rho_v c_v \dfrac{\partial T}{\partial \tau} & (2) \\[2mm]
s_2(t) < x < s_3(t) &
\end{cases}
$$

while the boundary conditions are given by the following:

$$
-k_c \frac{\partial T}{\partial x} + \dot{m}_p H_p + \dot{m}_c \cdot \Delta H_c = q(t) \quad x = s_1(t) \quad (3)
$$

$$
-k_c \frac{\partial T}{\partial x} = -k_v \frac{\partial T}{\partial x} + \dot{m}_p \cdot \Delta H_p \quad x = s_2(t) \quad (4)
$$

$$
-k_v \frac{\partial T}{\partial x} = 0 \quad x = s_3(t) \tag{5}
$$

and the initial condition is given by the following:

$$
T(x,0) = T_0 \tag{6}
$$

The involved parameters in the preceding equations have been defined in the nomenclature.

The ablation model involves two zones and two moving boundaries, s_1 and s_2, and a fixed boundary, s_3. Corresponding equations for defining boundaries are given as follows:

$$
s_1(t) = \int_0^t \frac{\dot{m}_c}{\rho_c} \, dt \tag{7}
$$

$$
s_2(t) = \int_0^t \frac{\dot{m}_p}{\rho_v - \rho_c} \, dt \tag{8}
$$

$$
s_3(t) = \text{const} \tag{9}
$$

To complete the system of equations of the in-depth ablation model, it is necessary to include equations for calculating the pyrolysis mass flow rate. The motion of the pyrolysis zone is defined by the kinetics of the phenolic resin decomposition. It is assumed that the rate of decomposition may be expressed by a first-degree reaction:

$$
\frac{\partial \varepsilon}{\partial \tau} = B_p \left(\frac{\rho_v - \rho_c}{\rho_v} - \varepsilon(x,t) \right) e^{-\frac{E}{RT}} \tag{10}
$$

Utilizing Eq. (10), the mass flow rate of the pyrolysis gas can be expressed as follows:

$$
\dot{m}_p = \int_{s_2}^{s_3} \rho_v B_p \left(\frac{\rho_v - \rho_c}{\rho_v} - \varepsilon \right) \exp \left(\frac{-E}{RT} \right) dx \tag{11}
$$

Now that the sets of equations is completed, the implicit Laasonen method (refer to Tannehill et al., 1997) is used to descretize time and space derivatives to achieve the solution. This method has a first-order accuracy in time with a truncation error of $O[\Delta t, (\Delta x)^2]$ and is unconditionally stable. Common forward or backward second-order space finite differences have been applied to the boundary conditions. Owing to the high heat flux and low conductivity of the insulator, small time and space steps are selected to achieve the necessary accuracy. Moreover, because of the movement of the boundaries, the volume of fluid method (VOF) (Jong et al., 2005) is used. In the VOF method, the fraction function is defined

to be equal to 1.0 in the char or the virgin region and 0.0 in the ablated region. By using the VOF method, there is no need to regrid the insulator in each time. This makes the computation much more efficient. In the next section, the inverse problem is developed.

3. INVERSE PROBLEM

It is assumed that all of the ablation parameters involved in Eqs. (1)–(11) are known in the direct problem, but the nine parameters are unknown in the inverse problem. The unknown parameters are ablation temperature T_a, thermal conductivity of char k_c, density of char ρ_c, specific heat of char C_c, enthalpy of gases from pyrolysis H_p, specific pyrolysis heat ΔH_p, specific ablation heat ΔH_c, and Arrhenius constants B_p and E. These unknown ablation parameters can be gathered in a single unknown vector $\mathbf{P}$ as follows:

$$\mathbf{P} = [T_a, k_c, \rho_c, C_c, H_p, \Delta H_p, \Delta H_c, B_p, E] \qquad (12)$$

These unknown parameters are to be estimated using temperatures measured by sensors located inside the insulator, as seen in Fig. 2. The surface heat flux $q(t)$ and the initial temperature T_0 are assumed to be known in this inverse problem. It is worth mentioning that our first try for solving the problem was initially assumed to be our 10th unknown, but we found that because of the very small sensitivity of this parameter to the measured temperatures, it is not possible to estimate it independently and together with other unknowns. It should also be noted that due to the occurrence of high temperature values near the active surface and its deterioration during the experiment, common thermal sensors may not withstand such harsh conditions and are burned out (Fig. 2). On the other hand, if the sensors are located far from the active surface, the sensitivity of the measured temperatures to the required parameters reduces appreciably; therefore the determination of the optimal sensor location is not an easy task in this work. A deep sensitivity analysis should be performed to determine the best location for sensors. In Fig. 2, the states of the sensors and insulators' regions at the end of the experiment are illustrated.

To estimate the nine ablative parameters in the inverse problem, a nonlinear optimization problem is defined in which finding the minimum of the sum of squared differences between experimental and calculated temperatures is sought:

$$S\left(\mathbf{P}\right) = \sum_{i=1}^{m} \sum_{j=1}^{M} \left[T_{i,j}\left(\mathbf{P}\right) - Y_{i,j}\right]^2 \qquad (13)$$

where m is the number of sensors, M is the total number of temperatures measured by each of the sensors, $Y_{i,j}$ s are the measured temperatures, and $T_{i,j}$ s are the calculated temperatures at the measurement locations using the proposed model Eqs. (1)–(6) and arbitrary values for unknown parameters.

Thus the problem in hand may be categorized as a nonlinear programming optimization one. One of the methods for solving this type of problem is the Levenberg-Marquardt method (LMM), as described next.

3.1 Computational Procedure for Inverse Method

The inverse solution algorithm based on LMM is an iterative method, and the computational procedure for the estimation of the unknown parameters at iteration i can be summarized as follows (more details of which may be found in the book by Ozisik and Orlande (2000)).

1. Solve the direct problem given by Eqs. (1)–(6) with available estimated $\overrightarrow{P}^i$ to obtain temperature fields in virgin and char materials $T(\overrightarrow{P}^i)$.

2. Compute S from Eq. (13).

3. Compute the sensitivity matrix X^i defined by the following equation:

$$X_{\tilde{m} \times n} = \begin{bmatrix} \dfrac{\partial T_{1,1}}{\partial P_1} & \dfrac{\partial T_{1,1}}{\partial P_2} & \cdots & \dfrac{\partial T_{1,1}}{\partial P_n} \\[2mm] \dfrac{\partial T_{1,2}}{\partial P_1} & \dfrac{\partial T_{1,2}}{\partial P_2} & \cdots & \dfrac{\partial T_{1,2}}{\partial P_n} \\[2mm] \vdots & \vdots & & \vdots \\[2mm] \dfrac{\partial T_{1,M}}{\partial P_1} & \dfrac{\partial T_{1,M}}{\partial P_2} & & \dfrac{\partial T_{1,M}}{\partial P_n} \\[2mm] \dfrac{\partial T_{2,1}}{\partial P_1} & \dfrac{\partial T_{2,1}}{\partial P_2} & & \dfrac{\partial T_{2,1}}{\partial P_n} \\[2mm] \dfrac{\partial T_{2,2}}{\partial P_1} & \dfrac{\partial T_{2,2}}{\partial P_2} & & \dfrac{\partial T_{2,2}}{\partial P_n} \\[2mm] \vdots & \vdots & & \vdots \\[2mm] \dfrac{\partial T_{m,M}}{\partial P_1} & \dfrac{\partial T_{m,M}}{\partial P_2} & \cdots & \dfrac{\partial T_{m,M}}{\partial P_n} \end{bmatrix} \qquad (14)$$

P_1 to P_n denote the components of the unknown vector $\mathbf{P}$. Parameter $\tilde{m}$ is the total number of temperature measurement by all sensors ($\tilde{m} = m \times M$).

4. Solve the following linear system of equation to find $\Delta \overrightarrow{P}^{(i)}$:

$$
\begin{aligned}
&\left[\lambda^{(i)} I + X^{T(i)} X^{(i)}\right] \Delta \mathbf{P}^{(i)} = X^{T(i)} \\
&\times \left(\mathbf{T}^{(i)} - \mathbf{Y}^{(i)}\right)
\end{aligned}
\tag{15}
$$

where superscript T denotes the transpose sign and vectors $\mathbf{T}$ and $\mathbf{Y}$ are defined as

$$
\begin{aligned}
\overrightarrow{T}_{1\times\tilde{m}}^{(i)} &= \big[T_{1,1}, T_{1,2}, ..., T_{1,M}, T_{2,1}, T_{2,2}, \\
&..., T_{2,M}, ..., T_{m,M}\big]^{(i)}
\end{aligned}
\tag{16}
$$

$$
\begin{aligned}
\overrightarrow{Y}_{1\times\tilde{m}}^{(i)} &= \big[Y_{1,1}, Y_{1,2}, ..., Y_{1,M}, Y_{2,1}, Y_{2,2}, \\
&..., Y_{2,M}, ..., Y_{m,M}\big]^{(i)}
\end{aligned}
\tag{17}
$$

where the initial value for $\lambda^{(i)}$ is set to 0.01.

5. The updating rule for the LMM's algorithm is then applied to determine the unknown vector:

$$
\mathbf{P}^{(i+1)} = \mathbf{P}^{(i)} + \Delta \mathbf{P}^{(i)}
\tag{18}
$$

6. Solve the direct problem of Eqs. (1)–(6) with this new estimated $\mathbf{P}^{i+1}$ to obtain $T\left(\mathbf{P}^{i+1}\right)$, then compute S, as defined by Eq. (13).

7. If $S(\mathbf{P}^{i+1}) \geq S(\mathbf{P}^i)$, replace λ^i by $10 \times \lambda^i$ and return to step 4.

8. If $S(\mathbf{P}^{i+1}) < S(\mathbf{P}^i)$, accept the new estimated $\mathbf{P}^{i+1}$ and replace λ^i by $0.1 \times \lambda^i$.

9. Check the stopping criteria given by Eq. (19):

$$
S\left(\mathbf{P}^n\right) < \mu
\tag{19}
$$

Stop the iteration procedure if it is satisfied; otherwise, replace i by $i + 1$ and return to step 3.

For errorless (nonnoisy) temperature data, the μ in Eq. (19) can be chosen to be an arbitrary small value.

When the measured temperatures contain noise, as is the case in a real experiment, we do not expect the target function defined by Eq. (13) to become equal to zero at the final iteration step; therefore, according to a suggestion by Oliveira and Orlande (2004) as well as Colaco and Orlande (1999), we use the following expression for μ:

$$
\mu = m \times M \times \sigma^2
\tag{20}
$$

where σ is the standard deviation of the measured temperature errors.

4. RESULTS AND DISCUSSION

We now examine the present analysis for estimation of the nine unknown parameters collected in the vector $\mathbf{P}$ in Eq. (12). For all test cases considered in this work, the ablative material is a carbon phenolic composite with properties as given in Table 1 of Kanevce and Kanevce (1999). The thermal conductivity, density, and specific heat of the composite at room temperature are $k_v = 0.76$ W/mK, $\rho_v = 1340\,\text{kg/m}^3$, and $C_v = 1249$ J/kgK. The thickness of the slab was taken as 9 mm, and the slab was assumed to be initially at the uniform temperature of 300 K. The domain is discretized into a fine grid network with $\Delta x = 2 \times 10^{-6}$ m. The duration of the experiment, that is, the total time of heat flux exposure, was assumed to be 4.5 s. Heat transfer on the composite surface was considered in combined convective-radiative modes as the following equation, and its value is shown in Fig. 3:

$$
\begin{aligned}
q(t) &= h_g(T_g - T_s) + \varepsilon_g \sigma(T_g^4 - T_s^4) \\
&- \varepsilon_s \sigma(T_s^4 - T_{\text{surr}}^4)
\end{aligned}
\tag{21}
$$

with the convective coefficient of $h_g = 19,700$ W/m^2 K, ambient gas, and surrounding temperature of $T_g = 3170$ K, $T_{\text{surr}} = 300$ K, respectively. The emissivity coefficients for gas and surface are $\varepsilon_g = 1$ and $\varepsilon_s = 0.8$, respectively. To calculate $q(t)$ at any time step (2×10^{-4} s), the value of T_s in the preceding equation is taken as its

TABLE 1: Actual properties of the used carbon phenolic composite

C_c (J/kgK)	C_v (J/kgK)	ρ_c (kg/m^3)	ρ_v (kg/m^3)	k_c (W/m K)	k_v (W/m K)
1978	1249	1019	1340	2.407	0.76

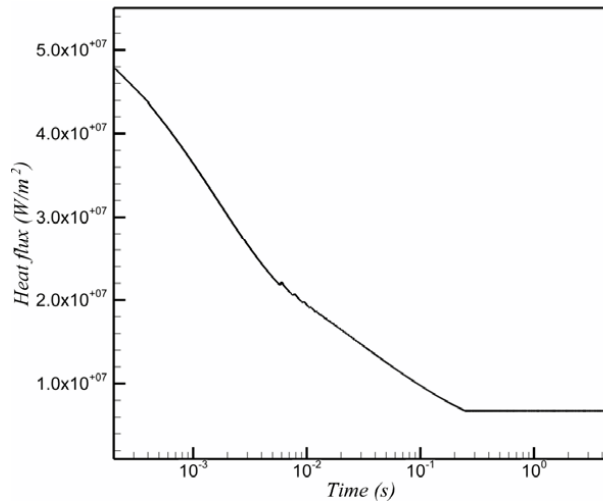| E/R (K)	B_p (s^{-1})	T_a (K)	ΔH_c (J/kg)	ΔH_p (J/kg)	H_p (J/kg)
2.3×10^4	9.9×10^6	2870	3.2×10^6	7.5×10^6	1.3×10^6

FIG. 3: Applied heat flux on the composite surface in the parameter estimation procedure

value in the previous time step. It is assumed that the sensors are capable of sustaining high temperature to 2000 K, and data readings were taken every 0.1 s. The thermocouples are placed in the virgin material at appropriate locations. Some of the thermocouples may be burned out during the course of the measurement. In this situation, it is assumed that the burned sensors return zero values; hence it does not affect the mathematical formulation given previously. The minimum number of sensors used for this problem by which reasonable results could be obtained was three; therefore the total number of temperature readings that has been taken in this simulation in accordance with the sensor limitations was 82 samples. These three sensors were located at $x = 1^{mm}$, $x = 1.3^{mm}$, and $x = 1.6^{mm}$ (x is the distance from the active surface). Three sets of data were used in this study: (1) errorless data by which the inverse algorithm is tested; (2) data containing additive errors based on what was proposed by Ozisik and Orlande (2000) as having a Gaussian distribution with standard deviation equal to 0.5% of the ablating temperature, that is, $\sigma = 8.5$ K; and (3) data containing errors having a Gaussian distribution with standard deviation equal to 1% of the ablating temperature (corresponding roughly to a 17 K error).

The initial guess for **P** in an inverse algorithm is very important for the convergence of the algorithm. Generally, the choice of initial guess depends on some knowledge about the order of magnitude of these parameters. An improper guess may cause the program to diverge,

while a good one helps the better convergence of the program. For example, if the density of the char layer is chosen bigger than that of a virgin material (i.e., a wrong initial guess), it may cause the direct solution to diverge on the whole. Table 2 shows the generated initial guessed parameters for this study. These values are obtained somewhat randomly; although, as was said earlier, their orders of magnitude are assumed to be known.

Figure 4 illustrates the reduction history of the objective functional with respect to the number of iterations in LMM for the different levels of measurement errors. Figure 5 illustrates noisy temperature data acquired from the direct problem used for parameter estimation in the inverse procedure.

The estimated parameters for different cases are compared with actual parameters in Table 3. The root mean square error of the estimated vector **P** with respect to actual **P** given in Table 3 is defined as

$$\text{RMS} = \sqrt{\frac{1}{m.M} \sum_{j=1}^{m} \sum_{i=1}^{M} \left(T_{i,j}\left(\mathbf{P}\right) - Y_{i,j}\right)^2} \qquad (22)$$

The estimated parameters are sufficiently accurate considering the fact that the used material is an insulator that causes the measured temperatures to have a low sensitivity to the surface heat flux.
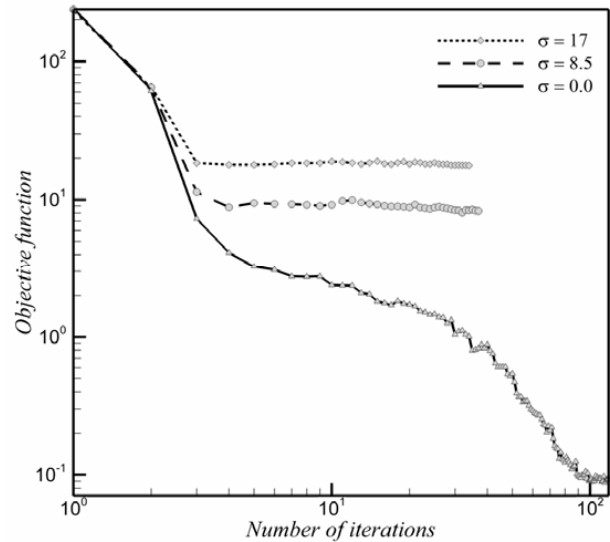

FIG. 4: Reduction history of the objective function for different cases

TABLE 2: Initial guess for unknown parameters

T_a (K)	ρ_c (kg/m^3)	k_c (W/m K)	C_c (J/kgK)	E/R (K)	B_p (s^{-1})	ΔH_c (J/kg)	ΔH_p (J/kg)	H_p (J/kg)
2800	1005	2.28	1873	2.4×10^4	7×10^6	5×10^6	6×10^6	1.0×10^6

TABLE 3: Estimated parameters for different cases

RMS (K)	E/R $\times 10^{-4}$ (K)	B_p $\times 10^{-6}$ (s^{-1})	ΔH_p $\times 10^{-6}$ (J/kg)	H_p $\times 10^{-6}$ (J/kg)	ΔH_c $\times 10^{-6}$ (J/kg)	c_c (J/kgK)	k_c (W/m K)	ρ_c (kg/m^3)	T_a (K)	Noise variance, σ (K)
0.23	2.26	8.00	6.75	1.76	3.15	1856	2.23	1014	2873	0
9.70	2.18	7.12	7.06	3.77	3.91	1355	2.47	982	2852	8.5
16.70	2.23	12.0	4.72	3.69	2.64	1843	2.16	988	2880	17
0	2.3	9.9	7.5	1.3	3.2	1978	2.41	1019	2870	Actual parameter

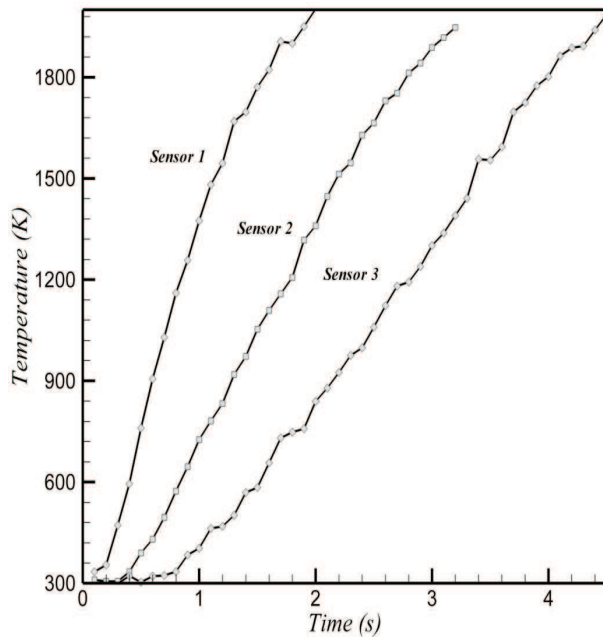**FIG. 5:** Noisy temperatures used for parameter estimation ($\sigma = 17$ K)

FIG. 6: Comparison of computed temperatures at the sensor locations using actual, estimated, and initial guessed parameters (errorless data)

Figures 6–8 illustrate the comparison of the computed temperatures at the sensor locations using actual, estimated, and the initial guessed parameters separately for different noise levels. These figures can be used to assess the accuracy of the estimated parameters. As is sho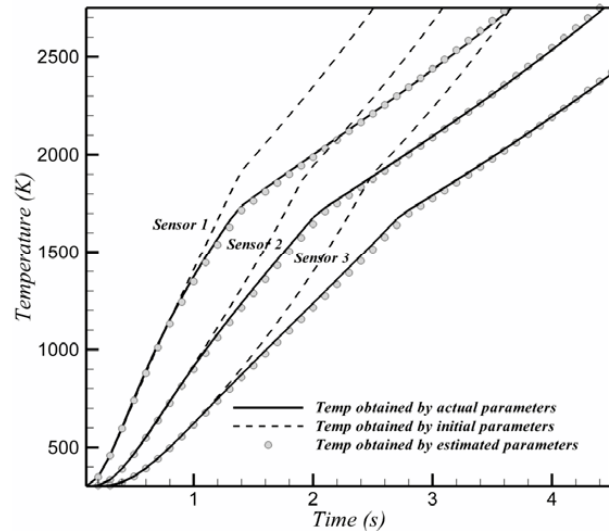wn in Figs. 6–8, while the temperature range used for the parameter estimation procedure was limited to 2000 K (because of the sensor limitations), the temperature profiles obtained from estimated parameters match well with the temperature profile obtained by actual parameters even at higher temperatures. It should be noted that these kinds of insulators are applied for long periods in their real applications; therefore it is very important that the estimated parameters obtained from sensor temperatures in a lim-
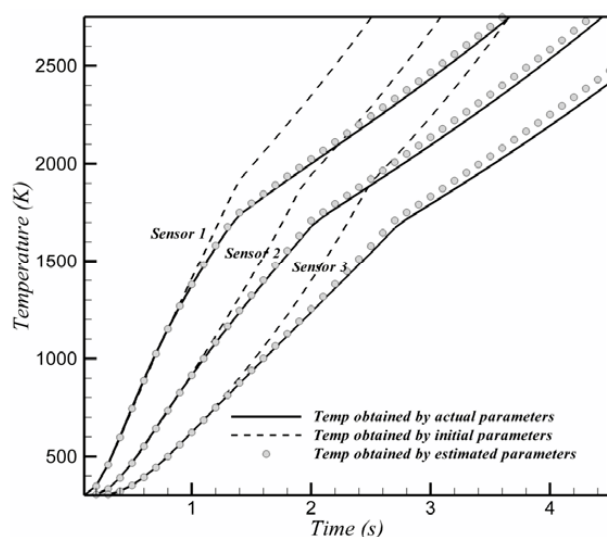
FIG. 7: Comparison of computed temperatures at the sensor locations using actual, estimated, and initial guessed parameters (noise level σ = 8.5 K)
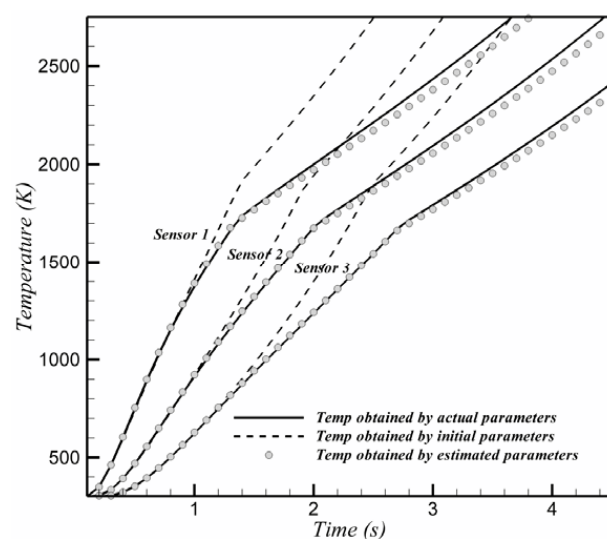

FIG. 8: Comparison of computed temperatures at the sensor locations using actual, estimated, and initial guessed parameters (noise level σ = 17 K)

thalpy of gases from pyrolysis (H_p), despite its high relative error value of 190%, does not have any major effect on the design aspects of the ablative composite problems. The important parameter of T_a, the temperature at which the ablation of composite is started, has been estimated very precisely with relative error of less than 1%.

5. CONCLUSION

In this article, nine ablative parameters of a phenolic composite were estimated using Levenberg-Marquardt's algorithm. Results match well with actual parameters. It is possible to use this procedure for other ablative composites and estimate their unknown ablative parameters. The enthalpy of gases from pyrolysis (H_p) could not be estimated precisely, and this parameter, contrary to the ablative temperature T_a, does not have a key role in the design of such composites.

REFERENCES

Beck, J. V., Transient determination of thermal properties, *Nucl. Eng. Design*, vol. **3**, pp. 373–381, 1966.

Carvalho, G. D. and Neto, A. J. S., Experimental design and optimization with inverse analysis for polymers thermal properties estimation, in *Third Int. Conf. on Inverse Problems in Engineering*, Port Ludlow, WA, 13-18 June, 1999.

Colaco, M. J. and Orlande, H. R. B., Comparison of different version of the conjugate gradient method of function estimation, *Numer. Heat Transfer, Part A*, vol. **36**, pp. 229–249, 1999.

Cozzens, R. F. and Fox, R. B., Infrared laser ablation of polymers, *Polymer Eng. Sci.*, vol. **18**, pp. 900–904, 1978.

Firouzmanesh, M. R. and Aref Azar, A., Study of thermal stability and ablation behavior of carbon fabric/epoxy-novolac ablative composites, *Int. J. Polymer. Mater.*, vol. **53**, pp. 541–552, 2004.

Hakkaki-Fard, A., Estimation of ablative parameters of ablative composites by nonlinear parameter estimation methods, M.S. thesis, University of Tehran, 2006.

Hakkaki-Fard, A. and Kowsary, F., Heat flux estimation in a charring ablator, *Numer. Heat Transfer, Part A*, vol. **53**, pp. 543–560, 2008.

Jong, S. P., Seung, M. K., Min, S. K., and Woo, I. L., Finite element analysis of flow and heat transfer with moving free surface using fixed grid system, *Int. J. Comput. Fluid Dyn.*, vol. **19**, pp. 263–276, 2005.

Kanevce, L. P. and Kanevce, G. H., Comparison of two kinds of experiments for estimation of thermal properties of ablative composite, in *Third Int. Conf. on Inverse Problems in Engineering*, Port Ludlow, Washington, USA, June 13–18, 1999.

ited time and temperature range be able to estimate their behavior in the whole time period of their application. Moreover, as observed in Figs. 6–8, the computed temperature matches excellently with temperature curves obtained from exact parameters. Thus the parameter of en-

Nesmelov, V. V., Gol'din, V. D., and Kostin, G. F., Ablation characteristics of thermal protective materials based on carbon fiber reinforced composites, *Combustion Explosion Shock Waves*, vol. **39**, pp. 309–315, 2003.

Norman, B. and Ronald, R. E., Ablation mechanisms in plastics with inorganic reinforcement, *ARS J.*, vol. **31**, pp. 532–539, 1961.

Ohlhorst, C. W., Vaughn, W. L., Ransone, P. O., and Tsou, H. T., Thermal conductivity database of various structural carbon-carbon composite materials, *NASA Tech. Memo.,* vol. **4787**, 1997.

Oliveira, A. P. D. and Orlande, H. R. B., Estimation of the heat flux at the surface of ablating materials by using temperature and surface position measurements, *Inverse Prob. Sci. Eng.*, vol. **12**, pp. 563–577, 2004.

Ozisik, M. N. and Orlande, H. R. B., *Inverse Heat Transfer Fundamentals and Applications*, Taylor and Francis, New York, 2000.

Rohsenow, W. M., *Handbook of Heat Transfer*, McGraw-Hill, New York, 1973.

Scott, E. P. and Beck, J. V., Estimation of thermal properties in carbon/epoxy matrix materials during curing, *J. Composite Mater.*, vol. **26**, pp. 21–36, 1992a.

Scott, E. P. and Beck, J. V., Estimation of thermal properties in epoxy matrix/carbon fiber composite materials, *J. Composite Mater.*, vol. **26**, pp. 132–149, 1992b.

Sohi, J. D., Development of low-cost ablative nozzles for large solid propellant rocket motors, *NASA Tech. Rep.*, report no. NASA-CR-72973, 1971.

Taktak, R., Beck, J. V., and Scott, E. P., Optimal experimental design for estimating thermal properties of composite materials, *Int. J. Heat Mass Transfer*, vol. **36**, pp. 2977–2986, 1993.

Tannehill, J. C., Anderson, D. A., and Pletcher, R. H., *Computational Fluid Mechanics and Heat Transfer*, Taylor & Francis, London, 1997.

Wilson, R. G., Hemispherical spectral emittance of ablation chars, carbon, and zirconia to 3700 K, *NASA Tech. Note*, vol. **D-2704**, 1965.

VISCOUS DISSIPATION EFFECTS ON HEAT TRANSFER FOR OSCILLATING FLOW IN A PIPE PARTIALLY FILLED WITH A POROUS MEDIUM

D. Dhahri,[*] *K. Slimi, & S. Ben Nasrallah*

Laboratoire d'Etudes des Systèmes Thermiques et Energétiques, Ecole Nationale d'Ingénieurs de Monastir, Rue Ibn Eljazzar, 5019 Monastir, Tunisia

[*]Address all correspondence to D. Dhahri E-mail: dhacen@yahoo.fr

A numerical study is reported here to investigate a laminar incompressible oscillating flow and heat transfer into a finite length pipe of circular cross section partially filled with an annular lining of porous medium. The porous substrate is attached to the wall, which is heated with uniform temperature. The flow in the porous material is described by the Brinkman-Lapwood-Forchheimer extended Darcy model with variable porosity. The model for the energy transport is based on the local thermal equilibrium assumption, between the fluid and the solid phases, and takes into account the viscous dissipation effects. The control volume–based finite element method (CVFEM) is used for solving the governing differential equations system with an unequal order velocity-pressure interpolation. A comprehensive analysis of the influence of the Darcy number, the Womersly number, the thermal conductivity ratio, the heat capacity ratio, the porous layer thickness, and the Eckert number is presented and discussed throughout the article.

KEY WORDS: *numerical, CVFEM, viscous dissipation, heat transfer, oscillating flow, porous media*

1. INTRODUCTION

The current research interest in fluid flow and heat transfer in porous media, being documented in several comprehensive books published recently by Nield and Bejan (1999), Vafai (2000), Pop and Ingham (2001), and Ingham and Pop (2002), is motivated by numerous practical applications that can be modeled or approximated as transport through porous media such as thermal insulation of buildings, packed bed heat exchangers, geothermal systems, drying technology, catalytic reactors, petroleum industries, and electronic cooling. Owing to these different applications, special attention has been paid to the internal flows in ducts and channels filled completely or partially with porous media. It is noteworthy that recent investigations have focused on the use of porous inserts to obtain heat transfer enhancements with a minimum of frictional losses. Furthermore, partial filling eliminates contact between the porous material layer and the fluid layer, which decreases heat losses from the porous mate-

rial to the surface. It is worth mentioning that for many industrial applications, there is no need to fill completely the system with the porous medium; rather a partial filling is sufficient (Mohamad, 2002).

Convective heat transfer in a composite system fluid/porous medium has been the topic of several studies published in the literature (Poulikakos and Kazmierczak, 1987; Huang and Vafai, 1994; Chikh et al., 1995a, 1995b; Zhang and Zhao, 2000). Recently, a numerical study of heat transfer enhancements in a cylinder partially filled with porous media with isothermal boundary conditions has been developed by Mohamad (2002). Renato and Marcelo (2003) have investigated numerical solutions for such a hybrid medium, considering a channel partially filled with a porous layer through which fluid flows in a turbulent regime. Costa et al. (2004) dealt with numerical simulation of non-Darcian flows through spaces partially filled with a porous medium. In this study, the flow within the porous medium is modeled by the Brinkman- Forchheimer extended Darcy model, and the porosity variation

NOMENCLATURE

A_o	dimensionless oscillation amplitude
C_p	specific heat capacity at constant pressure ($J\ K^{-1}\ kg^{-1}$)
D	channel diameter (m)
d_p	particle diameter (m)
Da	Darcy number, $\mathrm{Da} = K_\infty/D^2$
Ec	Eckert number, $\mathrm{Ec} = \mu_f\left(U_{\max}\right)^2/C_f \Delta T_{\mathrm{ref}}$
F	geometric function
k	thermal conductivity ($W\ m^{-1}\ K^{-1}$)
K	porous medium permeability (m^2)
P	dimensionless pressure
Pr	Prandtl number, $\mathrm{Pr} = \mu_f C_{pf}/k_f$
Re_w	kinetic Reynolds number, $\mathrm{Re}_w = \rho \omega D^2/\mu_f$
R_c	heat capacity ratio, $R_c = (\rho c)_{sd}/(\rho c)_f$
R_k	thermal conductivity ratio, $R_k = k_{sd}/k_f$
r, z	dimensionless radial and axial coordinates
r_i	radius of the fluid region

S	porous layer thickness, $S = r - r_1/R - r_1$
t	dimensionless time
T	dimensionless temperature
$\mathbf{U}$	dimensionless velocity vector

Greek Symbols

α	Womersly number, $\alpha = \sqrt{\mathrm{Re}_w}/2$
ω	oscillatory frequency
ε	porosity
λ	binary parameter
μ_f	dynamic fluid viscosity ($Kg\ m^{-1}\ s^{-1}$)
ρ	density ($Kg\ m^{-3}$)
Λ	permeability ratio, $\Lambda = K_\infty/K$

Subscripts

f	fluid
fr	oscillatory frequency
sd	solid
i	initial or inlet
∞	free

has been neglected. Deng and Martinez (2005) have considered the two-dimensional flow of a viscous fluid both over and through a porous medium. In the fluid-only region, the two-dimensional flow field is governed by the Navier-Stokes equation. The Brinkman–extended Darcy law relationship has been considered in a porous medium. Jen and Yan (2005) have presented a three-dimensional model for the analysis of the fluid flow and heat transfer in a square channel partially filled with a porous material. In this study, the porosity variation and viscous dissipation effects have been neglected.

Another potential application of fluid flow and heat transfer in porous media is found in thermal machines operating with an internal oscillating fluid flow (e.g., Stirling engine regenerators, internal combustion engines, filters). However, they may play a greater role in the near future due to their ability to operate with various energy sources brought externally: biogas, solar energy, geothermic energy, heat collected downstream of industrial processes, thermoacoustic waste heat upgrading. In this case, there are many areas requiring further investigation to better predict their performance and guide future designs for these machines. One important application, for example, is for oscillating flow regenerators. Leong and Jin (2005,

2006) have studied experimentally heat transfer in oscillating flow through a channel filled with open-cell aluminum foam with a fully interconnected pore structure and with different pore sizes: 10, 20, and 40 PPI. Khodadadi (1991) has treated analytically an oscillatory flow through a porous channel bounded by two impermeable parallel plates. Sozen and Vafai (1991) have presented an analysis of oscillating compressible flow through a packed bed. Fu et al. (2001) have studied experimentally heat transfer in a porous channel subjected to an oscillatory flow. They concluded that the length-average Nusselt number of oscillatory flow is higher than for steady flow. An experimental investigation of the temperature increase due to viscous dissipation in an oscillating pipe flow has been reported by Velarde et al. (2003). Jankowski and Majdalani (2003) have considered a laminar flow in a porous channel with a large wall section and weakly oscillatory pressure. Fang (2004) has investigated the heat transfer of oscillating and steady flows in a channel filled with a porous medium. Oscillatory flow in microporous media applied in pulse tube and Stirling-cycle cryocooler regenerators has been investigated by Cha et al. (2008). The authors have established a systematic experimental and Computational Fluid Dynamic (CFD) based proce-

dure for the quantification and directional permeability and Forchheimer's coefficients for porous structures under steady-periodic flow conditions.

Regardless of the relative importance of the frictional heating compared to the other heat transfer mechanisms in a composite system fluid/porous medium, there are some applications where one is willing to inspect the viscous dissipation effects. The effect of viscous dissipation has been included by Ingham et al. (1990) in the study of combined free and forced convection in a porous medium bounded by two vertical walls. Yee and Kamiuto (2002) have treated the viscous dissipation effects on forced convection heat transfer in cylindrical packed beds, taking into account the porosity variation. El-Amin (2003) has considered the combined effects of viscous dissipation and Joule heating on magnetohydrodynamic forced convection over a nonisothermal cylinder embedded in a fluid-saturated porous medium. Magyari et al. (2003) have treated the uniform forced convection flow in a fluid-saturated porous medium adjacent to a plane surface. The effect of viscous dissipation is included in the energy conservation equation as a quadratic term of the Darcy velocity. The effects of viscous dissipation on thermal entrance heat transfer in a parallel plate channel filled with a saturated porous medium were investigated analytically on the basis of a Darcy model by Hooman and Bandpy (2004). Nield et al. (2003) have used a modified Graetz methodology to investigate the thermal development of forced convection in parallel isothermal plates filled with a saturated porous medium. This study takes into account effects of axial conduction and viscous dissipation. The effect of viscous dissipation on the steady free convection in a square cavity filled with a porous medium has been reported numerically by Saeid and Pop (2004). His results show that the viscous dissipation effect reduces the heat transfer rate and decreases the average Nusselt number. Seddeek (2006) has reported in his study the influence of viscous dissipation and thermophoresis on Darcy-Forchheimer mixed convection in a fluid-saturated porous medium. Berletta and Magyari (2007) have given a unified analytical approach to Darcy mixed convection with viscous dissipation effects in a vertical porous channel.

Studies of forced convection heat transfer for oscillatory flow into a pipe partially filled with a porous medium are relatively scarce and often incomplete. Kim et al. (1994) have presented a study dealing with heat transfer from a pulsating flow in a channel filled with a porous medium and maintained at constant temperature. In this study, the Brinkman-Forchheimer extended Darcy model

has been used. The porosity variation and the viscous dissipation effects have been neglected. Guo et al. (1997) have investigated the pulsating flow and heat transfer in a channel partially filled with a porous medium attached to the wall pipe. In this study, axial diffusion, inertia terms, porosity variation, and viscous dissipation effects have been neglected. Dhahri et al. (2003, 2006) have investigated forced pulsating flow and heat transfer in conduits in a composite system fluid/porous medium without considering the viscous dissipation effects in the energy equation. To the best of the authors' knowledge, the viscous dissipation effects on heat transfer for oscillating flow in a composite system fluid/porous medium have not been investigated in the open literature.

The aim of this article is a numerical investigation of a forced oscillating laminar flow into a cylinder partially filled with an annular lining of porous medium. In the present work, the Brinkman-Lapwood-Forchheimer extended Darcy model with variable porosity is employed. In the energy conservation equation, the viscous dissipation term is included. The porous substrate is attached to the wall, which is heated with uniform temperature. In this study, efforts are focused on identifying the effects of emerging parameters on flow and heat transfer properties such as the Darcy number, the Womersly number, the thermal conductivity ratio, the heat capacity ratio, the porous layer thickness, and the Eckert number.

2. MATHEMATICAL FORMULATION

The analysis is carried out for an oscillating laminar, incompressible, axisymmetric, two- dimensional flow into a cylinder partially filled with an annular lining of a homogeneous and isotropic porous medium, which is attached to the wall (Fig. 1). The wall of the cylinder is heated with uniform temperature. The fluid enters the pipe at a uniform axial velocity with periodical variations according to the following relation:

$$U_i = U_{\max} \sin \omega t \qquad (1)$$

where ωt is the phase angle of the cross-sectional mean velocity, ω is the oscillatory frequency, and $U_{\max}$ is the maximum cross-sectional mean velocity.

The porous medium is saturated with a Newtonian single fluid phase and assumed to be in local thermodynamic equilibrium. The thermophysical properties of the solid matrix and of the fluid are assumed to be constant. Viscous dissipation effects are included in the energy equation.

Fluid flow and heat transfer in a composite system fluid/porous medium is described by mass conservation, momentum, and energy equations. Particular forms of transport equations in a porous medium may be derived in terms of average macroscopic variables (Whitakar, 1977; Vafai and Tien, 1981; Vafai, 2005; Dhahri et al., 2006). The differential form of these equations can be expressed as follows:

Continuity Equation:

$$\frac{\partial U}{\partial z} + \frac{1}{r}\frac{\partial (rV)}{\partial r} = 0 \qquad (2)$$

Momentum Equation:

$$\begin{aligned}
&\frac{\partial U}{\partial t} + \frac{A_o}{2}\frac{\partial}{\partial z}\left[\left(\lambda\left(\frac{1}{\varepsilon}-1\right)+1\right)UU\right] \\
&+ \frac{A_o}{2}\frac{1}{r}\frac{\partial}{\partial r}\left[\left(\lambda\left(\frac{1}{\varepsilon}-1\right)+1\right)rUV\right] \\
&= -\frac{A_o}{2}\frac{\partial P}{\partial z} + \frac{1}{\mathrm{Re}_w}\left[\frac{\partial^2 U}{\partial z^2} + \frac{1}{r}\frac{\partial}{\partial r}\left(r\frac{\partial U}{\partial r}\right)\right] \\
&- \lambda\left(\frac{\Lambda\varepsilon}{\mathrm{Da}\,\mathrm{Re}_w} + \frac{A_o}{2}\frac{F\varepsilon\Lambda^{1/2}}{\sqrt{Da}}|\mathbf{U}|\right)U
\end{aligned} \qquad (3)$$

$$\begin{aligned}
&\frac{\partial V}{\partial t} + \frac{A_o}{2}\frac{\partial}{\partial z}\left\{\left[\lambda\left(\frac{1}{\varepsilon}-1\right)+1\right]VU\right\} \\
&+ \frac{A_o}{2}\frac{1}{r}\frac{\partial}{\partial r}\left\{\left[\lambda\left(\frac{1}{\varepsilon}-1\right)+1\right]rVV\right\} \\
&= -\frac{A_o}{2}\frac{\partial P}{\partial r} + \frac{1}{\mathrm{Re}_w}\left[\frac{\partial^2 V}{\partial z^2} + \frac{1}{r}\frac{\partial}{\partial r}\left(r\frac{\partial V}{\partial r}\right)\right] \\
&- \frac{V}{\mathrm{Re}_w r^2} - \lambda\left(\frac{\varepsilon\Lambda}{\mathrm{DaRe}_w} + \frac{A_o}{2}\frac{F\varepsilon\Lambda^{1/2}}{\sqrt{Da}}|\mathbf{U}|\right)V
\end{aligned} \qquad (4)$$

Energy Equation:

$$\begin{aligned}
&\frac{\partial T}{\partial t} + \frac{A_o}{2}\frac{1}{\{\lambda[(\varepsilon-1)+(1-\varepsilon)R_c]+1\}} \\
&\times \left[\frac{\partial}{\partial z}(UT) + \frac{1}{r}\frac{\partial}{\partial r}(rTV)\right] = \frac{1}{\mathrm{Pr}\,\mathrm{Re}_w} \\
&\times \frac{1}{\{\lambda[(\varepsilon-1)+(1-\varepsilon)R_c]+1\}} \\
&\times \begin{cases} \dfrac{\partial^2}{\partial z^2}\left(\{\lambda[(\varepsilon-1)+(1-\varepsilon)R_k]+1\}T\right) \\ +\dfrac{1}{r}\dfrac{\partial}{\partial r}\left(r\{\lambda[(\varepsilon-1)+(1-\varepsilon)R_k]+1\}\dfrac{\partial T}{\partial r}\right) \end{cases} \\
&+ \mathrm{Ec}\left(\frac{\phi_1}{\mathrm{Re}_w} + \lambda\phi_2\right)
\end{aligned} \qquad (5)$$

where

$$\phi_1 = 2\left[\left(\frac{\partial V}{\partial r}\right)^2 + \left(\frac{V}{r}\right)^2 + \left(\frac{\partial U}{\partial z}\right)^2\right] + \left(\frac{\partial V}{\partial z} + \frac{\partial U}{\partial r}\right)^2$$

$$\phi_2 = \left(\frac{\varepsilon\Lambda}{\mathrm{Re}_w\mathrm{Da}} + \frac{A_o}{2}\frac{\varepsilon F\Lambda^{1/2}}{\mathrm{Da}^{1/2}}|\mathbf{U}|\right)(|\mathbf{U}|)^2$$

It is worth mentioning that the governing equations are written in a unified way for the fluid region and the porous region by introducing a binary parameter. This parameter is defined as $\lambda = 1$ in the porous region and $\lambda = 0$ in the fluid region.

The nondimensional variables and parameters are constructed on the basis of the following scales:

$$L_{\mathrm{ref}} = D, \quad \Delta T_{\mathrm{ref}} = T_w - T_i, \quad U_{\mathrm{ref}} = U_{\max},$$

$$t_{\mathrm{ref}} = \frac{1}{\omega}, \quad P_{\mathrm{ref}} = \rho U_{\max}^2$$

The dimensionless numbers and parameters arising in the equation system are the kinetic Reynolds number $\mathrm{Re}_w = \omega D^2/v$, the dimensionless oscillation amplitude $A_o = x_{\max}/D$ based on the maximum fluid displacement $x_{\max}$, the Prandtl number $\mathrm{Pr} = \mu_f C_{pf}/k_f$, the Darcy number $\mathrm{Da} = K_\infty/D^2$, the thermal conductivity ratio $R_k = k_{sd}/k_f$, the heat capacity ratio $R_c = (\rho c)_{sd}/(\rho c)_f$, the Eckert number $\mathrm{Ec} = (\mu_f U_{\max})^2/C_f\Delta T_{\mathrm{ref}}$, and the permeability ratio $\Lambda = K_\infty/K$. Here v is the kinematic viscosity, k_f is the thermal conductivity of the fluid, K is the permeability, K_∞ is the free stream permeability of the porous medium, and $x_{\max}$ is the maximum fluid displacement.

Equations (3)–(5) show that Re_w, A_o, Da, Ec, R_c, R_k, Pr, and S are similarity parameters for an incompressible oscillating flow and associated heat transfer in a pipe of circular cross section partially filled with a porous material. For the variable porosity case, the permeability of the porous medium K and the geometric function F can be represented as in Ergun (1952) and may be expressed in the following improved form (Vafai, 1984):

$$K = \frac{\varepsilon^3 d_p^2}{150(1-\varepsilon)^2}, \quad F = \frac{1.75}{\sqrt{150\varepsilon^3}} \qquad (6)$$

where d_p is the particle diameter and ε denotes the medium porosity. According to an experimental observation given by Robee et al. (1958) and Benenati and Brosilow (1996), the porosity in a randomly packed bed is dependent on the distance from the wall. A common practice is to consider an exponential decaying function

to approximate the spatial porosity variation. In this study, the porosity distribution throughout the porous medium can be represented by the following equation (Dhahri al., 2006):

$$\varepsilon = \varepsilon_\infty \left[1 + a_1 e^{-0.5 a_2 \left(1 - \frac{r - r_1}{R - r_1} \right)} \right] \qquad (7)$$

where ε_∞ is the porosity far from the wall, while a_1 and a_2 are empirical constants. Variable ε_∞ was chosen to be 0.37, whereas the chosen values of a_1 and a_2 are, respectively, $a_1 = 1.7$ and $a_2 = 6$. These values lead to a good approximation with the available experimental data (Amiri and Vafai, 1994).

2.1 Boundary Conditions

Initially, the fluid is at rest and the nondimensional temperature is equal to 0. The associated boundary conditions are formulated as follows:

At the Cylinder Inlet ($z = 0$ for $0 \prec r \prec 0.5$:

$$U = \sin(\omega\tau), \quad V = 0, \quad \text{and} \quad T = 0 \quad \text{if} \quad \omega\tau \leq 180°$$

$$\frac{\partial U}{\partial z} = 0, \quad \frac{\partial V}{\partial z} = 0, \quad \text{and} \quad \frac{\partial T}{\partial z} = 0 \quad \text{if} \quad \omega\tau \geq 180°$$

At the Cylinder Outlet ($z = L$ for $0 \prec r \prec 0.5$:

$$U = \sin(\omega\tau), \quad V = 0, \quad \text{and} \quad T = 0 \quad \text{if} \quad \omega\tau \geq 180°$$

$$\frac{\partial U}{\partial z} = 0, \quad \frac{\partial V}{\partial z} = 0, \quad \text{and} \quad \frac{\partial T}{\partial z} = 0 \quad \text{if} \quad \omega\tau \leq 180°$$

At the Cylinder Wall ($r = 0.5$):

$$U = V = 0 \quad \text{and} \quad T = 1$$

Owing to the Symmetry Requirement at the Cylinder Centerline ($r = 0$):

$$\frac{\partial U}{\partial r} = V = \frac{\partial T}{\partial r} = 0$$

3. NUMERICAL PROCEDURE

In this study, we have used a two-dimensional laminar version of the control volume–based finite element method described by Baliga and Patankar (1980, 1983) and Dhahri et al. (2003, 2006). The Tri-Diagonal-Matrix Algorithm (TDMA) solver solves discretized and linearized equations system using the SIMPLER algorithm.

Accuracy tests were performed using different sets of grids in the $z - r$ directions: (111×31), (151×51), and (181×71) for different local variables (U, V, T, and P). The results obtained using a finer grid of (181×71) do not reveal discernible changes in the predicted heat transfer and flow field. Furthermore, there is a difference around 2% between the results obtained using this finer grid and those obtained using (151×51). Thus a (151×51) mesh size was used in this computation. In the present computation, typically 5–10 iterations were required for these local variables to achieve convergence. Furthermore, the time resolution was such that one oscillation period was divided by 3600 time steps during a cycle. The grid was selected as a trade-off between numerical accuracy, stability, and computational time. The convergence criterion adopted is that the relative variation of velocity and temperature fields between two successive iterations is smaller than 10^{-4}. For the present problem, satisfactory results are obtained where the initial velocities are arbitrarily chosen to be zero everywhere. In this case, the steady periodic state is reached after only a few cycles.

4. RESULTS AND DISCUSSION

To validate the established numerical procedure, the proposed numerical methodology was extensively tested with results for three different situations: (1) for a laminar forced convection in a heated pipe subjected to reciprocating flow (Zhao and Cheng, 1995) (Fig. 2), (2) for the case of pulsating flow in a channel without a porous medium (Cho and Hyun, 1990) (Fig. 3), and (3) for the case of nonpulsating flow in a channel partially filled with a porous medium (Poulikakos and Kazmierczak, 1987; Guo et al., 1997) (Fig. 4).

For case 1, there were typical variations of axial velocity and fluid temperature near the entrance of the pipe ($z = 6.2$) for $A_o = 15$ and $Re_w = 64$ at different radial positions during one cycle ($0° \leq \omega t \leq 360°$) (Fig. 2). As displayed in Fig. 2, the present numerical results are in fair agreement with the published ones. In case 2, the radial variation of the axial velocity at different axial positions is presented. As depicted in Fig. 3, the agreement between the predicted and published results is very satisfactory. In case 3, the nonpulsating flow corresponds to the case where the thickness of the porous medium near the wall is equal to 20% of the pipe radius ($S = 0.2$) and the pressure drop ($B = -\partial P / \partial z$) = 0.32. Figure 4 shows the axial velocity profile for different Darcy numbers. It can be seen that fluid flow is strongly subordinate
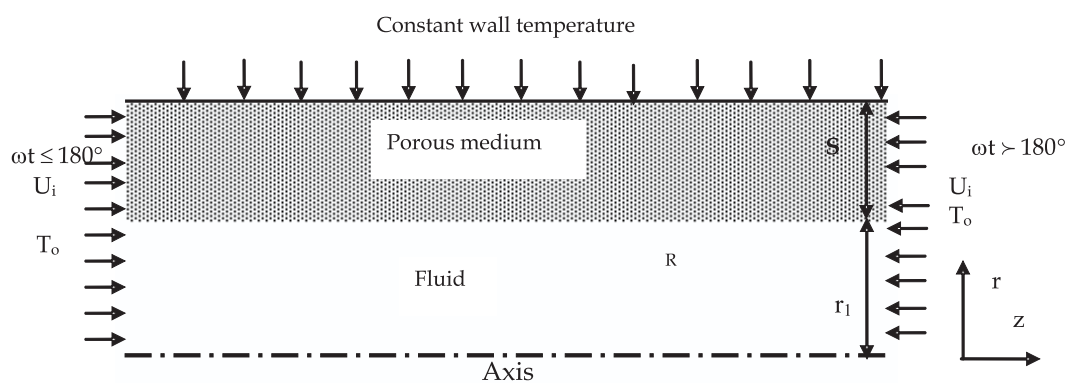
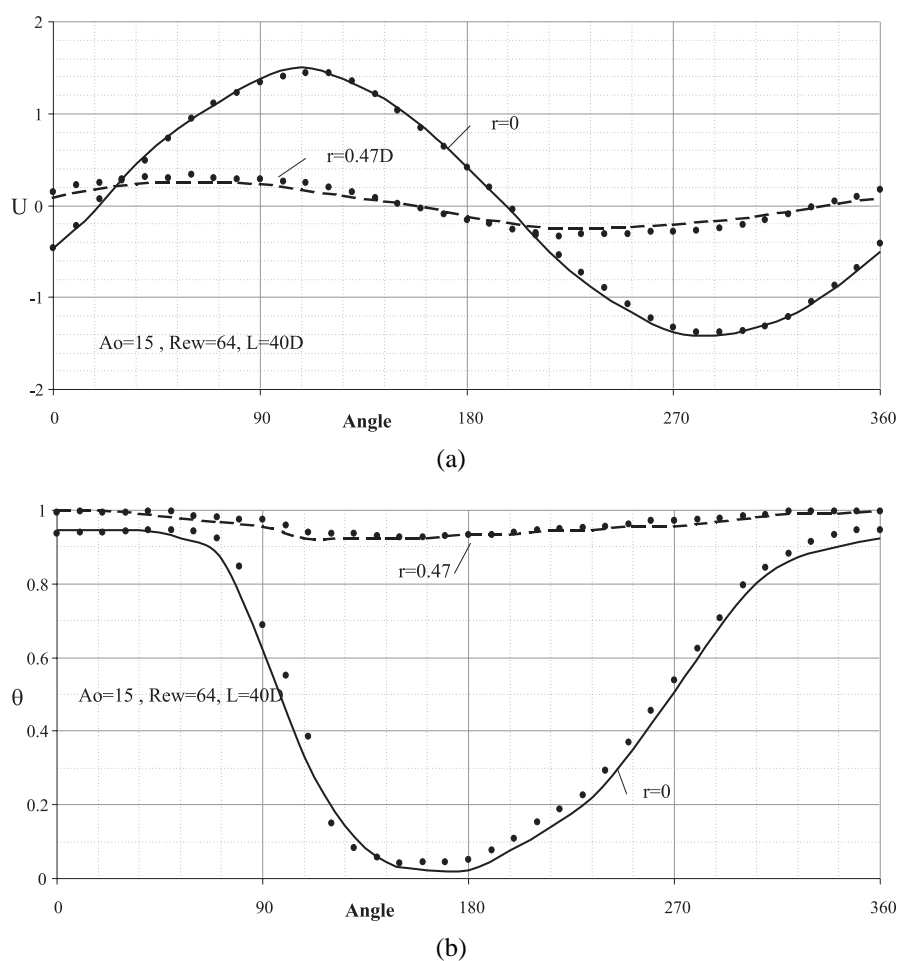**FIG. 1:** Schematic of a finite length pipe of a circular cross section partially filled with a porous medium.

FIG. 2: Instantaneous velocity profiles, U, for $M = 5$ and $A = 0.344$. Solid line shows the present calculations at $\omega t = 310°$. Measurements of Chao et al. (1990): (diamonds, $z = 0.005$; triangles, $z = 0.0432$; circles, $z = 0.263$).
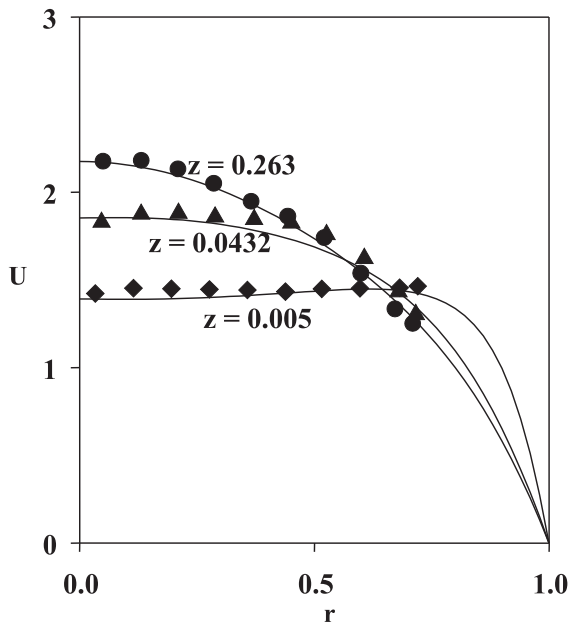
FIG. 3: Comparison of the steady nonpulsating velocity profile in the fully developed region. $S = 0.2$, $B = 0.32$ [solid line, numerical; circles, analysis obtained by Poulikakos et al. (1987) and Guo et al. (1997)].
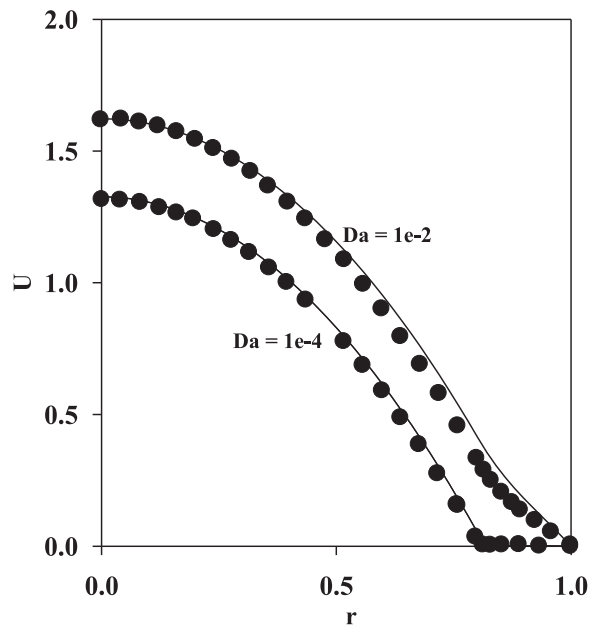
FIG. 4: Temporal variations in **(a)** velocity and **(b)** temperature at $z = 6.2$ and at different radial positions for $A_o = 15$ and $\text{Re}_w = 64$ [solid line, numerical; dashed line, Zhao et al. (1995)].

on Darcy number. Furthermore, our numerical results are in satisfactory agreement with those provided in the literature.

In all computations performed here, the dimensionless oscillation amplitude, the Prandtl number, and the cylinder length were chosen to be $A_o = 2.5$, $\text{Pr} = 7$, and $L = 40D$, respectively. Several sample computations established that a pipe length equal to 40 times its diameter ($L = 40D$) is compatible with the existing boundary conditions.

5. DYNAMIC FIELD

To understand the development of the flow in a pipe, the axial velocity profiles in the fully developed region are shown in Fig. 5(a). As expected, the presence of the inertia term and viscous forces generated by the solid matrix affected significantly the axial velocity. Therefore the flow is accelerated in the central zone, where a local maximum can occur depending on the porous layer thickness S, and decelerated near the interface fluid–porous medium. In the porous layer, according to the porosity variation, the axial velocity reaches a second local maximum with the velocity overshoot near the wall. Another point derived from this figure that the axial velocity in the porous layer is very small compared with the same in the fluid layer. Owing to the high resistance of the porous layer, fluid is squeezed out from the porous medium to the fluid layer. Therefore the fluid coming from the porous layer pushes the peak of velocity toward the inlet. It is interesting to note from this figure that the thickness of the dynamic boundary layer formed near the wall is significantly affected by the porous layer thickness. Furthermore, there is an optimal value of S depending on the Darcy number for which the flow rate in the fluid and porous regions is maximum. The effect of Darcy number on the axial velocity profile is depicted in Figs. 5(a) and 5(b). For small Darcy number, the porous layer is considered less permeable, and consequently, convective activities are suppressed in the porous layer.

A physical quantity of great interest in engineering applications is the skin friction coefficient based on the flow data. The skin friction can be written as follows:

$$C_f = \frac{\mu \left(\frac{\partial U}{\partial r} \right)_{r=0.5}}{\rho U_{\max}^2}$$

Figure 6(a) illustrates the temporal variation of skin friction for different values of the porous layer thickness S. It can be seen that the friction losses are affected significantly by the porous layer thickness. Higher friction
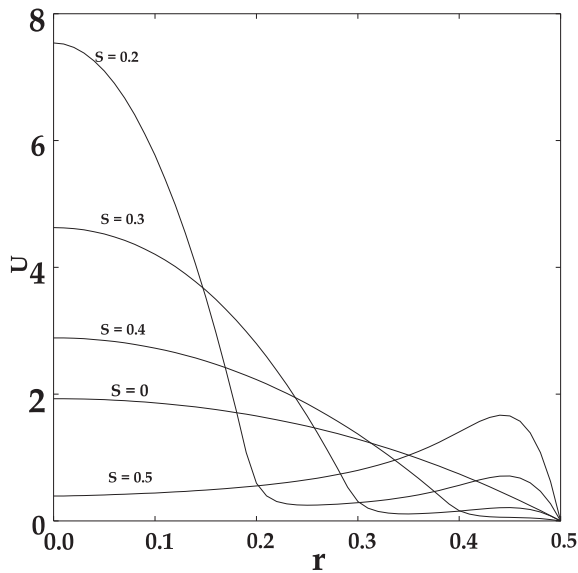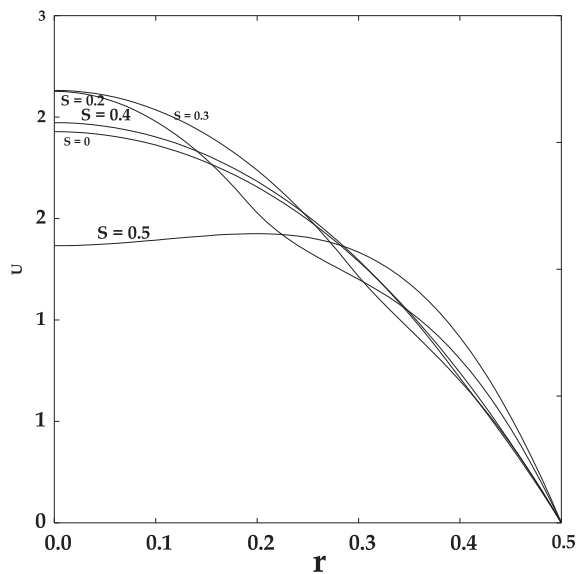
FIG. 5: Effect of S on the velocity profiles $U(r)$ for different Darcy numbers for $\alpha = 5$ at $\omega t = 90°$: **(a)** Da $= 10^{-4}$; **(b)** Da $= 1$.
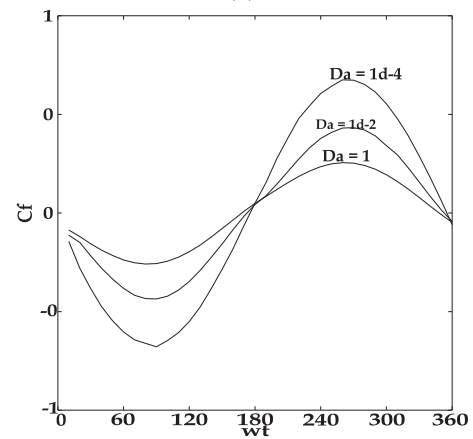
losses are found for $S = 0.5$. In addition, there is an optimum value of S ($S = 0.4$) for which the friction losses are lower. It is interesting to note that C_f is found to increase with the Womersly number α [Fig. 6(b)]. This is can be explained by the fact that C_f is affected by convection. It is worth mentioning that using a porous
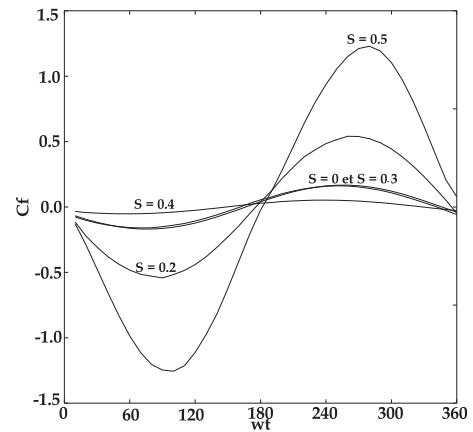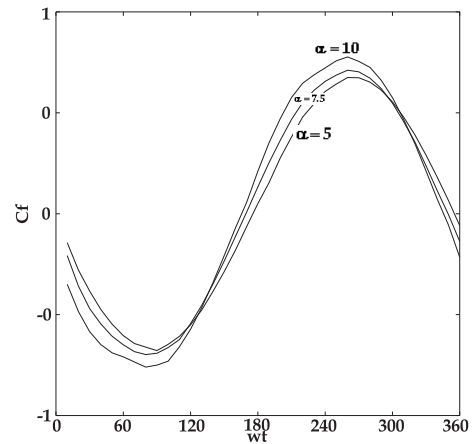
FIG. 6: Temporal variation of the friction losses **(a)** for different values of S (Da $= 10^{-4}$ and $\alpha = 5$), **(b)** for different values of α ($S = 0.2$ and Da $= 10^{-4}$, and **(c)** for different values of Da ($S = 0.2$ and $\alpha = 5$).

medium with high Darcy number reduces friction losses [Fig. 6(c)]. As a result, to reduce the friction losses, there is a need to use a porous medium with high Darcy number, or a partial filling is sufficient with a lower Darcy number to reduce the friction losses.

As far as the pressure drop is concerned, the temporal variations of the pressure drop ΔP are plotted in Fig. 7. It can be concluded from Fig. 7(a) that the partial filling reduces the pressure drop. The existence of an optimal value of S around 0.4 for which the pressure drop is lower confirms this behavior. It can be seen from Fig. 7(b) that the profiles of the pressure drop decrease with the increase of α. Two main reasons may be attributed to the decrease of this pressure drop. First, the radial velocity gradients adjacent to the pipe wall become steeper; consequently, the friction force decreases with the increase of α. Second, the inertia term decreases with α. Figure 7(c) demonstrates that the amplitude of ΔP becomes smaller when the Darcy number increases. This implies that the resistance to the porous matrix generated by viscous forces to the flow becomes large as Da decreases. It is interesting to note that the use of material with high permeability can reduce significantly the pressure drop.

For fixed values of Da and α, ΔP and U are nearly in phase, but they are in opposite phase with C_f (Fig. 8). Another point depicted from this figure is that high pressure corresponds to high flow velocity, which shows that the phase difference between the velocity and pressure drop is very small. An increase of Darcy number at a fixed value of α affected considerably the magnitude of ΔP, U, and C_f and the difference phases. The same phenomena have been found for a fixed value of Da and an increasing α. It is worth mentioning from this figure that high pressure corresponds to high flow velocity, which shows that the phase difference between velocity and pressure drop is very quite small.

6. THERMAL FIELD

Thermal field behavior has been compared with that obtained by neglecting the viscous dissipation effects. It can be concluded that the viscous dissipation causes an increase of the temperature [Fig. 9(a)]. From a practical point of view, the heat generation caused by viscous dissipation plays a role in the development of the temperature field in the porous pipe when the value of the permeability takes a considerably small value. Moreover, viscous dissipation affects the nature of the developing temperature profiles. Near the inlet ($z = 0.266$), the fluid heats up rapidly for large values of Ec. In addition, the fluid tem-
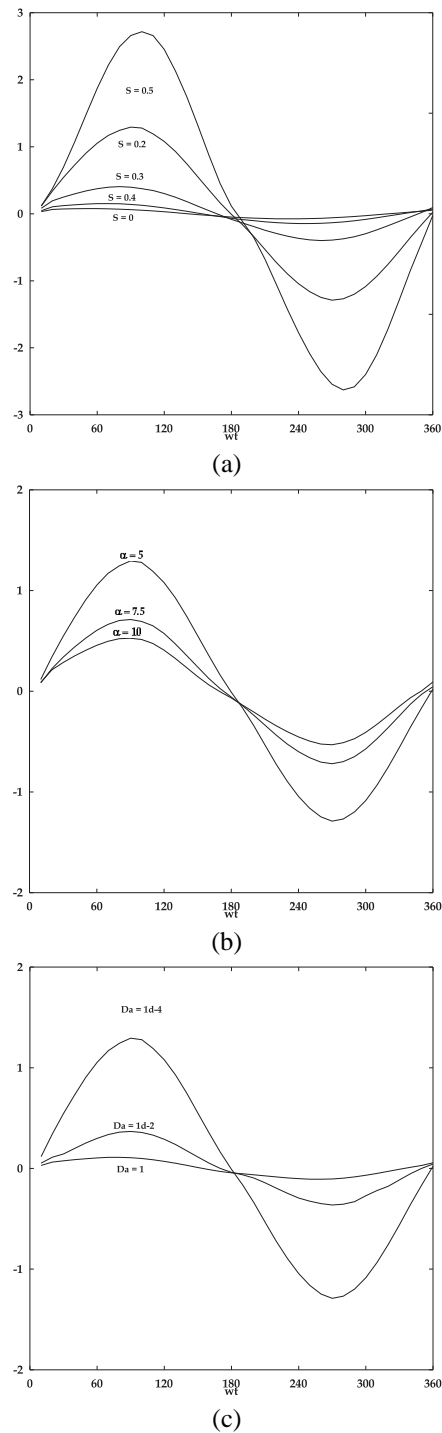

FIG. 7: Temporal variation of the pressure drop (a) for different values of S (Da $= 10^{-4}$ and $\alpha = 5$), (b) for different values of α ($S = 0.2$ and Da $= 10^{-4}$), and (c) for different values of Da ($S = 0.2$ and $\alpha = 5$).
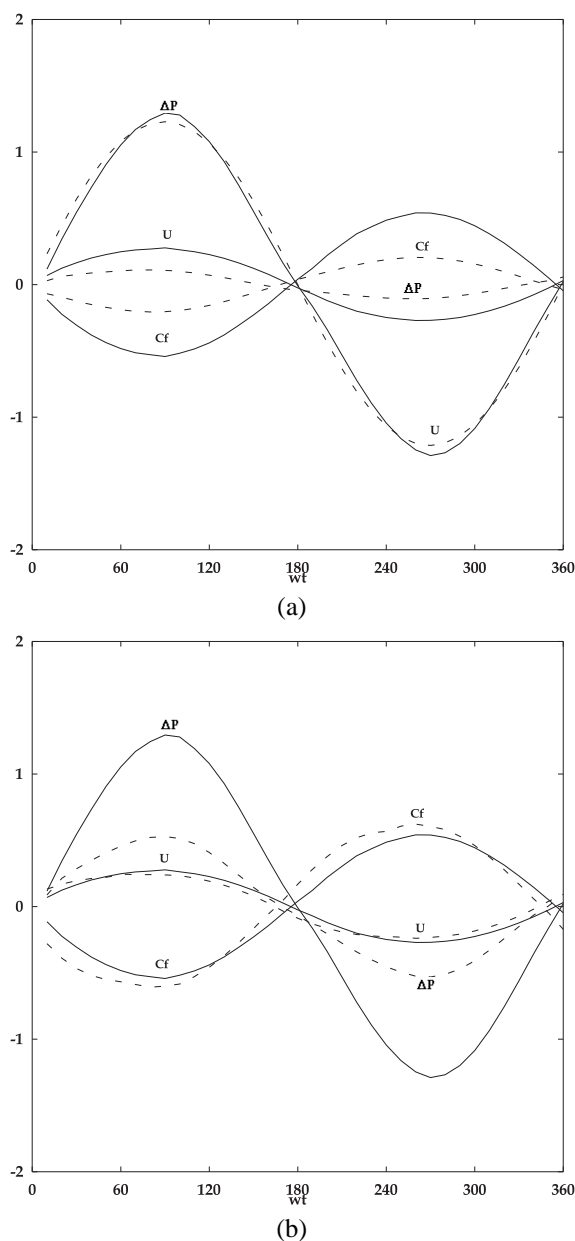
(a)

(b)

FIG. 8: Temporal variations of the axial velocity, pressure drop, and friction losses in the fully developed region for different Darcy numbers **(a)** $\alpha = 5$ (Da = 10^{-4} and Da = 1) and **(b)** Da = 10^{-4} ($\alpha = 5$ and $\alpha = 10$).

(a)

(b)

(c)

FIG. 9: Instantaneous radial variations of the fluid temperature at different axial locations at $\omega t = 60°$ **(a)** for different values of Ec, $S = 0.2$, Da = 10^{-4}, $\alpha = 5$, $R_k = 5$, and $R_c = 5$ ($z = 0.266$ and $z = 39.73$) and **(b** and **c)** for different values of S ($z = 0.266$ and $z = 39.73$, respectively), Da = 10^{-4}, $\alpha = 5$, Ec = 0.1, $R_k = 5$, and $R_c = 5$.

perature reaches a local maximum value near the interface of the fluid-porous layer. This local maximum is significantly affected by the Eckert number Ec. Near the outlet ($z = 39.73$), the fluid temperature increases in the central
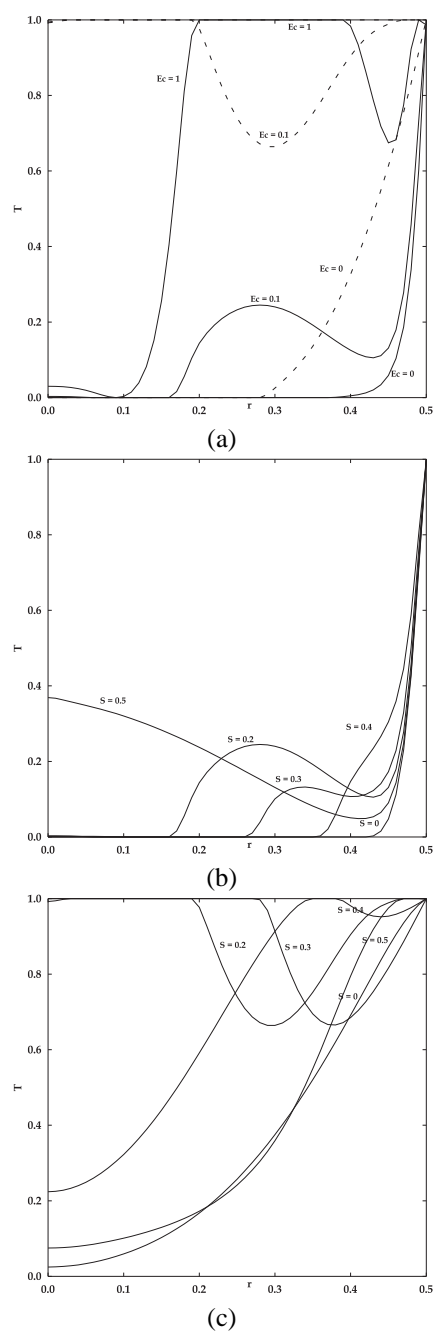
zone. For Ec = 0.1, the fluid temperature reaches a local minimum in the central zone. For large values of Ec, the fluid temperature and the imposed wall temperature are equal.

Near the inlet ($z = 0.266$), the temperature increases in the porous region to reach a maximum value near the fluid–porous layer interface. This is due to the porosity variation effect [Fig. 9(b)]. Near the wall, the temperature increases to reach the prescribed wall temperature. This local maximum value is affected by the porous layer thickness. Near the outlet ($z = 39.73$), we observe the inverse phenomenon [Fig. 9(c)].

Processing the numerical results of the thermal field, the heat transfer properties are now examined. One physical quantity of interest is the local Nusselt number, defined as

$$\text{Nu}\,(z,t) = \frac{h_{sf}D}{k_{\text{eff}}} = -\left(\frac{\partial T}{\partial r}\right)_{r=0.5}$$

Near the inlet ($z = 0.266$), the time evolution of $\text{Nu}(z,t)$ reaches optimums values that are strongly subordinate on S. As time increases, the local Nusselt number deceases to reach a zero value for a phase angle depending on the porous layer thickness. Near the outlet ($z = 39.73$), $\text{Nu}(z,t)$ decreases to reach the zero value for a phase angle depending on the porous layer thickness S for ($\omega t \prec 180°$). For ($\omega t \succ 180°$), the time evolution of $\text{Nu}(z,t)$ reaches extreme values depending on the porous layer thickness. Near both extremities ($z = 0.266$ and $z = 39.73$), the partial filling reduces the local Nusselt number (Fig. 10). It can be seen from this figure that using a pipe without a porous medium or completely filled with a porous medium enhances the heat transfer rate. The nonlinearity trends observed in the local Nusselt number profiles for different values of S are due to the viscous dissipation effects. Moreover, $\text{Nu}\,(z,t)$ increases with an increase of α. This happens due to the fact that high α leads to high inertia forces and thus faster movement, which enhances the local heat generation [Fig. 11(a)].

We now move to examine the effect of viscous dissipation. It is clear from Fig. 11(b) that an increase of the Eckert number reduces the local Nusselt number level. The profiles of $\text{Nu}(z,t)$ for lower Ec are in opposite phase with that for high Ec. It is apparent from Fig. 11(c) that a decreasing of the Darcy number introduces nonlinearity into the local Nusselt number profiles at the two extremities. In general, the overall heat transfer rate is enhanced with an increase of R_k due to large temperature gradients affected near the wall [Fig. 11(d)]. It can be observed here that with viscous dissipation effects, there is an op-
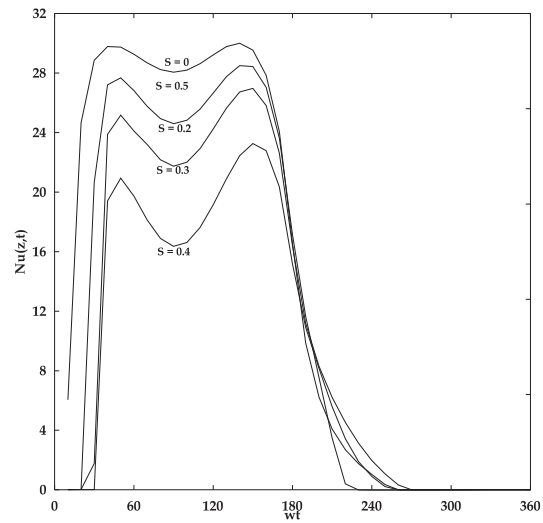
(a)
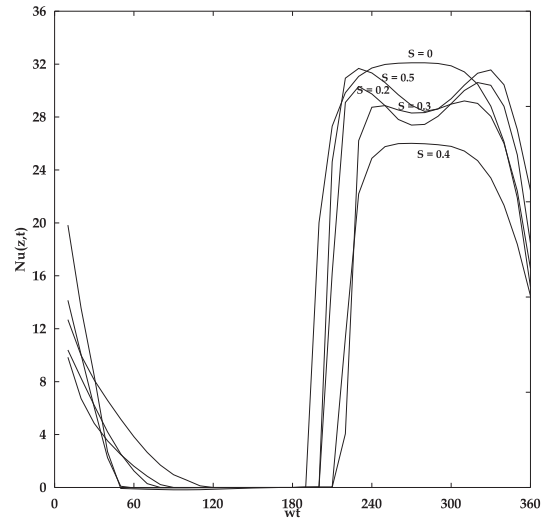
(b)

FIG. 10: Temporal variation of the local Nusselt number $\text{Nu}(z,t)$ as a function of S at different axial locations for Da = 10^{-4}, α = 5, $R_k = 5$, $R_c = 5$, and Ec = 0.1: **(a)** $z = 0.266$ and **(b)** $z = 39.73$.

timal value of R_k for which the $\text{Nu}(z,t)$ is maximal in both extremities. At the two extremities, the $\text{Nu}(z,t)$ decreases with R_c [Fig. 11(e)]. In this case, using a material with high capacity reduces the heat transfer rate. This is can be explained by the fact that the solid will absorb the heat transferred by the fluid. Furthermore, near the inlet ($z = 0.266$), for R_c around 20, the local Nusselt number is equal to zero. This trend can be explained by the fact
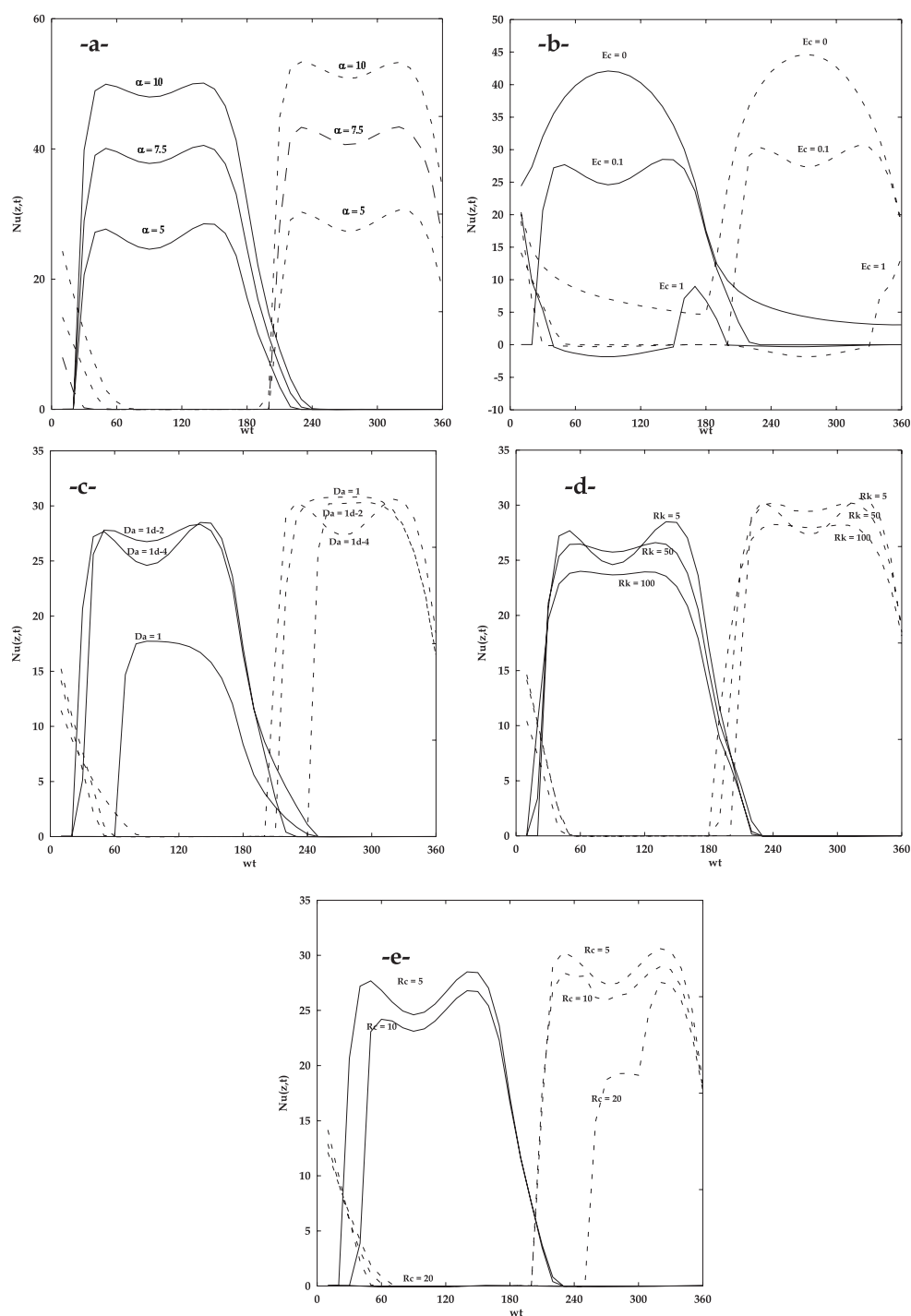
FIG. 11: Temporal variation of the local Nusselt number $\mathrm{Nu}(z,t)$ for $S = 0.2$ ($z = 0.266$ and $z = 39.73$) for **(a)** for different values of α ($\mathrm{Da} = 10^{-4}$, $\mathrm{Ec} = 0.1$, $R_k = 5$, and $R_c = 5$), **(b)** for different values of Ec ($\mathrm{Da} = 10^{-4}$, $\alpha = 5$, $R_k = 5$, and $R_c = 5$), **(c)** for different values of Da ($\alpha = 5$, $\mathrm{Ec} = 0.1$, $R_k = 5$, and $R_c = 5$), **(d)** for different values of R_k ($\mathrm{Da} = 10^{-4}$, $\mathrm{Ec} = 0.1$, $\alpha = 5$, and $R_c = 5$), and **(e)** for different values of R_c ($\mathrm{Da} = 10^{-4}$, $\mathrm{Ec} = 0.1$, $R_k = 5$, and $\alpha = 5$).

FIG. 12: The averaged local Nusselt number $\overline{Nu}$ versus S **(a)** for different values of α (Da $= 10^{-4}$, Ec $= 0.1$, $R_k = 5$, and $R_c = 5$, **(b)** for different values of Ec (Da $= 10^{-4}$, $\alpha = 5$, $R_k = 5$, and $R_c = 5$, **(c)** for different values of Da ($\alpha = 5$, Ec $= 0.1$, $R_k = 5$, and $R_c = 5$, **(d)** for different values of R_k (Da $= 10^{-4}$, Ec $= 0.1$, $\alpha = 5$, and $R_c = 5$), and **(e)** for different values of R_c (Da $= 10^{-4}$, Ec $= 0.1$, $R_k = 5$, and $\alpha = 5$).
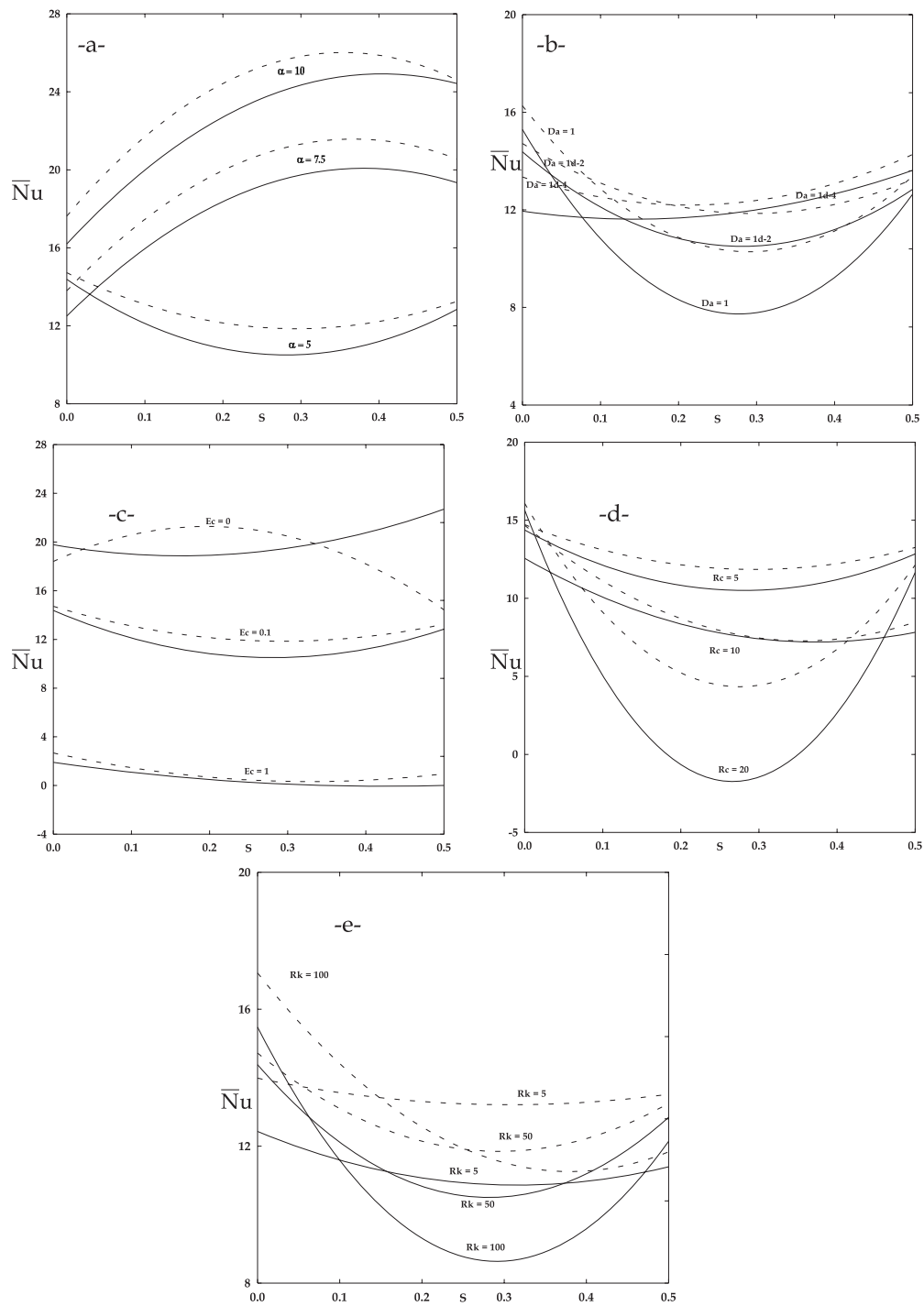
that the wall temperature is equal to the fluid temperature near the wall.

The variations of the time-averaged local Nusselt number $\overline{\mathrm{Nu}} = fr \int_0^{1/fr} \mathrm{Nu}(z, t) dt$ versus the porous layer thickness, where fr represents the oscillation frequency, are illustrated in Fig. 12. It is interesting to note that the variations of $\overline{\mathrm{Nu}}$ versus S for α, Ec, Da, R_c, and R_k are polynomial. It can be seen from this figure the existence of an optimal value of S depending on these several emerging parameters (α, Ec, Da, R_c, and R_k) for which the $\overline{\mathrm{Nu}}$ near both extremities has an extreme value.

7. CONCLUSION

Numerical simulation is performed here to investigate the effects of viscous dissipation on heat transfer for oscillating flow in a composite system fluid/porous medium. The velocity, the friction losses, the pressure drop, the temperature, the local Nusselt number, and the time-averaged local Nusselt number are presented and discussed.

The specific conclusions derived from this study can be listed briefly as follows:

1. The axial velocity reaches a maximum value at the pipe centerline for an optimal value of S depending on the Darcy number.

2. Phase angle differences between the magnitudes of ΔP, U, and C_f are affected by Da or α.

3. Partial filling reduces friction losses and pressure drop for oscillating flow in a composite system fluid/porous medium.

4. The fluid temperature heats up rapidly due to viscous dissipation effects. These effects change the nature of the temperature profiles.

5. An increasing of Ec reduces the local Nusselt number.

6. There is a critical value of S depending on R_k or R_c for which the local Nusselt number is minimal.

7. There is a critical value of S depending of the emerging parameters α, Ec, Da, R_c, and R_k for which the time-averaged local Nusselt number reaches an extreme value.

REFERENCES

Amiri, A. and Vafai, K., Analysis of dissipation effects and non-thermal equilibrium, non-Darcian, variable porosity incompressible flow through porous media, *Int. J. Heat Mass Transfer,* vol. **37**, pp. 939–954, 1994.

Baliga, B. R. and Patankar, S. V., A new finite-element formulation for convection-diffusion problems, *Numer. Heat Transfer,* vol. **3**, pp. 393–409, 1980.

Baliga, B. R. and Patankar, S. V., A control-volume finite element method for two-dimensional fluid flow and heat transfer, *Numer. Heat Transfer,* vol. **6**, pp. 245–261, 1983.

Barletta, A. and Magyari, E., Forced convection with viscous dissipation in the thermal entrance region of a circular duct with prescribed wall heat flux, *Int. J. Heat Mass Transfer,* vol. **50**, pp. 26–35, 2007.

Benenati, R. F. and Brosilow, C. B., Void fraction distribution in beds spheres, *AIChE J.*, vol. **4**, pp. 450–464, 1996.

Cha, J. S., Ghiaasiaan, S. M., and Kirkconnell, C. S., Oscillatory flow in microporous media applied in pulse-tube and Stirling-cycle cryocooler regenerators, *Exp. Thermal Fluid Sci.,* vol. **32**, pp. 1264–1278, 2008.

Chikh, S., Boumedien, A., Bouhadef, K., and Lauriat, G., Analytical solution of non-Darcian forced convection in an annular partially filled with a porous medium, *Int. J. Heat Mass Transfer*, vol. **38**, pp. 1543–1551, 1995a.

Chikh, S., Boumedien, A., Bouhadef, K., and Lauriat, G., Non-Darcian forced convection in an annular duct partially filled with a porous medium, *Numer. Heat Transfer A*, vol. **38**, pp. 707–722, 1995b.

Cho, H. W. and Hyun, J. M., Numerical solutions of pulsating flow and heat transfer characteristics in a pipe, *Int. J. Heat Fluid Flow*, vol. **11**, pp. 321–330, 1990.

Costa, V. A. F., Oliveira, M. S. A., and Sousa, A. C. M., Numerical simulation of non-Darcian flows through spaces partially filled with a porous medium, *Comput. Struct.*, vol. **82**, pp. 1535–1541, 2004.

Deng, C. and Martinez, D. M., Viscous flow in a channel partially filled with a porous medium and with wall suction, *Chem. Eng. Sci.*, vol. **60**, pp. 329–336, 2005.

Dhahri, H., Boughamoura, A., and Ben Nasrallah, S., Forced heat transfer for pulsating flow in composite system porous/fluid system, *Int. J. Heat Technol.*, vol. **21**, pp. 193–202, 2003.

Dhahri, H., Boughamoura, A., and Ben Nasrallah, S., Forced pulsating flow and heat transfer in a tube partially filled with porous medium, *J. Porous Media*, vol. **9**, pp. 1–14, 2006.

El-Amin, M. F., Combined effect of viscous dissipation and Joule heating on MHD forced convection over a non-isothermal horizontal cylinder embedded in a fluid saturated porous medium, *J. Magnetism Magnetic Mater.,* vol. **263**, pp. 337–343, 2003.

Ergun, S., Fluid flow through packed columns, *Chem. Eng. Proc.*, vol. **48**, pp. 89–92, 1952.

Fang, T., Heat transfer of oscillating and steady flows in a channel filled with porous medium, *Int. Commun. Heat Transfer,* vol. **31**, pp. 63–72, 2004.

Fu, H. L., Leong, K. C., Huang, X. Y., and Liu, C. Y., An experimental study of heat transfer of a porous channel subjected to oscillatory flow, *Trans. ASME*, vol. **123**, pp. 162–170, 2001.

Guo, Z., Kim, S., and Sung, H. J., Pulsating flow and heat transfer in a pipe partially filled with porous medium, *Int. J. Heat Mass Transfer,* vol. **40**, pp. 4209–4218, 1997.

Hooman, K. and Bandpy, M. G., Effects of viscous dissipation on forced convection in a porous saturated duct with uniform wall temperature, *Heat Transfer Res.*, vol. **35**, pp. 132–142, 2004.

Huang, P. C. and Vafai, K., Analysis of forced convection enhancement in a channel using porous block, *J. Therm. Heat Transfer,* vol. **8**, pp. 563–573, 1994.

Ingham, D. B. and Pop, I., *Transport Phenomena in Porous Media*, vol. **2**, Pergamon, Oxford, 2002.

Ingham, D. B., Pop, I., and Cheng, P., Combined free and forced convection in a porous medium between two vertical walls with viscous dissipation, *Transp. Porous Media,* vol. **5**, pp. 381–398, 1990.

Jankowski, T. A. and Majdalani, J., Laminar flow in a porous channel with large wall section and weakly oscillatory pressure, *Phys. Fluids*, vol. **14**, pp. 1101–1110, 2003.

Jen, T. C. and Yan, T. Z., Developing fluid flow and heat transfer in a channel partially filled with porous medium, *Int. J. Heat Mass Transfer,* vol. **48**, pp. 3395–4009, 2005.

Khodadadi, J. M., Oscillatory fluid flow through a porous medium channel bounded by two impermeable parallel plates, *J. Fluid Eng.,* vol. **113**, pp. 509–511, 1991.

Kim, S. Y., Kang, B. H., and Hyun, J. M., Heat transfer from pulsating flow in a channel filled with porous medium, *Int. J. Heat Mass Transfer,* vol. **37**, pp. 2025–2033, 1994.

Leong, K. C. and Jin, L. W., An experimental study of heat transfer in oscillating flow through a channel filled with an aluminium foam, *Int. J. Heat Mass Transfer,* vol. **48**, pp. 243–253, 2005.

Leong, K. C. and Jin, L. W., Characteristics of oscillating flow through a channel filled with open-cell metal foam, *Int. J. Heat Fluid Flow,* vol. **27**, pp. 144–153, 2006.

Magyari, E., Pop, I., and Keller, B., Effect of viscous dissipation effect on the Darcy forced convection flow past a plane surface, *J. Porous Media*, vol. **6**, pp. 29–40, 2003.

Mohamad, A. A., Heat transfer enhancement in heat exchangers fitted with porous media. Part I: Constant wall temperature, *Int. J. Thermal Sci.*, vol. **42**, pp. 387–395, 2003.

Nield, D. A. and Bejan, A., *Convection in Porous Media*, 2nd ed., Springer, New York, 1999.

Nield, D. A., Kuznetsov, A., and Ming, X., Thermally developing forced convection in a porous medium: Parallel plate-channel with walls at uniform temperature, with axial conduction and viscous dissipation effects, *Int. J. Heat Mass Transfer,* vol. **46**, pp. 643–651, 2003.

Pop, I. and Ingham, D. B., *Convective Heat Transfer: Mathematical and Computational Modelling of Viscous Fluids and Porous Media*, Pergamon, Oxford, 2001.

Poulikakos, D. and Kazmierczak, M., Forced convection in a duct partially filled with a porous material, *ASME J. Heat Transfer*, vol. **109**, pp. 653–664, 1987.

Renato, A. S. and Marcelo, J. L. S., Turbulent flow in a channel occupied by a porous layer considering the stress jump at the interface, *Int. J. Heat Mass Transfer,* vol. **46**, pp. 5113–5121, 2003.

Robee, L. H. S., Braid, R. M., and Tienny, J. W., Radial porosity variation in packed beds, *AIChE J.,* vol. **8**, pp. 359–361, 1958.

Saeid, N. H. and Pop, I., Viscous dissipation effects on free convection in a porous cavity, *Int. Commun. Heat Mass Transfer,* vol. **31**, pp. 723–732, 2004.

Seddeek, M. A., Influence of viscous dissipation and thermophoresis on Darcy-Forchheimer mixed convection in a fluid saturated porous media, *J. Colloid Interface Sci.*, vol. **293**, pp. 137–142, 2006.

Sozen, M. and Vafai, K., Analysis of oscillating compressible flow through a packed bed, *Int. J. Heat Fluid Flow,* vol. **12**, pp. 130–136, 1991.

Vafai, K., Convective flow and heat transfer in variable-porosity media, *J. Fluid Mech.,* vol. **147**, pp. 233–259, 1984.

Vafai, K., *Handbook of Porous Media*, Marcel Dekker, New York, 2000.

Vafai, K., *Handbook of Porous Media*, 2nd ed., Taylor & Francis, New York, 2005.

Vafai, K. and Tien, C. L., Boundary and inertia effects on flow and heat transfer on porous media, *Int. J. Heat Mass Transfer,* vol. **24**, pp. 195–203, 1981.

Velarde, J. R. H., Zenit, R., and Mena, B., Measurement of the temperature rise in non-Newtonian oscillatory pipe flows, *J. Non-Newtonian Fluid Mech.*, vol. **109**, pp. 157–176, 2003.

Whitaker, S., Simultaneous heat, mass, and momentum transfer in porous media: A theory of drying, *Adv. Heat Transfer,* vol. **108**, pp. 119–203, 1977.

Yee, S. S. and Kamiuto, K., Effect of viscous dissipation on forced-convection heat transfer in cylindrical packed-beds, *Int. J. Heat Mass Transfer*, vol. **45**, pp. 461–464, 2002.

Zhang, B. and Zhao, Y., A numerical method for simulation of forced convection in a composite porous/fluid region, *Int. J. Heat Fluid Flow*, vol. **21**, pp. 432–441, 2000.

Zhao, T. S. and Cheng, P., A numerical solution of laminar forced convection in a heated pipe subjected to a reciprocating flow, *Int. J. Heat Mass Transfer*, vol. **38**, pp. 3011–3022, 1995.